2016

Novel cooling strategies for improved protection of gas turbine blades

Wenwu Zhou
Iowa State University

Novel cooling strategies for improved protection of gas turbine blades

by

Wenwu Zhou

A dissertation submitted to the graduate faculty

in partial fulfillment of the requirements for the degree of

DOCTOR OF PHILOSOPHY

Major: Aerospace Engineering

Program of Study Committee:
Hui Hu, Major Professor
Alric P. Rothmayer
Anupam Sharma
Xinwei Wang
Xiaoli Tan

Iowa State University

Ames, Iowa

2016

TABLE OF CONTENTS

Page

NOMENCLATURE

C_p	=	Pressure coefficient, $(p-p_\infty)\Big/\frac{1}{2}\rho U_\infty^2$
D	=	Diameter of hole / dimple
D_h	=	Hydraulic diameter of test section
D_s	=	Concentration diffusion coefficient of species
DR	=	Density ratio of the coolant and mainstream, ρ_c/ρ_∞
h	=	Depth of dimple
H	=	Height of test section
I	=	Momentum flux ratio of the coolant and mainstream flow, $\rho_c V_c^2 \big/ \rho_\infty V_\infty^2$
Le	=	Lewis number, α/D_s
M	=	Mass flux ratio of the coolant and mainstream flow, $\rho_c V_c/\rho_\infty V_\infty$
Ma	=	Mach number
q''	=	Heat flux
Re	=	Reynolds number of incoming flow, $\rho U_\infty D_h/\mu$
T_{aw}	=	Adiabatic wall temperature at the wall
T_c	=	Temperature of the coolant
T_∞	=	Temperature of the main stream flow
U_∞	=	Incoming free stream velocity
W	=	Width of channel
α	=	Thermal diffusion coefficient
η_{aw}	=	Adiabatic film cooling effectiveness at the wall

Δq_r = Net heat flux reduction

ϕ = Overall cooling effectiveness

$\left(C_{o_2}\right)_{main}$ = Oxygen concentration of mainstream

$\left(C_{o_2}\right)_{mix}$ = Oxygen concentration of mainstream-coolant mixture at the wall

$\left(C_{o_2}\right)_{coolant}$ = Oxygen concentration of cooling flow

$\left(p_{o_2}\right)_{air}$ = Partial pressure of oxygen with air as the coolant

$\left(p_{o_2}\right)_{mix}$ = Partial pressure of oxygen with N_2 or CO_2 as the coolant

$\left(p_{o_2}\right)_{ref}$ = Partial pressure of oxygen at reference state

Abbreviation

BDA = Barchan-dune-assisted

BDSR = Barchan-dune-shaped ramp

BDSIC = Barchan-dune-shaped injection compound

CRV = Counter rotating vortex

MW = Molecular weights ratio of the coolant gas to mainstream

WBD = With Barchan dune

WOBD = Without Barchan dune

ACKNOWLEDGEMENTS

I would like to express my sincere appreciation to my supervisor Dr. Hui Hu, whose expertise, enthusiasm, support and patience greatly contributed to the success of this study. Without his generous guidance, this dissertation would not be possible. My appreciation also goes to the committee members, Dr. Alric P. Rothmayer, Dr. Anupam Sharma, Dr. Xinwei Wang, and Dr. Xiaoli Tan for evaluating my research work and giving me many insightful comments.

I would like to extend my gratitude to the members of Advanced Flow Diagnostics and Experimental Aerodynamics Lab, especially Dr. Blake E. Johnson and Dr. Kai Zhang for many helpful discussions and suggestions on film cooling study. I would like to thanks Mr. Maxwell Person for proofreading my thesis. Further thanks to the staffs of Aerospace Engineering, Mr. Bill Richard and Mr. Andrew Jordan for their continuous help on setting up my experimental facilities.

Most importantly, I would like to thank my friends and family. Especially my wife Ting, her love and encouragement make me able to overcome the difficulties in my life. Deepest appreciation is reserved for my parents, Chengliang Zhou, Jinhua Zou, thanking for their unconditional love and support throughout my life.

ABSTRACT

Modern gas turbines are operating at peak turbine inlet temperature well beyond the maximum endurable temperature of turbine blade material. As a result, hot gas-contacting blades or vanes have to be cooled intensively by using various cooling technologies, such as film cooling and internal cooling, in order to increase the fatigue lifetime of the engine.

In the present study, a series of experimental investigations were conducted to explore innovative cooling strategies for improved exterior and interior cooling of gas turbine blades. For the exterior cooling, the effectiveness of novel film cooling designs with coolant injection from Barchan-Dune-Shaped ramp (BDSR) and Barchan-Dune-Shaped injection compound (BDSIC) were evaluated in great detail, in comparison to that of conventional circular holes. While a high-resolution Particle Image Velocimetry (PIV) system was used to conduct detailed flow field measurements to quantify the dynamic mixing process between the coolant streams and the mainstream flows over the test plates, Pressure Sensitive Paint (PSP) technique was used to map the corresponding adiabatic film cooling effectiveness on the surface of interest based on a mass-flux analog to traditional temperature-based cooling effectiveness measurements. The measured effectiveness maps were correlated with the characteristics of the flow structures revealed from the detailed PIV measurement in order to elucidate underlying physics to explore/optimize design paradigms for a better protection of the critical components of turbine blades.

Beside exploration of novel cooling designs for film cooling, an experiment was performed to examine the compressibility effect on film cooling effectiveness by using

PSP and PIV technique. The experimental studies were conducted in a transonic, open-circuit wind tunnel located at Iowa State University. The measured effectiveness revealed that the mainstream compressibility has limited effect on film effectiveness, and the effectiveness of transonic speed flow can be studied in a relative low-speed wind tunnel.

Pertinent to interior cooling of turbine blades, finally, an experimental investigation was also conducted to quantify the characteristics of the turbulent boundary layer flows over a dimpled surface. Many interesting flow features over the dimpled surfaces, such as the separation of incoming boundary layer flow at the dimple front rim, the formation and shedding of unsteady Kelvin-Helmholtz vortices over the dimple cavity, the impingement of the high-speed incoming flow onto the back rim of the dimple, and the generation of strong upwash flow over the back rim of dimple, were revealed clearly and quantitatively. This was found to correlate well with the enhanced heat transfer performance of dimpled surface design reported in previous studies.

CHAPTER 1

GENERAL INTRODUCTION

1. Background and Motivation

Gas turbine engines have become an essential part of our daily lives. Due to the widespread application of gas turbines in different fields, such as power and transportation, there is a great incentive to maximize the performance of engines for both economic and environmental reasons. Improvements of engine efficiency, even if by marginal increments, will lead to a significant amount of savings. Thermodynamic analysis reveals that thermal efficiency and power output of a gas turbine can be further improved through higher turbine inlet temperatures. This is vividly illustrated in Figure 1 (collected in Han *et al*.[1]). It is clear that the specific core power is as function of turbine inlet temperature, higher temperature leading to enhanced power. The ideal performance line represents a 100% efficient power output without leakage or coolant loss, which is impossible to achieve. However if the coolant consumptions are well controlled, the engines performance tends to follow the performance line fairly close. Obviously, increasing turbine inlet temperature is one of the key technologies to achieve better turbine performance.

Advanced gas turbines are operating at peak turbine inlet temperature (as high as 1700ºC), which are well beyond the maximum endurable temperature of blade. Figure 2 shows the variation of turbine entry temperature over recent years, collected in Han *et al*.[1]. Over the last 40 years, it is clear that the inlet temperature was found to increase dramatically from the melting point to far-beyond the permissible conditions. As a result,

hot gas-contacting turbine blades have to be cooled intensively by using various cooling techniques, such as external cooling and internal cooling, in order to ensure a good structural integrity of the blades. External cooling, also named film cooling, is achieved by releasing a film of coolant gas on the airfoil surface to isolate the components from the hot gases in the turbine stage. Internal cooling uses coolant air to remove the waste heat from an internal channel, which is accomplished by a variety of cooling techniques, such as impingement cooling at the leading edge, forced convective cooling in the mid-chord region, and pin-fin cooling at near the trailing edge of blade.

The cooling techniques in gas blade is highly sophisticated, including film cooling, impingement cooling, forced convective cooling. Figure 3 shows various cooling methods for a turbine blade. Normally, the coolant comes from the compressor and impinges on the inner wall of the blade, then it passes through complicated channels, finally the spent gas injects out through cooling holes to provide film cooling. Obviously, this process is a combination of both external and internal cooling, which is the core technique to meet the extremely harsh environment inside engine.

1.1 Film cooling.

Film cooling: a film of coolant covers on the surface of the blade to protect it from eroding and melting. The overall goal of turbine cooling is to reduce the amount of heat transferring from the hot gas to the blade surface, since higher metal temperature leads to reduced lifetime for components. A simple relationship can be used to assess the net heat flux reduction (Δq_r) due to the appearance of film cooling. Please refer to the paper by Bogard and Thole [3] for more information.

$$\Delta q_r = 1 - \frac{h_f}{h_0}\left(\frac{1-\eta}{\phi}\right) \tag{1}$$

$$\eta = \frac{T_\infty - T_{aw}}{T_\infty - T_{c,exit}} \tag{2}$$

Where h_f is the heat transfer coefficient with film cooling, h_0 is the heat transfer coefficient without film cooling, η is the film cooling effectiveness, and ϕ is a non-dimensional parameter for actual metal temperature. Larger magnitude of heat flux reduction Δq_r means increased amount of heat was removed by the film cooling process, and vice versa. The heat transfer coefficient $h_f = q^{"}/(T_{aw} - T_w)$ is closely tied to the adiabatic temperature T_{aw}, which can be derived from the film cooling effectiveness. Therefore, in order to calculate the net heat flux reduction, the effectiveness of film cooling is an unavoidable parameter that need to be studied first.

As shown in Eq. (2), the film cooling effectiveness is defined based on temperature difference ratios, which can be used to characterize the coolant coverage on the surface of the blade. In general, experimental study of film effectiveness can be classified into two categories: isothermal and non-isothermal methods. Non-isothermal methods are based on conventional thermal measurement, such as thermocouples [4], liquid crystal thermometry [1], infrared thermography [5,6], and Temperature Sensitive Paint (TSP) [7], to measure the surface temperature and then compute the effectiveness. Though it is straightforward to reveal useful information of film cooling effectiveness, there always exist concerns regarding the adiabaticity of the wall temperature measurement due to effects of heat conduction within the test plate. However, isothermal methods—such as the Pressure Sensitive Paint (PSP) technique [8]—can successfully eliminate errors due to conduction

since they are based on a mass transfer analog to the temperature ratio, freeing the measurement of any questions about heat conduction. The *Lewis number* ($Le = \alpha/D_s$) is around one at atmospheric pressure, which means the thermal boundary layer and concentration boundary layer are of the same order, so that the differential equations involving heat and mass transfer can be treated as analogous [7,9,10].

For PSP measurements, the surface of the test model was coated with an oxygen-sensitive paint layer (ISSI UniFIB). The paint consists of light-sensitive molecules called luminophores mixed into a gas-permeable polymeric binder. When the luminophores are exposed to UV light, they are excited and emit light at 650 nm wavelength. However, in the presence of diatomic oxygen gas the excited electrons return to their ground state via a radiationless transition. This process is called oxygen quenching [8], where the intensity of the photoluminescence is inversely proportional to the concentration of local oxygen. Consequently, the concentration of oxygen against the interested surface can be calculated by recorded light intensity through the using of calibrated curve. Applying the concentrations of oxygen rather than the temperature into Eq. (2), the adiabatic cooling effectiveness can be expressed as Eq. (3), as described by Charbonnier *et al* [11], where *MW* is the ratio of molecular weights of the coolant gas to the freestream gas.

$$\eta = 1 - \frac{1}{\left[\left(\left(p_{o_2}\right)_{air} / \left(p_{o_2}\right)_{mix}\right)_{wall} - 1\right] MW + 1} \tag{3}$$

The pressures in Eq. (3) can be computed using the recorded intensity of emission light, which is directly related to the partial pressure of oxygen. The mathematical function between normalized intensity and partial pressure can be obtained through a dedicated PSP calibration process.

Figure 4 depicts the experimental setup for PSP calibration. A test plate painted with PSP paint was mounted in an enclosed test cell. The paint chosen for the present study is ISSI Uni-FIB which has a low temperature sensitivity (~0.5%/ºC). A constant temperature thermal bath system was used to control the temperature of the copper plate mounted inside the test cell. During the calibration experiment, a vacuum pump was employed to depressurize the test cell. The pressure within the test cell was measured with a digital sensor array (DSA 3217 Module, Scanivalve Corp). A reference pressure of atmospheric pressure was used in the present study, which corresponds in the wind tunnel experiments to a condition of η=0. Since it is feasible that some experiments might indicate a possible maximum of η=1.0 locally, corresponding to a true zero absolute O_2 pressure, it is necessary to calibrate for this condition rather than rely upon calibration curve extrapolation. For this data point the cell was flushed with pure CO_2 until the PSP emission reached a steady value.

As for the uncertainty measurement of PSP technique, please refer to the individual chapter for detailed information.

The effectiveness of film cooling is affected by a series of physical parameters [3]: mass flux ratio (*M*), momentum ratio (*I*), density ratio (*DR*), turbulence intensity, shape of hole, and so on, shown in Table 1. In the present study, our research interest is mainly focused on the exploration of innovative holes for better film cooling performance.

Various types of cooling holes can be found in literatures, including slots, circular holes, shaped holes, and new cooling concepts, that aim to reduce the coolant consumption while provides necessary cooling for turbine. Film cooling studies of using slots, typically not practical for turbine airfoil due to the unbalanced thermal stress, were summarized

clearly by Goldstein [12]. Circular holes are probably the most widely used configuration for turbine cooling, which have been studied comprehensively, especially the basic cooling configuration. This configuration consists of a row of circular holes on flat plate [1,3,13,5–7]. Besides the circular holes, the exploration of shaped holes are one of the long lasting research topics in film cooling. Goldstein *et al.* [14] firstly reported a remarkable increment of film cooling performance by using fan-shaped holes. Similar results were obtained by Schmidt *et al.* [15], who studied compound angle shaped hole. Other ideas such as anti-vortex hole (Heidmann *et al.* [16] and Dhungel *et al*. [17]), console-shaped hole (Sargison *et al.* [18]), trenched holes (Bunker [19]), crescent-shaped hole (Lu *et al*. [20]), and yaw angle double-row holes (Gräf and Kleiser [21]) were proposed and studied, which showed effective test results. Shaped holes provide a promising solution for film cooling, except the concern of structure strength reduction hinders the applications in certain situations.

The appearance of 3D-printing technology has greatly promoted the development of film cooling design concepts. Many innovative but unmachinable design concepts can now be printed as a whole part at the engine scale, including the shaped hole and other new cooling concepts such as placing a ramp upstream or downstream of coolant hole. Zaman and Foss [22] studied the effect of triangular tabs on jet in cross flow. A similar study was conducted by Zaman *et al*. [23] and Shinn *et al*. [24] using micro-ramp. Other studies like ramp (Na and Shih [25]) and spherical bumps (Sakai *et al*. [26]) were investigated in great detail. Most of the presented designs are shown to be effective in improving the performance, however the majority of these ideas produce an unwanted sharp edge that has aerodynamic liabilities or additional surfaces that are difficult to cool.

Barchan dunes are commonly-seen features on Earth. They have a streamlined shape along the wind flow direction, featured by a crescentic platform with two gradually-widened horns pointing downstream [27,28]. When airflow passes over it, symmetric vortex structures would be formed behind the dune. Due to its unique shape, the continual suction induced by the vortices generates a "quiet" wake flow behind the dune. As a result, sand particles can settle down on the ground behind the dune, instead of being blown away by the incoming flow. Inspired by the unique shape and characteristics of the Barchan dune, we proposed Barchan-dune-shaped ramp (BDSR) and injection compound (BDSIC) for film cooling. Similar as the sand particles settling down on the ground behind the dune, the coolant streams exhausted from new holes will be able to provide a better film protection to the surface.

The objective of the present study is to develop novel cooling strategies for better cooling performance, and also to understand the underlying physics of film cooling. Therefore, a series of experiments were conducted to evaluate the effectiveness of film cooling using PIV and PSP techniques, in comparison to circular hole as the baseline. The effects of geometrical parameters, mass flux ratios, and density ratios on the cooling effectiveness were examined in great detailed. The PIV measurements were correlated with the adiabatic cooling effectiveness maps to reveal inherent physics in order to optimize/explore design paradigms for improved film cooling effectiveness and to protect the crucial components of turbine blades from harsh environments.

1.2 Internal cooling.

In reality, turbine rotors and stators are usually hollow, particularly the first several stages that suffer the most severe hot gas from the combustion. Hollowed blades and vanes are equipped with mazy channels, where many techniques have been developed to enhance the heat transfer of passages. The rib turbulators are often lined inside the passages at the middle of airfoil. Around the leading edge of blade, jet impingement is commonly used. Due to the limited space, pin-fins and dimples are utilized in the trailing edge part of blades. Han and Wright [29] provided a decent literature review of internal cooling of turbine blades.

Recently, dimple arrays have become a magnet in forced convective heat transfer studies [29–39]. Due to the relatively low pressure loss penalties and moderate heat transfer augmentation in comparison to pin-fins cooling, a dimpled surface (i.e., a flat surface with dimple arrays) provides a desirable alternative for the internal cooling of turbine blades, especially in the rear regions of turbine blades.

A number of experimental and numerical studies have been conducted in recent years to investigate heat transfer augmentation performance of dimpled surfaces [31–35,38]. Han *et al.*[29] and Ligrani [37] provide a comprehensive overview of the current state of the art of internal airfoil cooling techniques that are mainly applicable in turbine blades and components. It was found that the heat transfer performance of a dimpled surface is greatly affected by the configuration of the dimples, including dimple diameter, dimple depth ratio, distribution pattern and shape of the dimples. Mahmood *et al*. [33] and Ligrani *et al*. [31] studied the local heat transfer and flow structures over dimpled surfaces experimentally with Reynolds numbers changing from 1,250 to 61,500. Based on

qualitative flow visualization, Ligrani *et al*. [31] suggested that unsteady vortex structures shedding from dimples would enhance the turbulent mixing between the mainstream coolant flow and the hot flow inside the dimple cavity. Mahmood and Ligrani [38] conducted an experimental study to investigate the combined influences of channel height ratios (0.2, 0.25, 0.5 and 1.0), temperature ratios (0.78~0.94), Reynolds number (600~11,000) and flow structures on the heat transfer process over dimpled surfaces. A separate experimental and numerical study by Rao *et al.* [34] concluded that the teardrop dimples exhibit about 18% higher heat transfer ratio than dimples.

Many findings have been revealed through previous studies, however most of those studies focused on the global features of enhanced heat transfer over dimpled surfaces, very few can be found in literature to provide detailed flow field measurements to quantify the unique characteristics of flows over dimpled surface. While the unsteady vortex structures generated inside dimples were suggested to play a very important role for the heat transfer augmentation over dimpled surfaces [31,33,39], most of the previous studies were conducted by using smoke wires to qualitatively visualize the unsteady vortex structures over dimpled surfaces, no quantitative measurements have ever been available to characterize the evolution of the unsteady vortex structures. Such quantitative information is highly desirable to elucidate underlying physics for improved heat transfer performance of dimpled surfaces.

The objective of the internal cooling study was to quantify the characteristics of turbulent boundary layer flows over dimpled surface, and to correlate the measured flow field with the heat transfer coefficient to gain further insight into underlying physics to explore better internal cooling designs.

2. Outline of Thesis

The dissertation is consisted of six chapters, and four of them (Chapter 2-5) are in journal paper format, Chapter 1 is a general introduction and Chapter 6 gives the conclusion. An Appendix is included at the end of thesis to discuss uncovered material by the main chapter. Noting that some repetition might be found throughout the dissertation due to its format.

The first paper (Chapter 2) studied the cooling performance of proposed Barchan-dune-shaped ramp located either upstream or downstream of the coolant hole. The PSP technique was used to map the adiabatic effectiveness of film cooling over a flat surface. In order to understand the coolant behavior, both PIV and sPIV techniques were utilized to conduct detailed flow field measurements. The effects of the mass flux ratio, dune location, and height of dune on film cooling effectiveness were examined in great detail.

The second paper (Chapter 3) investigated the adiabatic cooling effectiveness of Barchan-dune-shaped Injection Compounds (BDSIC), upgraded from Barchan-dune shaped ramp. The effectiveness of BDSIC, in comparison to circular hole, was measured by PSP technique in order to study the dune shape effect, mass flux ratio effect, and hole interaction effect on film effectiveness. A high resolution PIV system was used to study the counter-rotating vortex structures in order to explain the unique film distribution on flat plate. In addition, the aerodynamic loss coefficient was studied to uncover the nature of loss generated in BDSIC film cooling.

The third paper (Chapter 4) examined the compressibility effect on film cooling effectiveness by using PSP and PIV technique. The experimental studies were conducted

in a transonic, open-circuit wind tunnel located at the Department of Aerospace Engineering of Iowa State University.

The fourth paper (Chapter 5), which studied the characteristics of turbulent boundary layer flows over dimpled surface, belongs to the internal cooling field. The friction factors of a test plate and pressure distribution inside dimple were determined first, then a high-resolution PIV system was used to achieve detailed flow filed measurement to quantify the flow character and the evolution of unsteady vortex structures inside the cavity. Many interesting flow features over the dimpled surfaces, such as the separation of incoming boundary layer flow at the dimple front rim, the formation and shedding of unsteady Kelvin-Helmholtz vortices over the dimple cavity, the impingement of the high-speed incoming flow onto the back rim of the dimple, and the generation of strong upwash flow over the back rim of dimple, were revealed clearly and quantitatively. This was found to correlate well with the enhanced heat transfer performance of a dimpled surface design reported in previous studies.

Reference

[1] Han, J., Dutta, S., and Ekkad, S., 2012, Gas turbine heat transfer and cooling technology, Taylor and Francis, New York.

[2] Xie, G., Sundén, B., and Zhang, W., 2011, "Comparisons of Pins/Dimples/ Protrusions Cooling Concepts for a Turbine Blade Tip-Wall at High Reynolds Numbers," J. Heat Transfer, **133**(6), p. 061902.

[3] Bogard, D. G., and Thole, K. A., 2006, "Gas Turbine Film Cooling," J. Propuls. Power, **22**(2), pp. 249–270.

[4] Ou, S., Han, J.-C., Mehendale, A. B., and Lee, C. P., 1994, "Unsteady Wake Over a Linear Turbine Blade Cascade With Air and CO2 Film Injection: Part I—Effect on Heat Transfer Coefficients," J. Turbomach., **116**(4), p. 721.

[5] Baldauf, S., Schulz, A., and Wittig, S., 2001, "High-Resolution Measurements of Local Effectiveness From Discrete Hole Film Cooling," J. Turbomach., **123**(4), p. 758.

[6] Baldauf, S., Scheurlen, M., Schulz, A., and Wittig, S., 2002, "Correlation of Film-Cooling Effectiveness From Thermographic Measurements at Enginelike Conditions," J. Turbomach., **124**(4), p. 686.

[7] Wright, L. M., Gao, Z., Varvel, T. A., and Han, J.-C., 2005, "Assessment of Steady State PSP, TSP, and IR Measurement Techniques for Flat Plate Film Cooling," Heat Transfer: Volume 3, ASME, pp. 37–46.

[8] Bell, J. H., Schairer, E. T., Hand, L. A., and Mehta, R. D., 2001, "SURFACE PRESSURE MEASUREMENTS U SING LUMINESCENT COATINGS 1," Annu. Rev. Fluid Mech., **33**(1), pp. 155–206.

[9] Eckert, E. R. G., 1992, "Similarity analysis of model experiments for film cooling in gas turbines," Wärme- und Stoffübertragung, **27**(4), pp. 217–223.

[10] Shadid, J. N., and Eckert, E. R. G., 1991, "The Mass Transfer Analogy to Heat Transfer in Fluids With Temperature-Dependent Properties," J. Turbomach., **113**(1), p. 27.

[11] Charbonnier, D., Ott, P., Jonsson, M., Cottier, F., and Köbke, T., 2009, "Experimental and Numerical Study of the Thermal Performance of a Film Cooled Turbine Platform," Proc. Asme Turbo Expo 2009, Vol 3, Pts A B, pp. 1027–1038.

[12] Goldstein, R., 1971, "Film cooling," Advances in heat transfer 7.1, pp. 321–379.

[13] Bogard, D. G., 2006, "Airfoil film cooling," The Gas Turbine Handbook, National Energy Technology Laboratory, Section 4.2.2.1.

[14] Goldstein, R. J., Eckert, E. R. G., and Burggraf, F., 1974, "Effects of hole geometry and density on three-dimensional film cooling," Int. J. Heat Mass Transf., **17**(5), pp. 595–607.

[15] Schmidt, D. L., Sen, B., and Bogard, D. G., 1996, "Film Cooling With Compound Angle Holes: Adiabatic Effectiveness," J. Turbomach., **118**(4), p. 807.

[16] Heidmann, J. D., and Ekkad, S., 2008, "A Novel Antivortex Turbine Film-Cooling Hole Concept," J. Turbomach., **130**(3), p. 031020.

[17] Dhungel, A., Lu, Y., Phillips, W., Ekkad, S. V., and Heidmann, J., 2009, "Film Cooling From a Row of Holes Supplemented With Antivortex Holes," J. Turbomach., **131**(2), p. 021007.

[18] Sargison, J. E., 2001, "Development of a Novel Film Cooling Hole Geometry," PhD Dissertation, Dept. of Engineering Sci., University of Oxford.

[19] Bunker, R. S., 2002, "Film Cooling Effectiveness Due to Discrete Holes Within a Transverse Surface Slot," Volume 3: Turbo Expo 2002, Parts A and B, ASME, pp. 129–138.

[20] Lu, Y., Faucheaux, D., and Ekkad, S. V., 2005, "Film Cooling Measurements for Novel Hole Configurations," ASME 2005 Summer Heat Transfer Conference collocated with the ASME 2005 Pacific Rim Technical Conference and Exhibition on Integration and Packaging of MEMS, NEMS, and Electronic Systems, ASME, pp. 59–66.

[21] Gräf, L., and Kleiser, L., 2014, "Film Cooling Using Antikidney Vortex Pairs: Effect of Blowing Conditions and Yaw Angle on Cooling and Losses," J. Turbomach.

[22] Zaman, K. B. M. Q., and Foss, J. K., 1997, "The Effect of Vortex Generators on a Jet in a Cross-Flow," Phys. Fluids, **9**, pp. 106–114.

[23] Zaman, K. M., Rigby, D., and Heidmann, J., 2010, "Inclined Jet in Crossflow Interacting With a Vortex Generator," J. Propuls. Power, **26**(5), pp. 947–954.

[24] Shinn, A. F., and Pratap Vanka, S., 2013, "Large eddy simulations of film-cooling flows with a micro-ramp vortex generator," J. Turbomach., **135**(1), p. 011004.

[25] Na, S., and Shih, T., 2007, "Increasing adiabatic film-cooling effectiveness by using an upstream ramp," J. Heat Transfer, **129**(4), pp. 464–471.

[26] Sakai, E., Takahashi, T., and Agata, Y., 2013, "Experimental Study on Effects of Internal Ribs and Rear Bumps on Film Cooling Effectiveness," J. Turbomach., **135**(3), p. 031025.

[27] Palmer, J. A., Mejia-Alvarez, R., Best, J. L., and Christensen, K. T., 2011, "Particle-image velocimetry measurements of flow over interacting barchan dunes," Exp. Fluids, **52**(3), pp. 809–829.

[28] Christensen, K. T., Kazemifar, F., Blois, G., Barros, J. M., Tang, Z., Hamed, A., Kim, T., and Best, J. L., 2014, "Quantitative Studies of Environmental Flows at the Micro- and Macro-Scales," 16th International Symposium on Flow Visualization, Okinawa, Japan.

[29] Han, J., and Wright, L., 2006, Enhanced internal cooling of turbine blades and vanes, The Gas Turbine Handbook.

[30] Han, J., Dutta, S., and Ekkad, S., 2012, Gas turbine heat transfer and cooling technology, Taylor and Francis, New York.

[31] Ligrani, P. M., Harrison, J. L., Mahmmod, G. I., and Hill, M. L., 2001, "Flow structure due to dimple depressions on a channel surface," Phys. Fluids, **13**(11), pp. 3442–3451.

[32] Xie, G., Liu, J., Ligrani, P. M., and Zhang, W., 2013, "Numerical Predictions of Heat Transfer and Flow Structure in a Square Cross-Section Channel with Various Non-Spherical Indentation Dimples," Numer. Heat Transf. Part A Appl., **64**(3), pp. 187–215.

[33] Mahmood, G., Hill, M., Nelson, D., and Ligrani, P., 2001, "Local heat transfer and flow structure on and above a dimpled surface in a channel," J. Turbomach., **123**(1), pp. 115–123.

[34] Rao, Y., Feng, Y., Li, B., and Weigand, B., 2014, "Experimental and Numerical Study of Heat Transfer and Flow Friction in Channels With Dimples of Different Shapes," J. Heat Transfer, **137**(3), p. 031901.

[35] Rao, Y., Xu, Y., and Wan, C., 2012, "A Numerical Study of the Flow and Heat Transfer in the Pin Fin-Dimple Channels With Various Dimple Depths," J. Heat Transfer, **134**(7), p. 071902.

[36] Moon, H. K., O'Connell, T., and Glezer, B., 2000, "Channel Height Effect on Heat Transfer and Friction in a Dimpled Passage," J. Eng. Gas Turbines Power, **122**(2), pp. 307–313.

[37] Ligrani, P., 2013, "Heat transfer augmentation technologies for internal cooling of turbine components of gas turbine engines," Int. J. Rotating Mach.

[38] Mahmood, G., and Ligrani, P., 2002, "Heat transfer in a dimpled channel: combined influences of aspect ratio, temperature ratio, Reynolds number, and flow structure," Int. J. Heat Mass Transf., **45**(10), pp. 2011–2020.

[39] Ligrani, P. M., Oliveira, M. M., and Blaskovich, T., 2012, "Comparison of Heat Transfer Augmentation Techniques," AIAA J., **41**(3), pp. 337–362.

Table 1. *Factors affecting the film cooling effectiveness* [3].

Coolant/mainstream conditions	Hole geometry and configuration	Blade geometry (Cascade)
Mass flux ratio	Shape of hole	location and distribution of holes
Density ratio	Injection angle, compound angle	Leading edge and blade tip, so on
Momentum flux ratio	Hole spacing and entry length	Surface roughness
Mach number Rotation	Spacing between rows	Curvature of blade

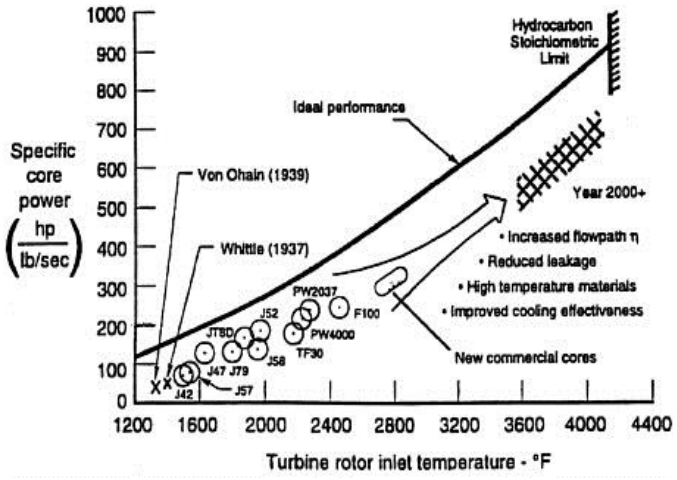

Figure 1. *Increased turbine inlet temperature dramatically improves cycle power output (Sautner et al. 1992; collected in Han et al.[1]).*

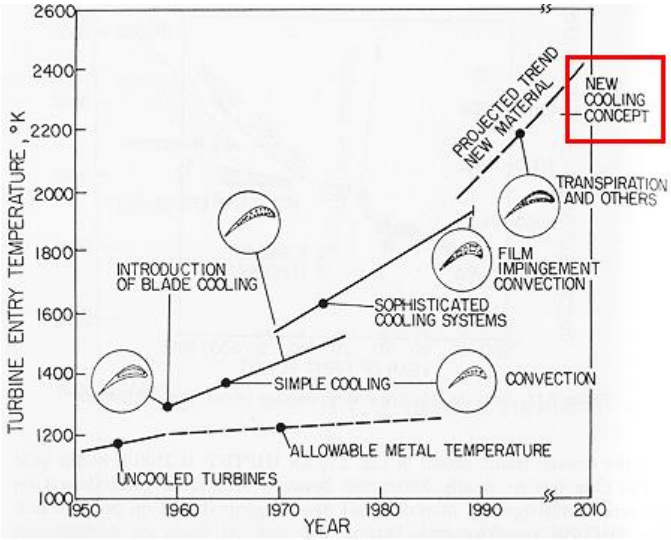

Figure 2. *Variation of turbine entry temperature over recent years (Lakshminarayana,1996; collected in Han et al.[1]).*

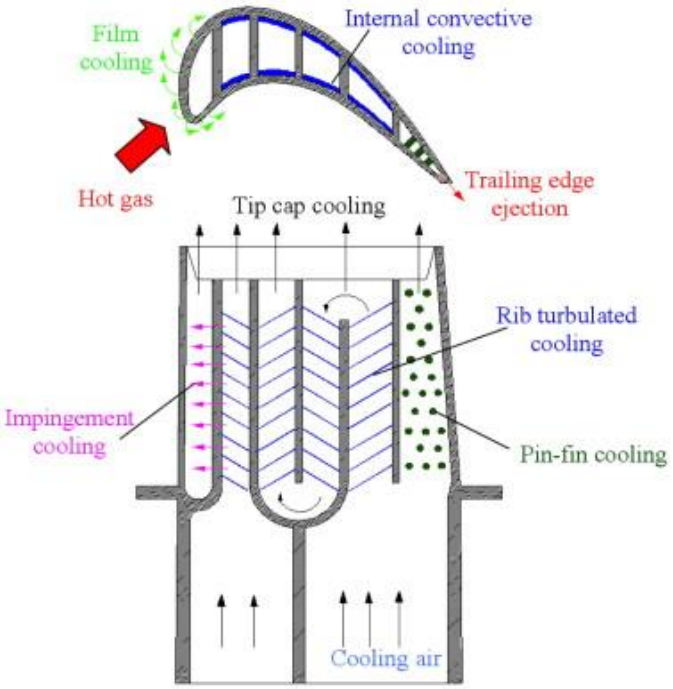

Figure 3*. Various cooling methods for a turbine blade (Xie et al.*[2]*).*

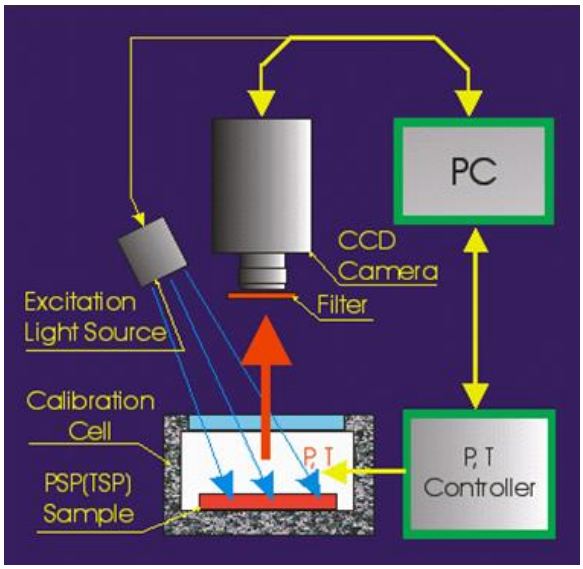

Figure 4. *Experimental setup for PSP calibration.*

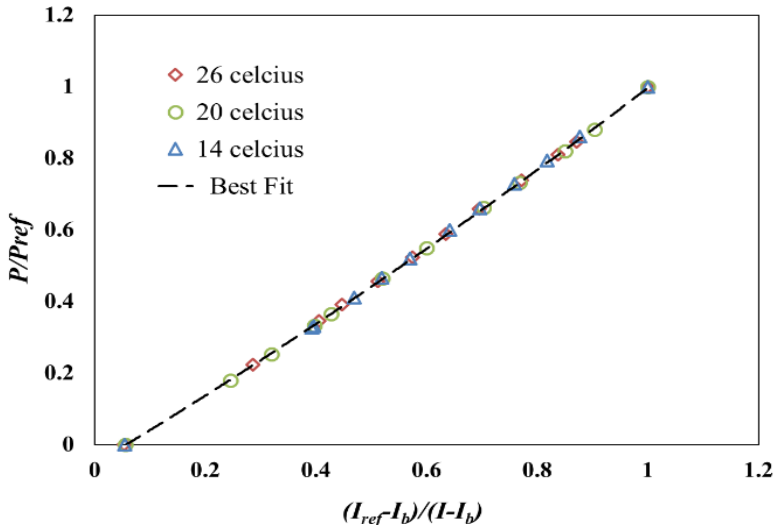

Figure 5. *The calibration curve for PSP measurements.*

CHAPTER 2

IMPROVEMENTS OF FILM COOLING EFFECTIVENESS BY USING BARCHAN-DUNE-SHAPED RAMPS

Wenwu Zhou and Hui Hu

Department of Aerospace Engineering, Iowa State University, Ames, IA 50011, USA

ABSTRACT

Inspired by the unique shape of Barchan dune to prevent sand particles on the ground from being blown away by the oncoming airstream, a Barchan-dune-assisted (BDA) film cooling concept was proposed and examined in present study. The film cooling performance behind Barchan-dune-shaped ramps had been studied experimentally for a row of 35 degree angled holes on a flat plate using Pressure Sensitive Paint (PSP) and Particle Image Velocimetry (PIV) techniques. The effects of mass flux ratio, dune location, and height of dune on film cooling effectiveness were studied in great detail. An improvement of 50%-100% in Area-averaged effectiveness was demonstrated for the BDA film cooling concept compared to the cylindrical hole. And the measured effectiveness behind Barchan dune was found to be closely related to both the location and height of the dune. Investigation of flow physics showed that the down-washing flow from Barchan dune suppressed the coolant streams and the Anti-CRV pair counteracted the vortex induction from coolant jet, allowing it to remain attached on the surface.

1. Introduction

Because of the widespread application of gas turbine engines in fields such as the power and transportation industries, there is a great incentive to maximize the performance

of turbine engines for both economic and environmental reasons. Improvements in gas turbine engine efficiency, even if by marginal increments, will lead to significant value of savings. Thermodynamic analysis reveals that thermal efficiency and power output of a gas turbine can be greatly enhanced through a higher turbine inlet temperature. Therefore means to protect the turbine components from corrosion and melting are essential, especially the implementation of film cooling technique. While coolant bleeds represent energy loss which should be minimized, gas turbine designers are seeking to optimize the film cooling efficiency without raising the consumption of coolant flow. Until now, substantial investigations have been conducted on film cooling techniques to better understand the inherent physics behind film cooling.

The film cooling effectiveness is affected by a series of physical parameters: mass flux ratio *(M)*, momentum flux ratio *(I)*, coolant to mainstream density ratio *(DR)*, turbulence intensity, morphology of the coolant hole, and so on. Comprehensive information can be found in archived documents such as Bogard [1,2] and Thole [1]. Using infrared thermography, Baldauf *et al.* [3,4] studied the influence of mass flux ratio and density ratio on film cooling behavior with a row of cylindrical holes. Wright *et al.* [5] conducted a PIV and PSP measurement to study the effect of freestream turbulence intensity on film cooling effectiveness. Besides the cylindrical hole, the researches of novel holes are one of the enduring research topics in film cooling. Goldstein *et al.* [6] firstly reported a remarkable enhancement of film effectiveness by using fan-shaped holes. Flow visualization and film cooling measurements both indicated that the secondary coolant jet from the shaped hole stayed close to the wall, unlike the coolant from circular hole which detached from the surface at higher blowing rates. Similar results were concluded by

Schmidt *et al.* [7], who studied a compound angle shaped hole. Lu *et al*. [8] measured the heat transfer and film cooling effectiveness of a crescent-shaped hole using IR thermography, which showed enhanced effectiveness. Sargison *et al.* [9] demonstrated an improved cooling performance and lower aerodynamic loss for console-shaped hole at certain mass flux ratios. Dhungel *et al*. [10] studied the cooling performance of an anti-vortex hole. They found that, at certain hole orientations, the designed hole exhibited a augmented film cooling performance due to the reduction of counter-rotating vortex (CRV) strength. More comprehensive comparisons of cooling behavior of these shaped holes can be found in the review paper by Bunker [11].

It is worth mentioning that the innovative holes discussed above not only include shaped holes, but also special configuration designs, such as placing a ramp upstream or downstream of coolant exit. Zaman *et al*. [12] experimentally studied an inclined jet-in-cross flow interacting with a vortex generator, which showed that the vortex generator produced a vorticity cancellation effect that postponed the jet lifting off from wall. Using large eddy simulation method, Shinn *et al*. [13] found that the strength of CRV associated with mainstream was reduced due to the exist of vortex generator, resulting in higher film cooling effectiveness. An *et al*. [14] conducted an experimental study to investigate the film cooling performance behind a crescent block. Their measurements showed that the cooling effectiveness behind block becomes larger within certain range of mass flux ratios. Na and Shih [15] performed a numerical study on placing ramp upstream of coolant hole, and found that ramp with backward-facing step can greatly enhance the film cooling effectiveness. Sakai *et al*. [16] experimentally studied the combined effects of internal ribs and downstream bumps (semicircular, hemispherical and cylindrical bumps) on film

cooling effectiveness. Their measurements showed that the cooling effectiveness of tested configurations is strongly affected by both the rib orientations and bump shapes. In general, the cooling effectiveness of these become greater under certain conditions in comparison with cylindrical hole.

A variety of ramps have been proposed through previous studies. Most of the ramps discussed above, however, present a sharp edge which could cause high skin friction and increase the aerodynamic loss. Barchan dunes are the most commonly-seen features in deserts, featured by arched crescent shape followed by two gradually-widened horns pointing downstream [17,18]. When airflow passes over it, symmetric vortex structures, as reported by Christensen *et al.*[19], would be formed behind a dune along the axis direction of the horns. Due to its unique shape, the continual suction induced by the vortices can create a "quiet" wake flow behind the dune. As a result, sand particles can settle down on the ground behind the dune, instead of being blown away by the oncoming airflow. Inspired by the unique shape of Barchan dune to prevent sand particles on the ground from being blown away by the oncoming airstream, a Barchan-dune-assisted (BDA) film cooling concept was proposed in present study. Similar as the sand particles settling down on the ground behind the dune, the coolant stream behind the Barchan dune will be able to stay on the surface and provide an enhanced cooling protection to the surface.

Advances in 3D-printing technology have greatly broadened the horizon of film cooling design concept, and many innovative but unmachinable hole designs can now be printed as a whole part at the engine scale (so does Barchan dune), which greatly promotes the development of film cooling technology. There are several advantages of using

Barchan-dune-assisted (BDA) film cooling instead of the aforementioned shaped hole in film cooling. First, BDA film cooling provides an alternative choice for special cases such as, space limitation inside engine, coolant injection angle constraint and endwall film cooling. It is possible to slightly increase the injection angle and satisfy the external cooling requirement by utilizing ramps to generate attraction between the coolant and the surface in order to drag down the coolant stream. Also, it offers a flexible plan for assisting the film cooling by either placing the dune at an upstream or downstream location relative to the coolant hole. Finally, the updating of old gas turbine cooling facilities become possible with the help of BDA film cooling. Since gas turbine components are coated with thermal coating, it is a practicable way to solve the 'heat problem' of outdated turbine by adding dunes made of thermal barrier coating.

Therefore, an experimental study was conducted to investigate the film cooling performance of a row of Barchan dunes located downstream or upstream of the coolant holes by leveraging the unique flow features of Barchan dunes. The objective of present study is to explore a novel dune-assisted film cooling design to produce wider and more stable coolant coverage over a test plate by taking advantage of vortex suction effects behind the Barchan dunes. During the experiments, a high-resolution Particle Image Velocimetry (PIV) system was used to conduct detailed flow field measurements to quantify the dynamic mixing process between the coolant jet and the mainstream flow. The Pressure Sensitive Paint (PSP) technique was used to map the adiabatic film cooling effectiveness on the surface of interest with and without Barchan dunes attached to the test plate. The effects of mass flux ratio, location, and height of Barchan dunes on the cooling performance were examined in great detail based on the quantitative PSP measurements.

The detailed PIV flow field measurements were correlated with the cooling effectiveness to elucidate the underlying physics in order to explore and optimize design paradigms for improved film cooling effectiveness.

2. Experimental Setup and Test Model

2.1 Experimental model and test rig.

The experimental studies were conducted in a low-speed, open-circuit wind tunnel located at the Department of Aerospace Engineering of Iowa State University. The tunnel has an optically-transparent test section with a cross section of 200 mm×125 mm and is driven by an upstream blower. With honeycombs and screen structures installed ahead of contraction section, the tunnel can supply uniform low-turbulence oncoming flow into the test section. The mainstream turbulence intensity of airflow in the test section was found to be about 1.5%, as measured by a hotwire anemometer.

In present study, all test models including test plate and Barchan dunes were made of hard ABS-like plastic material and manufactured by a rapid prototyping 3D-printer that built the models layer-by-layer with a resolution of about 25 microns. Figure 1 (a) shows the Barchan dune-assisted film cooling configuration, where the five dunes were affixed on the surface of the test plate by using a layer of 80 μm-thick double sided tape. For the cases without Barchan dunes, everything remains the same except for the removal of the dunes and, naturally, cleaning of tape adhesive residue. The span-wise pitch between adjacent holes is 3*D* center-to-center and the entry length of coolant hole is 4*D*. The coolant streams were injected through a row of five cylindrical holes with diameter

D=4mm at an injection angle 35° relative to the upper surface of the flat test plate. The test plate was mounted on a plenum chamber and sealed by a thin latex rubber gasket.

Figure 1 (b) shows the detailed dimensions of the Barchan dune used in present study, where *L* is the distance between the trailing edge of slip face and center of coolant hole. The height effect of Barchan dune on film cooling effectiveness was also investigated by using two types of dunes (case 1 & 2), which shared similar geometry other than the height different (*H*=0.3*D* and 0.5*D*). Due to the environmental diversity in deserts (i.e. wind strength, moisture, sand supply and so on), the sizes of developed dunes are found to vary in a wide range. Some could be as tall as 15 m high, or as small as several centimeters (such as on riverbed). The dune in present study was generated from a stereoscopic topographic map of idealized Barchan dune [20,21,17,22]. The shape of model truthfully reflected the curvature of dune encounter in deserts. Also the dimensions of the dune fell within the range of published data found in natural environments. The three-dimensional Barchan dunes were generated by the lofting command through Solidworks along three parabolic guidelines (obtained from actual scaled-down dune), which have two smooth surfaces in both of the windward side (convex face) and leeward side (concave face).

Figure 2 shows the schematic of the PSP experimental setup. A constant UV light (LM2X-DM, ISSI) with wavelength of 390 nm was used as the excitation source for the PSP measurements. A 14-bit (2048 pixel × 2048 pixel) charge-coupled device (CCD) camera (PCO2000, Cooke Corp.) fitted with a 610 nm long-pass filter was used to records the intensity of the photoluminescence light emitted by excited PSP molecules. The PSP paint used in the study was Uni-FIB provided by ISSI. This type of paint has a low sensitivity to temperature variation (~0.5%/°C) making it an ideal candidate for the study.

The tests were conducted in a room (~22˚C) where the temperature fluctuation was kept to a minimum. During the experiment, the mainstream flow from the wind tunnel was to simulate the hot gas in typical turbine stage. The test section had a constant speed of $U_\infty = 25$ m/s in the study. The coolant jet flow (CO_2 gas), supplied by a pressurized CO_2 gas cylinder (99.99% purity) with density ratio ($DR = \rho_c / \rho_\infty$) of 1.53, passed through control valves to enter the plenum chamber. A one-in.-wide 32 grit sand paper was employed at the leading edge of test section (i.e., 28*D* distance upstream of test plate) to trip the oncoming boundary layer to ensure a fully developed boundary layer flow over flat plate. The boundary layer profile was measured immediately upstream of the coolant holes (with no coolant flow), and was determined to resemble a fully-developed turbulent boundary layer with thickness of $\delta_{99} \approx 1.4D$, momentum thickness $\theta \approx 0.15D$ (corresponding $Re_\theta \approx 960$), and shape factor $H \approx 1.32$. The experiment was performed at four different mass flux ratios ranging between 0.40 and 1.25, defined as $M = \rho_c V_c / \rho_\infty V_\infty$.

2.2 Adiabatic film cooling effectiveness measurement using the PSP technique.

Adiabatic film cooling effectiveness η is traditionally expressed as,

$$\eta = \frac{T_\infty - T_{aw}}{T_\infty - T_c}, \quad (1)$$

where T_∞ is the temperature of the main-stream, T_{aw} is the adiabatic wall temperature of the surface under inspection, and T_c is the hole exit temperature of the coolant stream.

In this study, rather than conducting temperature measurements on the surface of interest (such as using thermocouples [23], liquid crystal thermometry [24], infrared

thermography [3,4] or Temperature Sensitive Paint (TSP) [25]), the effectiveness of film cooling was measured at isothermal conditions, using the PSP technique [26]. Based on mass transfer analogy, this method can eliminate the concerns and implications due to heat conduction through the test models on the adiabatic wall temperature measurements. When the value of the *Lewis number* ($Le = \alpha/D_s$) is about 1, the thermal boundary layer and concentration boundary layer thickness are of the same order. Therefore, the differential equations regarding heat and mass transfer can be treated as analogous [25,27,28], which is the case in present study ($Le \approx 1$).

For PSP experiments, the interested surface is coated with an oxygen-sensitive layer of paint. This paint consists of luminophores molecules hold together through gas-permeable polymeric binder. The luminophores molecules in PSP paint emit light when excited by certain UV light. But, the excited molecules will return to ground state via a reduced or radiationless emission in the presence of diatomic oxygen molecules. This process is called oxygen quenching [26], where the intensity of the photoluminescence is inversely proportional to the concentration of local oxygen. Consequently, the concentration of oxygen against the interested surface can be calculated by recorded light intensity through the using of calibrated curve. Applying the concentrations of oxygen rather than the temperature from Eq. (1), the adiabatic cooling effectiveness can be expressed as:

$$\eta = \frac{\left(C_{o_2}\right)_{main} - \left(C_{o_2}\right)_{mix}}{\left(C_{o_2}\right)_{main} - \left(C_{o_2}\right)_{coolant}} = \frac{\left(C_{o_2}\right)_{main} - \left(C_{o_2}\right)_{mix}}{\left(C_{o_2}\right)_{main}}. \tag{2}$$

For the choice of a coolant gas whose molecular mass differs greatly from that of the mainstream, the film cooling effectiveness as determined via measurement of the

concentrations of oxygen should be expressed as Eq. (3), as described by Charbonnier *et al* [29], where *MW* is the ratio of molecular weights of the coolant gas to the freestream gas.

$$\eta = 1 - \frac{1}{\left[\left(\left(p_{o_2}\right)_{air} / \left(p_{o_2}\right)_{mix}\right)_{wall} - 1\right] MW + 1}, \tag{3}$$

The pressures in Eq. (3) is computed using the recorded intensity of emission light, which is directly related to the partial pressure of oxygen. The mathematic function between normalized intensity and partial pressure can be obtained through a dedicated PSP calibration process. Detailed information on how to conduct PSP calibration can be found in papers, such as Wright *et al.*[25], Yang and Hu [30], Johnson *et al.*[31].

For the PSP image processing, in order to reduce the effects of camera noise on the measurements, spatial averaging was performed in the present study on square interrogation windows of 9×9 pixels with 50% overlap to ensure complete sampling of the measurement data. The acquired PSP images had a magnification of 0.07 mm/pix, a spatial resolution of 0.28 mm or 0.07*D* for the PSP measurements. The measurement uncertainty for the centerline effectiveness in the study is estimated to be of 3% for $\eta = 0.5$ and 5% for $\eta = 0.3$ (absolute uncertainty within $\Delta\eta$=0.02 throughout the entire interest). For laterally-averaged effectiveness, it is 7% for $\eta = 0.3$ and 10% for $\eta = 0.2$ (absolute uncertainty within $\Delta\eta$=0.03). These uncertainty are predicted based on Taylor Series Method [32–34]. Further PSP measurement uncertainty analysis can be found in Johnson and Hu [35].

2.3 Flow field measurements using the PIV and stereoscopic PIV (sPIV) technique.

A high-resolution Particle Image Velocimetry (PIV) system was used to conduct detailed flow field measurements to quantify the dynamic interaction and mixing processes between the coolant and mainstream flows over the test plate. Figure 4 shows the schematic of the experimental setup for the PIV measurement. During the experiment, the mainstream airflow and the cooling jets were seeded with ~1 μm oil droplets generated by a theatrical fog machine and an oil droplet generator, respectively. Illumination was provided by a double-pulsed Nd:YAG laser (NewWave Gemini 200) adjusted on the second harmonic and emitting two pulses of 200 mJ at the wavelength of 532 nm at a repetition rate of 10 Hz. Using a set of high-energy mirrors and optical lenses, the laser beam was shaped into a thin light sheet with a thickness in the measurement interest of less than 1 mm. The illuminating laser sheet was first aligned along the mainstream flow direction, bisecting the coolant hole in the middle of the test plate, to conduct PIV measurements in the *X*-*Y* plane. The laser sheet was then rotated 90 degrees to reveal the flow structures in the cross plane normal to the mainstream direction to perform sPIV measurements in the *Y*-*Z* planes at different locations downstream of the coolant exits.

For the sPIV measurements in the *Y*-*Z* planes, two high resolution 14-bit high-resolution CCD cameras (PCO2000, Cooke Corp.) was used for the sPIV image acquisitions. The two cameras were placed downstream of the test plate, with an angular displacement configuration (~45 degrees) to get a large overlapped view. With the installation of tilt-axis mounts, laser illumination plane, the lenses and camera bodies were adjusted to satisfy the Scheimpflug condition. The CCD cameras and double-pulsed Nd:YAG laser were both connected to a Digital Delay Generator (Berkeley Nucleonics,

Model 565), which controlled the time interval of the lasers and image acquisition. A general in-situ calibration procedure was conducted to obtain the mapping functions between the image planes and object planes for the sPIV measurements. A target plate (~150 × 100 mm^2) with 0.5 mm-diameter dots spaced at intervals of 1.0 mm was used for the in-situ calibration. The mapping function used in the present study was a multi-dimensional polynomial function, which is fourth order for the directions parallel to the laser illumination plane (i.e., *Y* and *Z* directions), and second order for the direction normal to the laser sheet plane (i.e., *X* direction). The coefficients of the multi-dimensional polynomial were determined from the calibration images by using a least-square method. For the PIV image processing, instantaneous PIV velocity vectors were obtained by using a frame-to-frame cross-correlation technique with an interrogation window size of 32 pixels ×32 pixels. An effective overlap of 50% of the interrogation windows was employed in PIV image processing, which results in a spatial resolution of 0.4 mm (0.1*D*) for the PIV measurement results. Similar process methodology was used for sPIV image processing, except a recursive interrogation window size changing from 64^2 pixels to 32^2 pixels was utilized for the sPIV processing to acquire the two-dimensional instantaneous velocity vectors. The acquired instantaneous vectors were then used to reconstruct all three components of the velocity vectors in the laser sheet planes through the mapping functions obtained by the calibration procedure. After the instantaneous velocity vectors (u_i, v_i, w_i) were determined, the distributions of the ensemble-averaged quantities such as mean velocity and normalized turbulence kinetic energy were obtained from a sequence of 1000 realizations of instantaneous vector fields. The measurement uncertainty level for the velocity vectors is estimated to be within 3%, while the uncertainties for the measurements

of ensemble-averaged flow quantities such as Reynolds stress and turbulent kinetic energy distributions are about 5%.

3. Results and Discussion

3.1 Verification of PSP technique.

Though a number of experimental studies have been conducted in recent years using the PSP technique to achieve quantitative effectiveness measurements, the PSP technique is still a fairly new technique in comparison to conventional temperature-based measurements. It is necessary to validate the reliability of the PSP measurements as an effective experimental tool for turbine blade film cooling studies. With this in mind, an experimental study was conducted to provide a quantitative comparison of the film cooling effectiveness by using PSP technique with mass transfer analogy against those derived directly from temperature-based measurements [7,36,37], which were under same or comparable test conditions. It is worth mentioning that the coolant streams from middle three holes were found to show a similar coolant coverage over the test plate. Therefore only the middle single jet contour was shown here for conciseness.

As shown clearly in Fig. 4, the measured centerline effectiveness in present study was found to agree with the temperature-based measurements well within the entire test plate (i.e., $2< x/D <30$). For the lateral-averaged effectiveness, though there was little difference at near the hole region, the general trend of measured results was consistent with the archived film cooling effectiveness. The discrepancy could be caused by the difference of spatial measurement resolutions that thermocouples can only provide limited number of discrete data points. Therefore, the PSP technique is a reliable method that can be used to

study the cooling performance behind Barchan dune ramp in present study. Noting that the lateral-averaged effectiveness was computed over a domain of -3< *z/D*<3, or two full periods of hole spacing pattern.

3.2 Effect of mass flux ratio on film effectiveness.

Figure 5 shows the comparison of film cooling effectiveness between the without Barchan dune (WOBD) and with Barchan dune (WBD) cases as a function of mass flux ratios over the flat surface. As shown clearly, the cooling performance of WBD case was found to be better than WOBD at relative large mass flux ratio (i.e., *M*>0.85), while there was limited effect for low mass flux ratio (i.e., *M*=0.40). When *M*=0.40, the effectiveness of WOBD case was slightly higher than that of WBD, indicating that the coolant jet from circular hole remained attached on the surface. As for WBD case, the coolant stream was trapped in the bay of Barchan dune. Due to the continual suction along the horns of dune, the very limited coolant gas would be forced to accumulate in the bay of dune rather than spread uniformly over the plate, therefore lead to shorter coolant coverage than WOBD configuration.

Increasing the mass flux ratio to 0.85, the lateral-averaged effectiveness of WBD started to exceed the WOBD, but the effectiveness of centerline dropped down in *x/D*>5 range. However as *M* >0.85, the effectiveness of the WBD completely surpassed WOBD, which showed an augmentation of 40-150% in lateral-averaged effectiveness than the original cases. These behaviors indicate that the high momentum jet of WOBD could have separated from the test surface and penetrated into the mainstream flow. While for the jet behind dune, the energetic coolant stream has escaped the ‘bay trap’ and spread widely in

spanwise direction. Therefore the BDA film cooling can largely improve the cooling effectiveness of circular hole, especially the lateral-averaged effectiveness, at relative high mass flux ratios.

3.3 PIV measurements for WOBD and WBD.

A high-resolution PIV system was used to conduct detailed flow field measurements to reveal the underlying physics pertinent to BDA film cooling in the region near the coolant jet, where the laser sheet was aligned along the middle plane of coolant hole (i.e., *X*-*Y* plane as shown in Fig. 3). Figure 6 shows the PIV measurements for WOBD and WBD assisted film cooling at M=0.40 and M=1.00 respectively, with corresponding velocity ratios (V_c / V_∞) of 0.26 and 0.66. The measured PIV results are in the terms of instantaneous vorticity field, mean velocity field, and normalized TKE $0.5\left(\overline{u'^2}+\overline{v'^2}\right)\Big/U_\infty^2$.

As shown clearly in Fig. 6 (a), a series of unsteady vortex structures were found to be generated and shed periodically from the interface of coolant jet and oncoming flow. It indicates that the jet flow was mixed intensively with the mainstream flow, which would dilute the potential of coolant as a heat sink to lower the blade mean temperature in gas turbine. Due to the velocity shear between the coolant and mainstream flows, packets of Kelvin-Helmholtz vortices were generated within the turbulent shear layer, shedding from either coolant exit or the crest of Barchan dune and dissipating in stream-wise direction. Similar flow features were seen for M=0.4, but only the instantaneous vorticity result of M=1.0 are shown here for conciseness.

The coolant jets of M=0.40 were found to stay attached on the surface as shown in Fig. 6 (b), but the streamlines in WOBD remained slightly closer to the surface, indicating that the cooling effectiveness of WOBD at M=0.40 should be higher, which is agreed with the measured PSP results. However, the velocity distribution changed completely as M increased to 1.00 [Figure 6 (c)]. The streamlines from the coolant jet of WOBD were found to lift off and penetrate into the mainstream flow, resulting in poor cooling effectiveness. Similar velocity distribution was found for WBD case, except the coolant flow was mildly diffused in the X–Y plane. If a jet's momentum is sufficient to overcome the penetration threshold, the attached stream would take off and penetrate into freestream flow. It is what happened in WOBD case at M=1.0. With the help of Barchan dune, the coolant jet would be, however, slightly pulled down toward the surface due to the continual lateral suction along the horns. As a result, the coolant flow from WBD would be slightly diffused. And the velocity field also reveals that a small stream was found to wash down from the crest of Barchan dune, suppressed on the coolant stream, leading to further diffusion of jet in flow direction. Consequently the film cooling effectiveness of WBD was higher than that of WOBD as shown in Fig. 5. What's more, it is interesting that the velocities of coolant exiting the holes were found to be less than that of WOBD for the cases where there were upstream dunes [Figure 6 (b) & (c)]. This could be attributed to the ramp disturbance and vortices suction behind the dune that to be discussed later.

Turbulence kinetic energy (*TKE*) is an important non-dimensional turbulent quantity that is often used as an index to evaluate the extent of turbulent mixing between the coolant stream and mainstream flow. A jet-in-cross-flow characterized with high *TKE* in real gas turbine could lead to enhanced heat transfer among hot gas and engine parts. Therefore,

special attention was paid to the *TKE* distribution of WOBD and WBD configurations. As shown in Fig. 6 (d), it is obvious that the *N.TKE* distributions demonstrate a strong interaction between the coolant and mainstream flow along the stream-wise direction, especially at the downstream of coolant flow. Because of the confluence of both the interactions of Mainstream–Barchan dune and Mainstream–Coolant, the WBD configuration exhibited slightly higher *TKE* level than WOBD case. Increasing *M* to 1.00, shown in Fig. 6 (e), the *TKE* distribution changed significantly that the area of high *TKE* moved from downstream location (at *M*=0.4) to the coolant exit, which was caused by the separation of coolant jets.

3.4 sPIV measurements for WOBD and WBD.

Film cooling as a state of art, fundamentally, is a jet-in-cross-flow (JICF) problem. The dominated features of a JICF configuration include jet shear-layer vortices formed at the leading edge of jet, horseshoe vortices around the jet, CRV pair in the jet, and wake vortices downstream of jet flow [38]. A major problem of film cooling technique is that the coolant jet tends to take off from blade surface, caused by vortex induction from the CRV. This leads to a deteriorated cooling performance in the engine. One method for improving the effectiveness is to reduce the negative effect of vortex induction by introducing a pair of Anti-CRV to control the strength of CRV from the coolant stream.

In the present study, a stereoscopic PIV measurement was conducted to investigate the vortex generation and evolution in WOBD and WBD assisted film cooling, results shown in Fig. 7, where the mainstream flow was directed in positive *X*-direction (inside the paper), and the plotted vectors were the resultant vectors of in-plane velocities (*V* and *W*).

As revealed clearly in Fig. 7(a), the CRV pair was found to be the salient flow structure for the WOBD case, where the near-wall coolant was ejected away so that an upwash flow was formed between the vortices. For the case with Barchan dune, a pair of Anti-CRV (similar phenomenon was reported by Zheng *et al.* [39] and Omidyeganeh *et al.* [40]), generated by the ramp, was captured in *Y-Z* plane besides the CRV, which had vorticity in opposite sign to CRV. When the incoming flow passes over the dune, the flow near the center plane of dune would climb over the crest, then interacts with the coolant jet and forms the CRV behind the dune. Away from the center of dune, the flow would impinge on the horns of dune, and part of the flow would stagnate there, while the rest would diverge and travel along the horn. As a results, the pressure at the stagantion area is much higher than the inner side of dune, therefore the flow would curl over the dune and generate the so-called Anti-CRV pair behind it. This process is similar to the formation of wingtip vortex. The generated vorticities can partially countervail the effect of vortex induction caused by the CRV, and therefore postpone the jet seperation. Due to the continuing entrainment of coolants from stream to surface, the Anti-CRV pair can create symetric downwash regions, resulting in wider coolant spread over the test surface. The velocity field also revealed that the distance between CRV cores of WBD was found to be elongated in lateral direction, which is believed to be caused by the rotation of Anti-CRV.

Comparing with WOBD case, a relative low velocity region (light blue) was found in WBD case in the near wall region. Such flow feature had been verified in Fig. 6. When the coolant was flushed out from the hole, it would interact with the mainstream at slightly higher postition since the upstream ramp would force the mainstream flow to deviate a little from its original path, leading to lower velocity ratio near the wall region. Also the

appearance of symmetric vortices in *X-Z* and *Y-Z* planes (shown in Fig. 8) facilitated the diffusion of gas in the bay of Barchan dune, whereby the velocity behind the dune was further reduced.

Figure 7 (b) shows the contours of vorticity evolution along the flow direction for WOBD and WBD cases at *X/D*=-1.3, 3, and 8. As shown clearly in these plots, the vorticity field of WOBD was characterized with a pair of CRV in the middle, and a pair of horeshoe vortex (*HV*) with lower vorticiy on the sides. These two pairs of structures were found to be the dominate features of inclined JICF for the WOBD case. Due to the dissipation of small eddies, the strength of vortices were decreasing along the streamise direction from *x/D*=3 to 8. Similar vorticity distribution was found in WBD case, which also held two pairs of coherent vortices. But, the strength of Anti-CRV in WBD was much stronger than that of *HV* in WOBD. Therefore, the Anti-CRV is like a enlarged *HV* that escorts the CRV and postpones the separation of coolant jet from the surface.

Figure 8 shows a schematic sketch of the flow features behind BDA film cooling configuration, which vividly illustrates the unique turbulent flow characteristics from the measured PIV results discussed above. As shown clearly in the sketch, the vortex structures behind Barchan dune were found to be highly three dimensional and featured by three pairs of symmetric vortices: CRV pair in the jet (*Y-Z* plane), Anti-CRV pair near the horns (*Y-Z* plane), and circulation vortex pair (*X-Z* plane) in the bay [19].

The CRV pair is formed by the strong shear interaction between the mainstream and coolant jet, which will generate detrimental vortex induction and promote the separation of jet stream. The Anti-CRV pair is generated by the rolling up of flow over the Barchan dune, as discussed in Fig. 7 (a). It is able to counteract the harmful vorticity effect

associated with coolant jet, therefore retard the detachment of jet from test surface. The circulation vortex pair is created by the low pressure attraction behind the dune, which results in the flow diverging and rotating inside the bay of dune. These vortices can generate continuous suction along the axis of horns and force the coolant to spread more uniformly on the surface. Therefore, the augmentation of the film cooling effectiveness is the result of both the down-wash effect and vortex pairs interactions behind the dune.

3.5 Influence of Barchan dune location.

The external cooling in gas turbine engine is achieved by thousands of arrays of cooling holes. One array of Barchan dunes placed upstream is located at the downstream of ahead array of cooling holes. Though the measured PSP results showed that the WBD case can enhance the effectiveness of cylindrical hole at higher mass flux ratio, it is necessary to address the effect of Barchan dune location on film cooling performance, which can help us determine the optimal configuration of BDA film cooling.

Figure 9 shows the effectiveness of film cooling as a function of distance (L) between Barchan dune and coolant hole at M=0.85 (left column) and 1.25 (right column). It is apparent that there is great difference between the film cooling contours achieved by placing the dune upstream and downstream of coolant hole. With the dune upstream, the cooling performance of L=-0.9D was better than that of L=-3.0D at M=0.85 and 1.25, because placing dune nearer the hole can maximize the use of downwash and vortex suction effects. With the dune downstream, the WBD configuration of L=3.4D exhibited higher effectiveness than the others. By analyzing the effectiveness of all the cases, the

L=-0.9*D* case was found to demonstrate the highest effectiveness at relative high *M*, followed closely by the *L*=3.4*D* case.

Figure 10 shows the PIV results with Barchan dune upstream (left column, *L*=-0.9D) and downstream (right column, *L*=3.4D) of coolant hole at *M*=1.0, where the corresponding velocity ratio (V_c / V_∞) is 0.66. For the *L*=-0.9*D* case, the aforementioned lateral suction and down-washing from the mainstream—both of whose strength are inversely proportional to the distance between dune and coolant hole, such that a shorter distance results in stronger lateral suction and down-washing—are the primary causes that lead to better coolant coverage. Placing the dune immediately ahead of the injection hole can enhance the performance of film cooling.

With the dune downstream (*L*=3.4*D* case), the streamlines from coolant were found to be attracted downward to the surface of dune, as revealed in Fig. 10 (a). It indicates, the Coanda effect, rather than the down-wash effect, is the primary reason for better cooling performance. If the coolant jet is treated as a rigid body and assumes little interaction with the mainstream flow, then the efflux jet angle from the hole would be 35º. The "gap" between jet and dune would be about 0.5*D* as coolant flows over it. In reality, this gap is much smaller taking account of gaseous diffusion and flow interactions. If the gap is sufficiently small, fluid jets will be bent to the nearby surfaces due to the Coanda effect, similar to what has observed here. And the TKE distributions of WBD for *L*=-0.9D and *L*=3.4D shown in Fig. 10 (b) indicate that the TKE level of the dune-upstream case was slightly higher than the dune-downstream case in the near hole region.

3.6 Influence of Barchan dune height.

Since the L=-0.9D and L=3.4D configurations discussed earlier exhibit higher film cooling performance, these two locations were chosen to study the height effect of Barchan dune by comparing the effectiveness of H=0.3D and 0.5D at corresponding positions. Up until now, all of the Barchan dunes discussed above have height of 0.5D.

As shown clearly in Fig. 11 (a), the dune upstream of H=0.5D was found to exhibit an improved cooling performance than H=0.3D at M=0.85 and 1.25, which was caused by the stronger downwash and suction effects in the taller case. It indicates that a higher height dune such as H=0.5D is a better choice for the upstream cases. Placing the dune downstream, the film cooling effectiveness of H=0.3D case was a bit higher than the H=0.5D case, suggesting that H=0.3D is a solution for where the dune is downstream. The Coanda effect, which affects the cooling performance behind Barchan dunes, is determined by the thickness of the "gap". The gap needs to be a specific size in order to generate proper attraction to push the coolant downward. The PSP results indicate that the gap of the H=0.3D case was just enough in the present study.

Based on above discussion (Fig. 10 & Fig. 11), it is apparent that the BDA film cooling is not only closely related to the height but also intrinsically related to the location of dune. With dune upstream, the H=0.5D case is a better solution for when the dune is placed upstream, while the H=0.3D is a considerable solution for the downstream configurations.

3.7 Area-averaged film effectiveness.

Figure 12 shows the area-averaged film cooling effectiveness and standard deviation of above three different configurations (from x/D=1 to 15; z/D=-1.5D to 1.5D) as a

function of mass flux ratio. The area-averaged effectiveness is computed by $\frac{1}{A}\iint \eta_{xz} dA$, where A is the total interest area, and η_{xz} is the corresponding effectiveness at each location. A lower standard deviation value represents a more uniform film coverage over the area of interest. As shown in Figure 12, the BDA film cooling with H=0.5D and L=-0.9D was found to display the highest averaged effectiveness and lowest standard deviation for most of the cases. Comparing with baseline, there was an augmentation of 50%-100% in Area-averaged effectiveness for WBD (H=0.5D, L=0.9D) case at M>0.85, indicating that the proposed configuration can provide a more uniform film over the test plate to protect the surface.

4. Conclusion

An experimental study was conducted to investigate the film cooling performance of proposed Barchan-dune-shaped ramp located either upstream or downstream of circular holes. While Pressure Sensitive Paint (PSP) technique was used to map the corresponding adiabatic film cooling effectiveness on the surface of interest, a high-resolution PIV system was used to conduct detailed flow field measurements to quantify the turbulent mixing between coolant and mainstream flow behind the Barchan-dune-shaped ramps. The effects of mass flux ratio (M=0.40, 0.85, 1.00, 1.25), dune location (DB=-3.0D, -0.9D, 2.7D, 3.4D), and height (H=0.3D, 0.5D) of Barchan dunes on the film cooling effectiveness were examined in great detail based on quantitative PSP and PIV measurements.

The experimental results revealed that BDA film cooling of H=0.5D and L=-0.9D can largely enhance the cooling performance of circular hole at relatively high mass flux ratios. Compared with circular hole, there was a 50%-100% gain in Area-averaged effectiveness for WBD (H=0.5D, L=0.9D) case at M>0.85. Investigation of flow physics using PIV and stereo-PIV showed three distinct mechanisms for enhancement of film cooling performance (i) down-wash stream from the crest of dune lowered and diffused the coolant jet in stream-wise direction, (ii) vortex structure in X-Z plane generated continuous suction along the horn of dunes, resulting in wider lateral film coverage, and (iii) formation of Anti-CRV pair in Y-Z plane counteracted the vortex induction from coolant jet, causing downdraught of coolant from jet core.

Also, the effectiveness of film cooling of WBD was found to be closely related to both the location and height of the dune. With dune upstream, the H=0.5D case is a better solution for when the dune is placed upstream at M>0.85. This is caused by the stronger downwash and suction effects in the taller case. However, the H=0.3D is a considerable solution for the downstream configurations due to the Coanda effect. Although the proposed Barchan-Dune ramp manifested improved cooling behavior than circular hole, extensive investigations are still needed to study the heat transfer coefficient, aerodynamic loss, and structural strength for further understanding the overall performance of BAD film cooling in severe environments encountered by gas turbine engine.

References

[1] Bogard, D. G., and Thole, K. A., 2006, "Gas Turbine Film Cooling," J. Propuls. Power, **22**(2), pp. 249–270.

[2] Bogard, D. G., 2006, "Airfoil film cooling," The Gas Turbine Handbook, National Energy Technology Laboratory, Section 4.2.2.1.

[3] Baldauf, S., Schulz, A., and Wittig, S., 2001, "High-Resolution Measurements of Local Effectiveness From Discrete Hole Film Cooling," J. Turbomach., **123**(4), p. 758.

[4] Baldauf, S., Scheurlen, M., Schulz, A., and Wittig, S., 2002, "Correlation of Film-Cooling Effectiveness From Thermographic Measurements at Enginelike Conditions," J. Turbomach., **124**(4), p. 686.

[5] Wright, L. M., McClain, S. T., and Clemenson, M. D., 2011, "Effect of Freestream Turbulence Intensity on Film Cooling Jet Structure and Surface Effectiveness Using PIV and PSP," J. Turbomach., **133**(4), p. 041023.

[6] Goldstein, R. J., Eckert, E. R. G., and Burggraf, F., 1974, "Effects of hole geometry and density on three-dimensional film cooling," Int. J. Heat Mass Transf., **17**(5), pp. 595–607.

[7] Schmidt, D. L., Sen, B., and Bogard, D. G., 1996, "Film Cooling With Compound Angle Holes: Adiabatic Effectiveness," J. Turbomach., **118**(4), p. 807.

[8] Lu, Y., Faucheaux, D., and Ekkad, S. V., 2005, "Film Cooling Measurements for Novel Hole Configurations," ASME 2005 Summer Heat Transfer Conference collocated with the ASME 2005 Pacific Rim Technical Conference and Exhibition on Integration and Packaging of MEMS, NEMS, and Electronic Systems, ASME, pp. 59–66.

[9] Sargison, J. E., 2001, "Development of a Novel Film Cooling Hole Geometry," PhD Dissertation, Dept. of Engineering Sci., University of Oxford.

[10] Dhungel, A., Lu, Y., Phillips, W., Ekkad, S. V., and Heidmann, J., 2009, "Film Cooling From a Row of Holes Supplemented With Antivortex Holes," J. Turbomach., **131**(2), p. 021007.

[11] Bunker, R. S., 2005, "A Review of Shaped Hole Turbine Film-Cooling Technology," J. Heat Transfer, **127**(4), p. 441.

[12] Zaman, K. M., Rigby, D., and Heidmann, J., 2010, "Inclined Jet in Crossflow Interacting With a Vortex Generator," J. Propuls. Power, **26**(5), pp. 947–954.

[13] Shinn, A. F., and Pratap Vanka, S., 2013, "Large eddy simulations of film-cooling flows with a micro-ramp vortex generator," J. Turbomach., **135**(1), p. 011004.

[14] An, B., Liu, J., Zhang, C., and Zhou, S., 2013, "Film Cooling of Cylindrical Hole With a Downstream Short Crescent-Shaped Block," J. Heat Transfer, **135**(3), p. 031702.

[15] Na, S., and Shih, T., 2007, "Increasing adiabatic film-cooling effectiveness by using an upstream ramp," J. Heat Transfer, **129**(4), pp. 464–471.

[16] Sakai, E., Takahashi, T., and Agata, Y., 2013, "Experimental Study on Effects of Internal Ribs and Rear Bumps on Film Cooling Effectiveness," J. Turbomach., **135**(3), p. 031025.

[17] Andreotti, B., Claudin, P., and Douady, S., 2002, "Selection of dune shapes and velocities Part 1: Dynamics of sand, wind and barchans," Eur. Phys. J. B - Condens. Matter, **28**(3), pp. 321–339.

[18] Parteli, E., Durán, O., and Herrmann, H., 2007, "Minimal size of a barchan dune," Phys. Rev. E, **75**(1), p. 011301.

[19] Christensen, K. T., Kazemifar, F., Blois, G., Barros, J. M., Tang, Z., Hamed, A., Kim, T., and Best, J. L., 2014, "Quantitative Studies of Environmental Flows at the Micro- and Macro-Scales," 16th International Symposium on Flow Visualization, Okinawa, Japan.

[20] Palmer, J. A., Mejia-Alvarez, R., Best, J. L., and Christensen, K. T., 2011, "Particle-image velocimetry measurements of flow over interacting barchan dunes," Exp. Fluids, **52**(3), pp. 809–829.

[21] Horvat, B., "Barchan dunes Seminar 2," p. http://www–f1.ijs.si/~rudi/sola/Sem4.pdf.

[22] Hersen, P., Andersen, K., Elbelrhiti, H., Andreotti, B., Claudin, P., and Douady, S., 2004, "Corridors of barchan dunes: Stability and size selection," Phys. Rev. E, **69**(1), p. 011304.

[23] Ou, S., Han, J.-C., Mehendale, A. B., and Lee, C. P., 1994, "Unsteady Wake Over a Linear Turbine Blade Cascade With Air and CO2 Film Injection: Part I—Effect on Heat Transfer Coefficients," J. Turbomach., **116**(4), p. 721.

[24] Han, J., Dutta, S., and Ekkad, S., 2012, Gas turbine heat transfer and cooling technology, Taylor and Francis, New York.

[25] Wright, L. M., Gao, Z., Varvel, T. A., and Han, J.-C., 2005, "Assessment of Steady State PSP, TSP, and IR Measurement Techniques for Flat Plate Film Cooling," Heat Transfer: Volume 3, ASME, pp. 37–46.

[26] Bell, J. H., Schairer, E. T., Hand, L. A., and Mehta, R. D., 2001, "SURFACE PRESSURE MEASUREMENTS USING LUMINESCENT COATINGS 1," Annu. Rev. Fluid Mech., **33**(1), pp. 155–206.

[27] Eckert, E. R. G., 1992, "Similarity analysis of model experiments for film cooling in gas turbines," Wärme- und Stoffübertragung, **27**(4), pp. 217–223.

[28] Shadid, J. N., and Eckert, E. R. G., 1991, "The Mass Transfer Analogy to Heat Transfer in Fluids With Temperature-Dependent Properties," J. Turbomach., **113**(1), p. 27.

[29] Charbonnier, D., Ott, P., Jonsson, M., Cottier, F., and Köbke, T., 2009, "Experimental and Numerical Study of the Thermal Performance of a Film Cooled Turbine Platform," Proc. Asme Turbo Expo 2009, Vol 3, Pts A B, pp. 1027–1038.

[30] Yang, Z., and Hu, H., 2011, "Study of Trailing-Edge Cooling Using Pressure Sensitive Paint Technique," J. Propuls. Power, **27**(3), pp. 700–709.

[31] Johnson, B., Tian, W., Zhang, K., and Hu, H., 2014, "An experimental study of density ratio effects on the film cooling injection from discrete holes by using PIV and PSP techniques," Int. J. Heat Mass Transf., **76**, pp. 337–349.

[32] Sajben, M., 1993, "Uncertainty estimates for pressure sensitive paint measurements," AIAA J., **31**(11), pp. 2105–2110.

[33] Kline, S. J., and Mcclintock, F. A., 1953, "Describing uncertainties in single sample experiments," J. Mech. Eng., **75**.

[34] Coleman, H. W., and Steele, W. G., 2009, Experimentation, Validation, and Uncertainty Analysis for Engineers, John Wiley & Sons.

[35] Johnson, B. E., and Hu, H., 2014, "Measurement Uncertainties Analysis in the Determination of Adiabatic Film Cooling Effectiveness by Using Pressure Sensitive Paint (PSP) Technique," Volume 1D, Symposia: Transport Phenomena in Mixing; Turbulent Flows; Urban Fluid Mechanics; Fluid Dynamic Behavior of Complex Particles, ASME, p. V01DT40A001.

[36] Sinha, A. K., Bogard, D. G., and Crawford, M. E., 1991, "Film-Cooling Effectiveness Downstream of a Single Row of Holes With Variable Density Ratio," J. Turbomach., **113**(3), p. 442.

[37] Pedersen, D., 1977, "Film cooling with large density differences between the mainstream and the secondary fluid measured by the heat-mass transfer analogy," J. Heat Transfer, **99**(4), pp. 620–627.

[38] Fric, T. F., and Roshko, A., 1994, "Vortical structure in the wake of a transverse jet," J. Fluid Mech., **279**, pp. 1–47.

[39] Zheng, Y., and Rinoshika, A., 2015, "Multi-scale vortical structure analysis on large eddy simulation of dune wake flow," J. Vis., **18**(1), pp. 95–109.

[40] Omidyeganeh, M., Piomelli, U., Christensen, K. T., and Best, J. L., 2013, "Large-eddy simulation of flow over barchan dunes," Marine and River Dune Dynamics – MARID IV, Bruges, pp. 191–198.

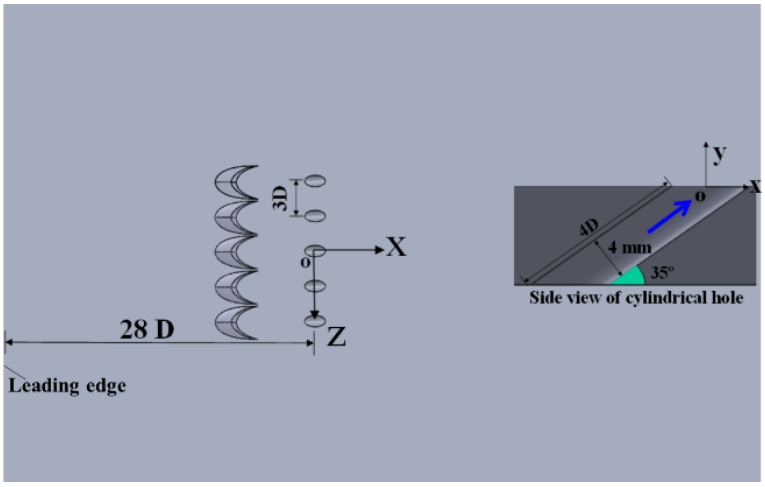

(a) Barchan dune-assisted film cooling configuration

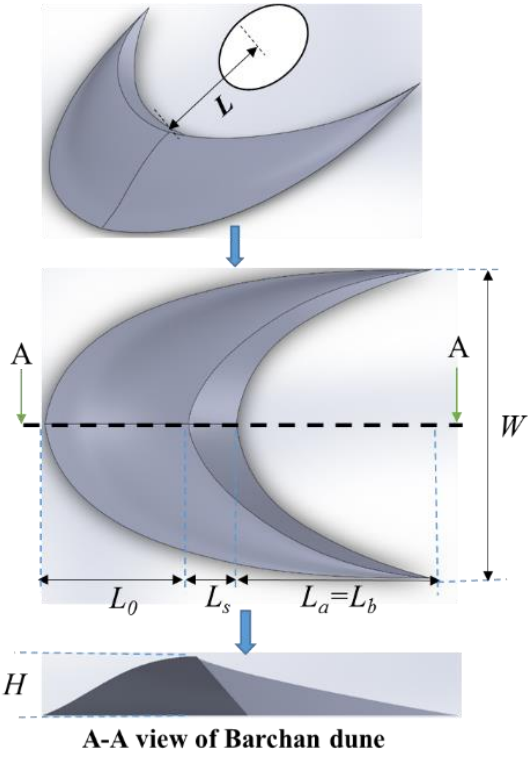

$Case1:$
$H = 0.3D$
$W = 2.85D$
$L_a = L_b = 1.8D$
$L_0 = 1.35D$
$L_s = 0.45D$

$Case2:$
$H = 0.5D$
$W = 2.85D,$
$L_a = L_b = 1.8D$
$L_0 = 1.35D$
$L_s = 0.45D$

(b) Detailed dimensions of Barchan dune

Figure 1. *Test models used in the present study (D is the diameter of coolant hole).*

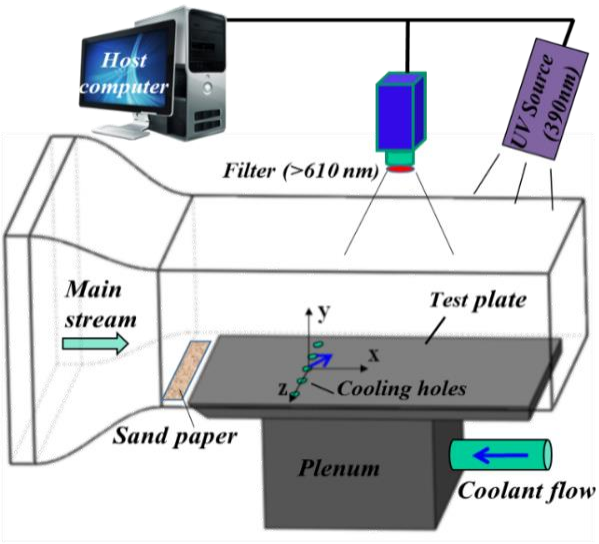

Figure 2. *Experimental setup for PSP measurements.*

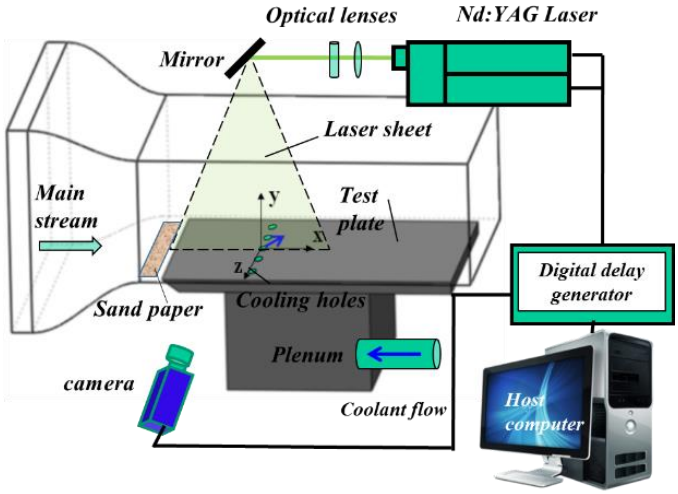

Figure 3. *Experimental test rig for PIV measurements.*

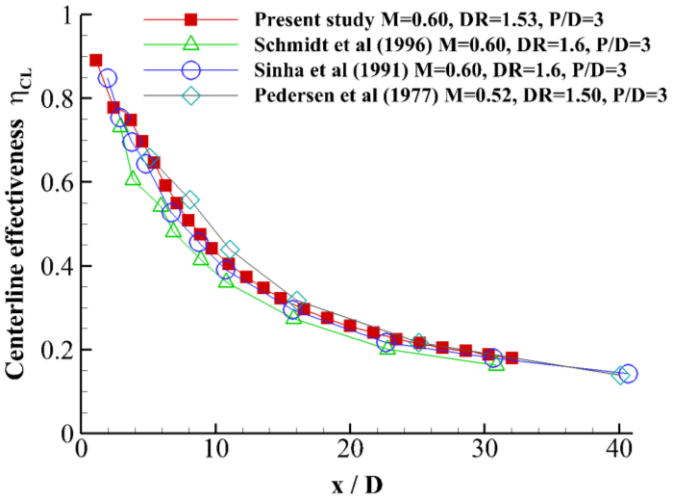

(a) Centerline effectiveness of cylindrical hole

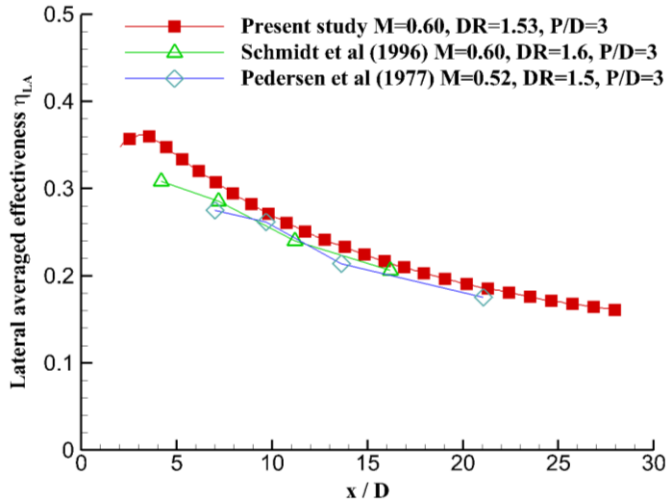

(b) Laterally-averaged effectiveness of cylindrical hole

Figure 4. *Comparison of measured film cooling effectiveness of present study with published results of previous studies at M=0.60, DR=1.53.*

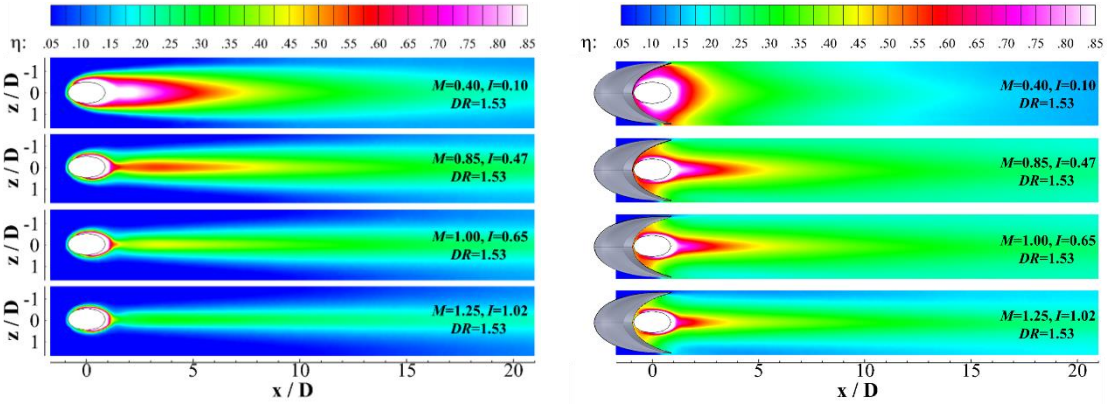

(a) The spatial distribution of film cooling effectiveness

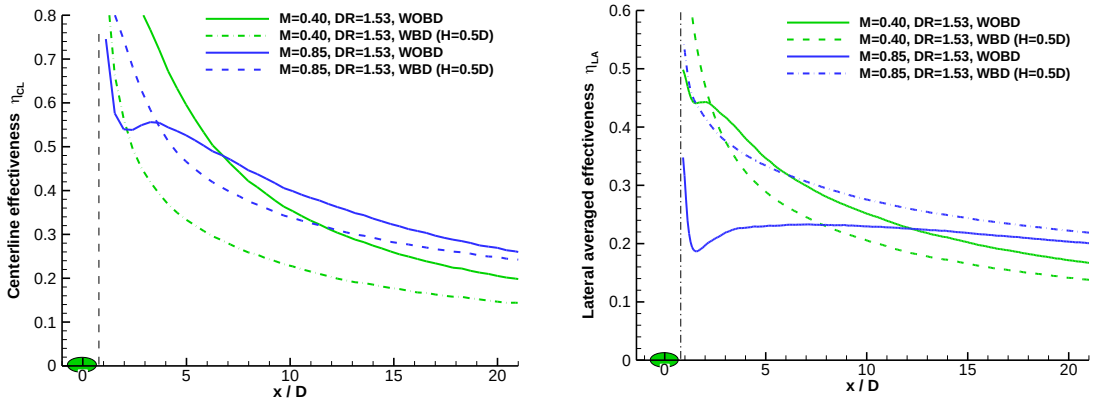

(b) The measurement results at M=0.40, 0.85

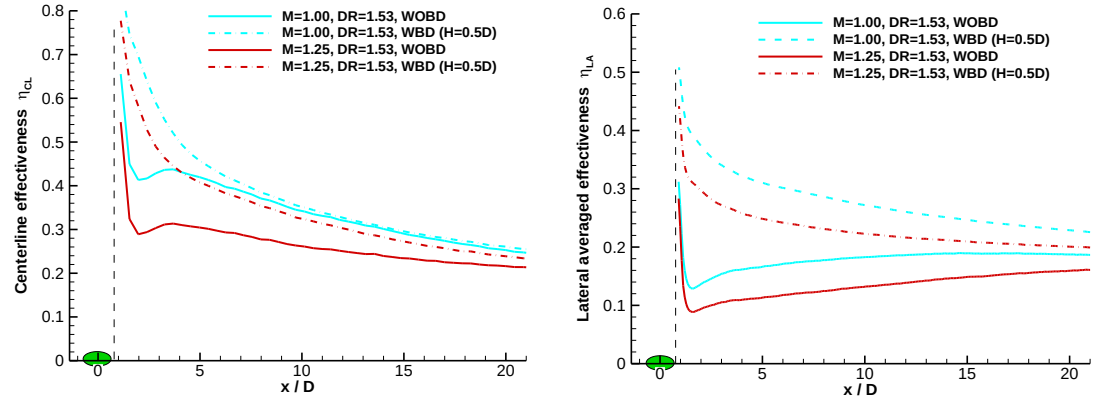

(c) The measurement results at M=1.00, 1.25

Figure 5. *Comparison of film cooling effectiveness between WOBD and WBD configurations at various mass flux ratio.*

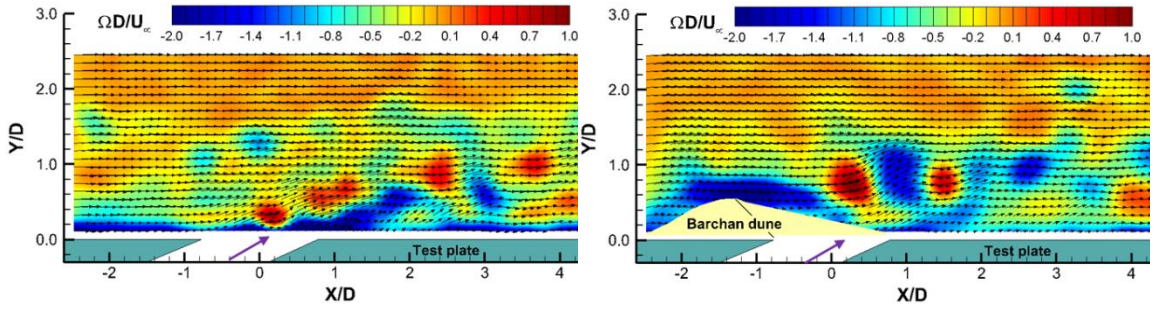

(a) Instantaneous vorticity field at *M*=1.0

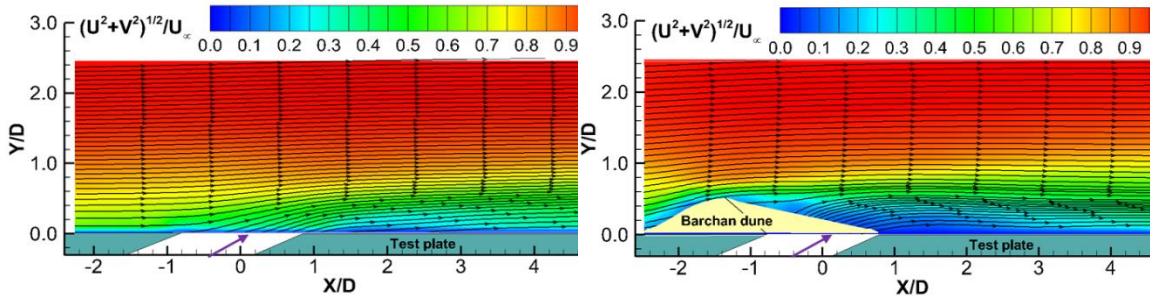

(b) Ensemble-averaged velocity field at *M*=0.40

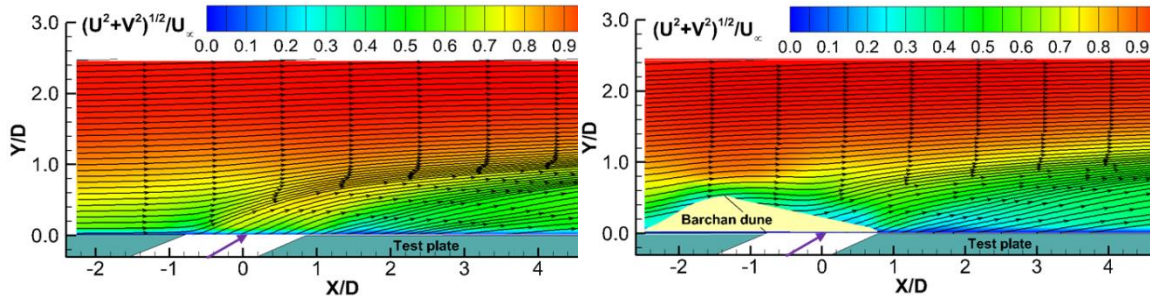

(c) Ensemble-averaged velocity field at *M*=1.00

Figure 6. *Measured PIV results for WOBD (left) and WBD (right) assisted cooling at M=0.40 and M=1.00 respectively.*

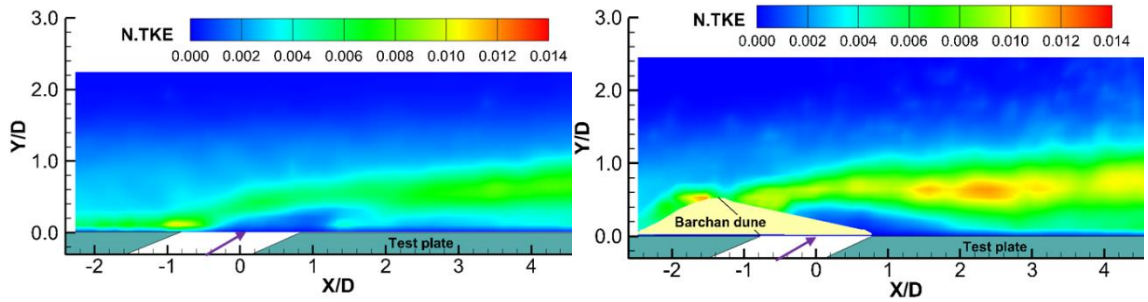

(b) Normalized TKE distribution at M=0.40

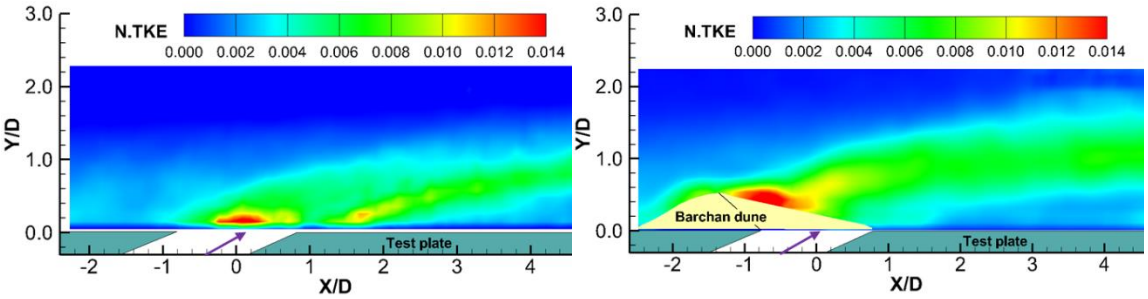

(c) Normalized TKE distribution at M=1.00

Figure 6 continued. *Measured PIV results for WOBD (left) and WBD (right) assisted cooling at M=0.40 and M=1.00 respectively.*

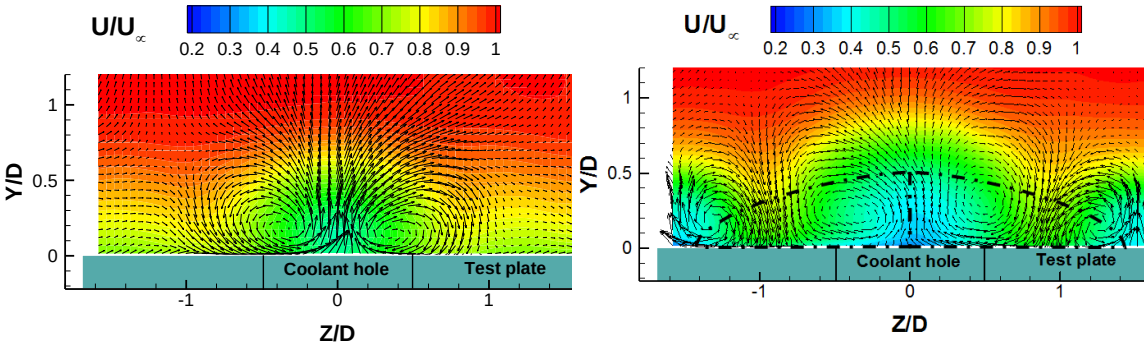

(a) Normalized streamwise velocity in the *X/D*=3.0 cross plane at *M*=1.00.

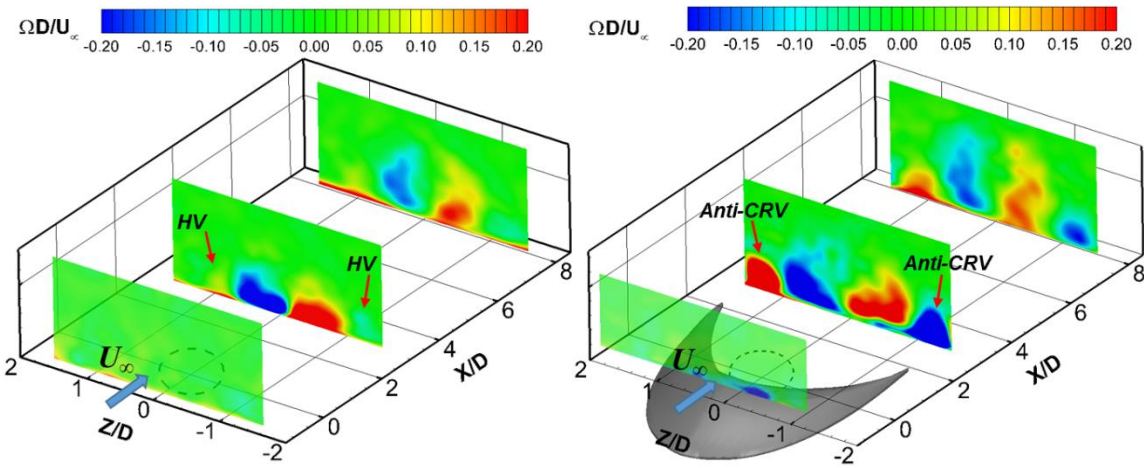

(b) Normalized vorticity evolution along stream-wise direction at *M*=1.00, where *HV* means horseshoe vortex.

Figure 7. *Stereoscopic PIV results for WOBD (left) and WBD (right) assisted film cooling at M=1.00.*

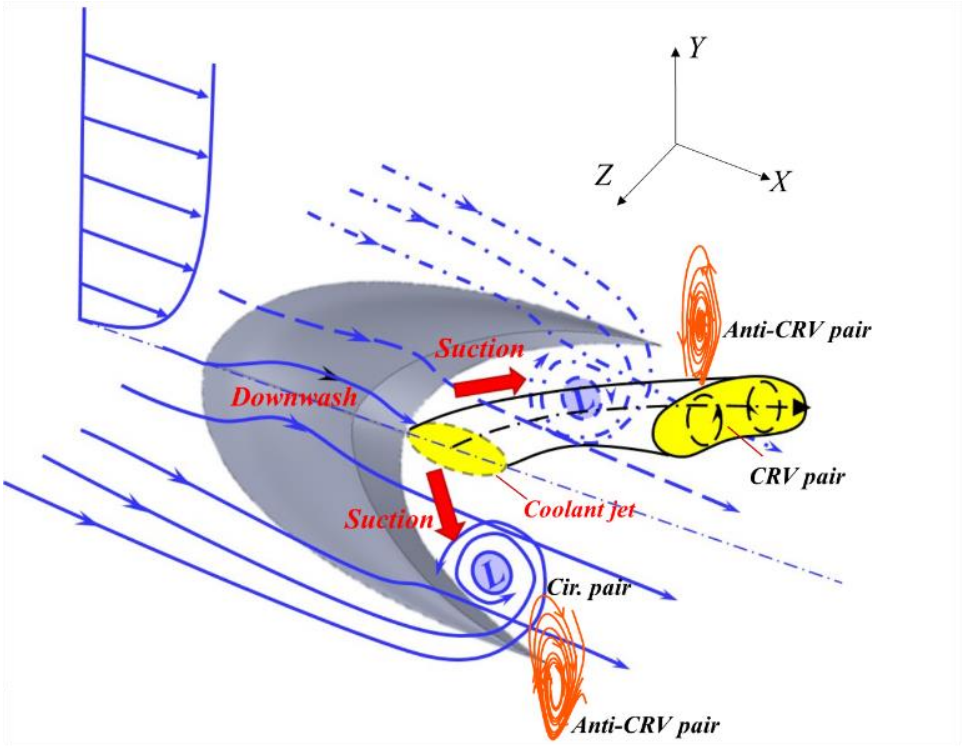

Figure 8. *Schematic of the flow structures behind BDA film cooling configuration, L indicates low pressure region.*

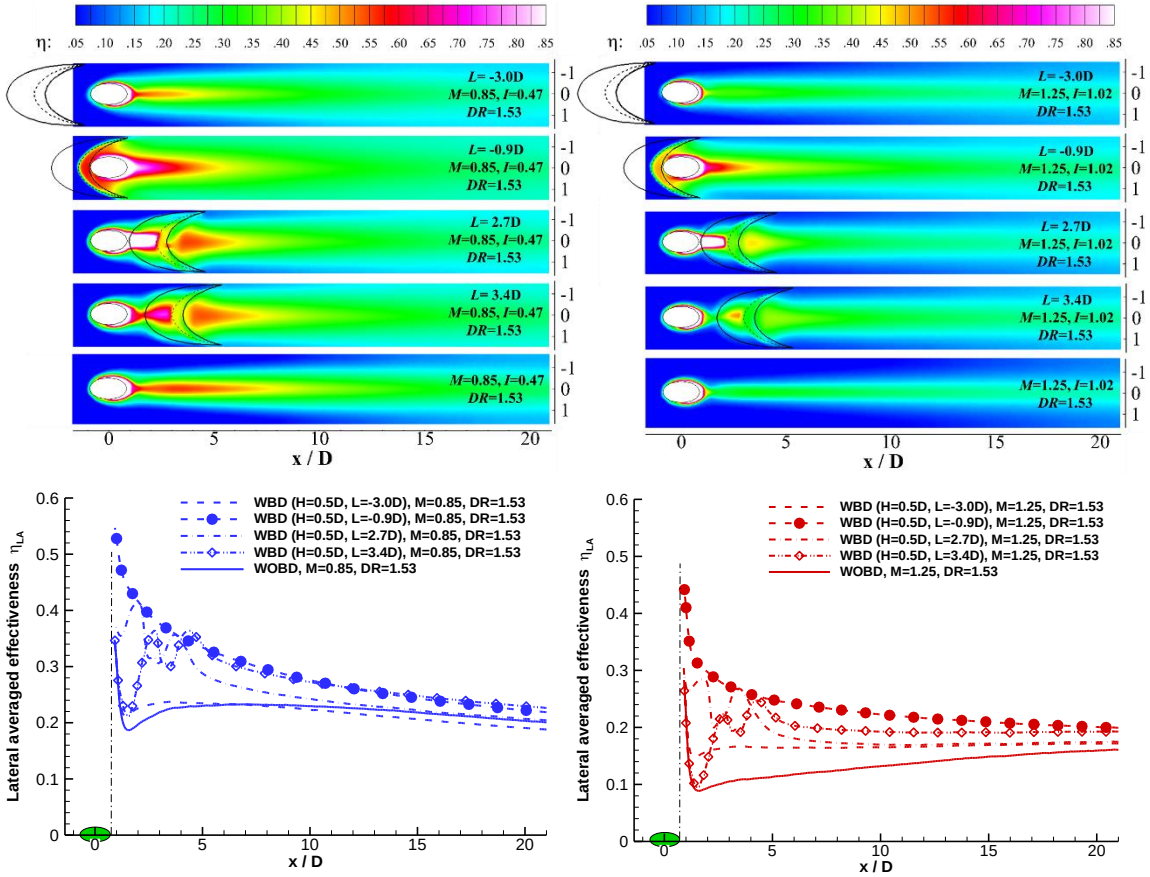

(a) Film cooling effectiveness at M=0.85

(b) Film cooling effectiveness at M=1.25

Figure 9. *Film cooling effectiveness as function of distance between Barchan dune and coolant hole at M=0.85 (left) and 1.25 (right).*

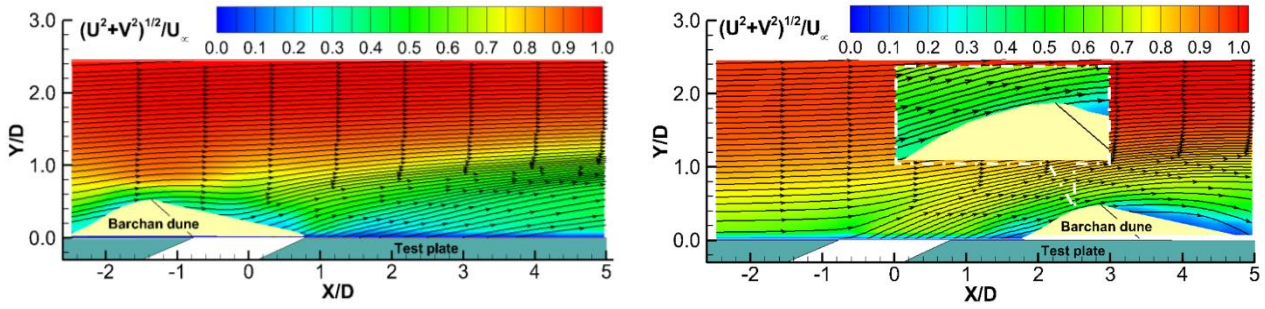

(a) Mean velocity distribution at *M*=1.00

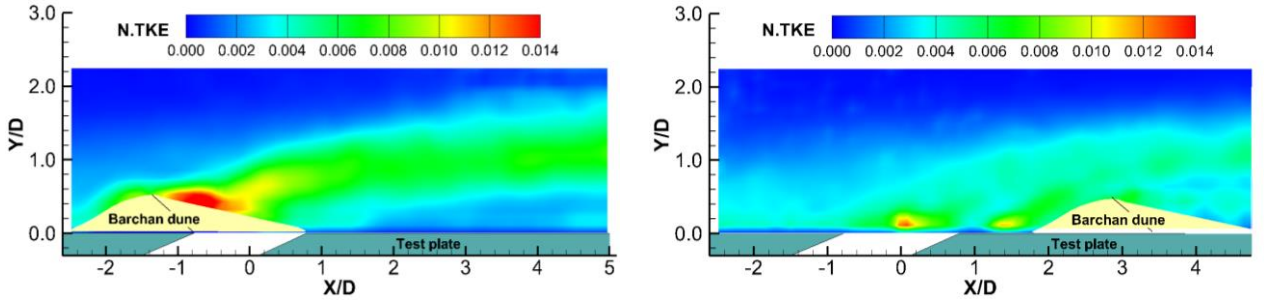

(b) Normalized TKE distribution at *M*=1.00

Figure 10. *PIV measurement results with Barchan dune upstream (left, L=-0.9D) and downstream (right, L=3.4D) of coolant hole at M=1.0.*

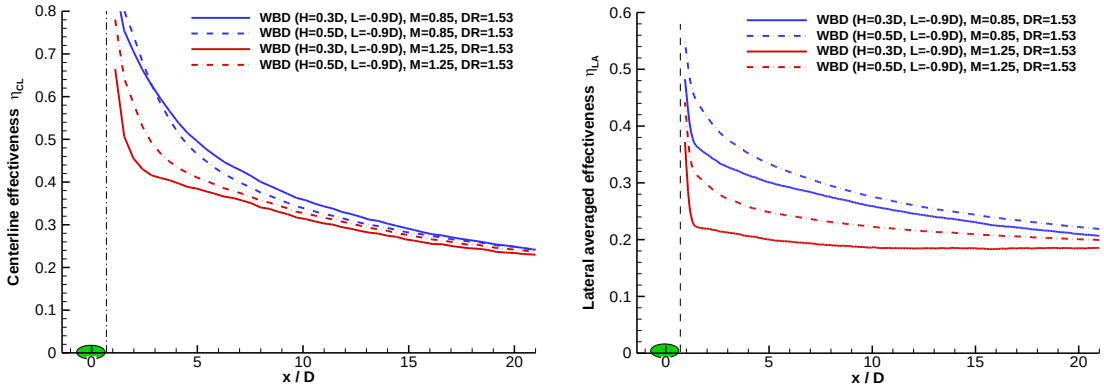

(a) Film cooling effectiveness with Barchan dune upstream (L=-0.9D)

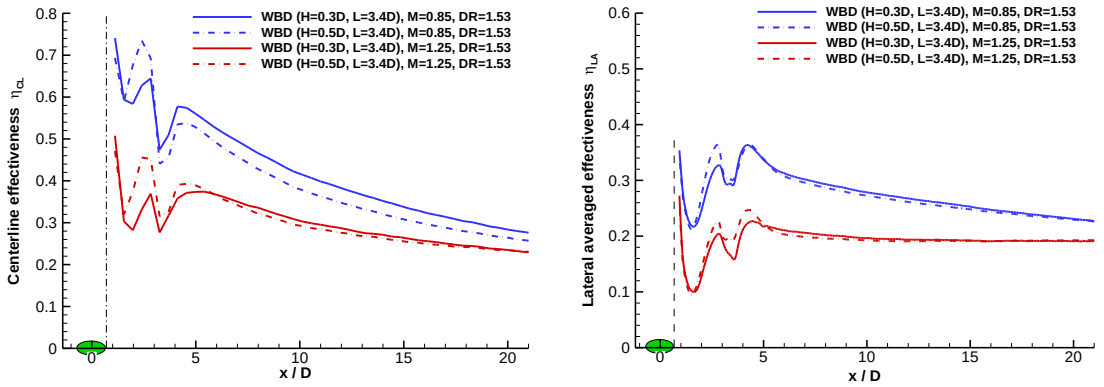

(b) Film cooling effectiveness with Barchan dune downstream (L=3.4D)

Figure 11. *Height effects of Barchan dune on film cooling effectiveness with dune upstream (L= -0.9D) and downstream (L=3.4D).*

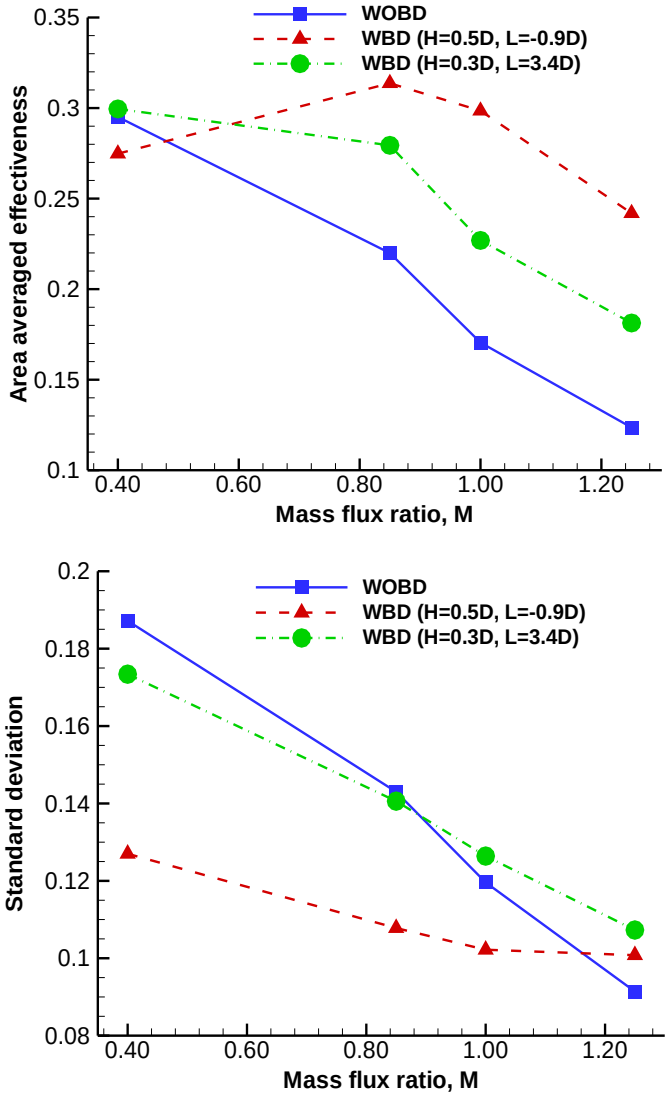

Figure 12. *The area-averaged cooling effectiveness and standard deviation as a function of mass flux ratio.*

CHAPTER 3

AN EXPERIMENTAL STUDY OF BARCHAN-DUNE-SHAPED INJECTION COMPOUNDS FOR IMPROVED FILM COOLING EFFECTIVENESS

Wenwu Zhou and Hui Hu

Department of Aerospace Engineering, Iowa State University, Ames, IA 50011, USA

ABSTRACT

Inspired by the unique shape of Barchan dune, which prevents sand particles on the ground from being blown away by the oncoming airstream, we proposed a Barchan-dune-shaped injection compound (BDSIC) for film cooling. Similar as the sand particles settling down on the ground behind the dune, the coolant streams exhausted from BDSIC would be able to flow over the surface of interest more steadily. The performance of film cooling behind BDSIC had been studied experimentally for a single 35 degree angled hole on a flat plate using PSP and PIV techniques. The effects of the dune shape, mass flux ratio, density ratio, and hole interaction on the film cooling effectiveness were studied in great detail. It was found that the BDSIC configurations can greatly enhance the cooling performance of baseline for all test conditions, especially the BDSIC with the elongated dune. Investigation of flow physics showed that the complete elimination of a CRV pair prevented the jet from lifting off, and formation of Anti-CRV created downdraught of coolant from the jet core, therefore the effectiveness was significantly improved. Comparing this to a circular hole, the aerodynamic loss of BDSIC was reduced at relative high mass flux ratio. In general, the BDSIC configuration possesses the merits from both

Barchan dune and ideal tangential slot, which demonstrated an enhanced effectiveness with less aerodynamic loss.

1. Introduction

To continue improving the thermal efficiency and power output of modern gas turbines, it is necessary to further enhance the turbine inlet temperatures while reducing the amount of cooling gas. Therefore, means to protect the blades from corrosion and melting are indispensable for a sustainable operation, especially the implementation of film cooling technique. The idea of film cooling is to build a thin film on the blade surface by injecting coolant into cross-flow to prevent it from direct hot gas exposure, hence increasing their working hours. A practical issue is to reduce the coolant flow rate while providing the necessary cooling, which requires substantial investigations to understand the inherent physics of film cooling and optimize its configurations. Many new holes and concepts of film cooling have been proposed recently to address this issue.

Film cooling studies of using slots, typically not practical in a gas turbine, were summarized clearly by Goldstein [1]. Utilization of discrete holes for film cooling is a more realistic option in a real gas turbine. There is a large number of experiments focused on the discrete holes, especially the basic film-cooling geometry: a row of circular holes on a flat plate [2–10]. This geometry allows for the study of jet lift-off and counter rotating vortex (CRV) pairs and is probably the most widely used configuration for turbine film cooling. Besides the circular holes, the exploration of shaped holes are one of the long lasting research topics in film cooling. Bunker [11] provided a decent literature overview of published film-cooling shaped holes. Goldstein *et al.* [12] firstly reported a remarkable

increment of film cooling performance by using fan-shaped holes, where the hole was similar to a diffuser that the momentum of the jet was reduced at the breakout of test plate. Similar results were obtained by Schmidt *et al.* [8], who studied a compound angle shaped hole. Besides the typical shaped hole with either lateral or laidback expansion, various new holes have been proposed over the years to improve the cooling performance. Heidmann *et al.* [13] and Dhungel *et al*. [14] introduced an anti-vortex hole concept that aimed to reduce the strength of CRV pair. Their measurements showed augmented film cooling effectiveness at certain hole orientation. Sargison *et al.* [15] demonstrated an enhanced cooling performance and lower aerodynamic loss for console-shaped hole. Other ideas such as trenched holes (Bunker [16]), crescent-shaped hole (Lu *et al*. [17]), and yaw angle double-row holes (Gräf and Kleiser [18]) were proposed and studied, which showed effective test results. Shaped holes provide a promising solution for film cooling, except the concerns of structure strength reduction and spatial restrictions hinder its applications in certain situations.

The appearance of 3D-printing technology has greatly promoted the development of film cooling design concept. Many innovative but unmachinable design concepts can now be printed as a whole part at the engine scale, including the shaped hole and other new cooling concepts such as placing a ramp upstream or downstream of coolant hole. Zaman and Foss [19] studied the effect of triangular tabs on the jet in cross flow, and found that the strength of bound vortex pair was diminished and the jet penetration was reduced. Similar conclusion was drawn by Zaman *et al*. [20] and Shinn *et al*. [21] using micro-ramp vortex generators. Na and Shih [22] performed a numerical study on placing ramp upstream of the coolant hole. Their results indicated that the ramp with backward step can

enhance the film cooling effectiveness. Sakai *et al*. [23] studied the combined effects of internal ribs and bumps on the film cooling effectiveness, and found that the cooling performance is strongly affected by the rib orientations and bump shapes. Zhou and Hu [24] proposed Barchan-dune-assisted film cooling concept and demonstrated 50-100% improvement of area-averaged cooling effectiveness. Most of the presented designs are shown to be effective in improving the performance, however the majority of these ideas produce an unwanted sharp edge that contains aerodynamic liabilities or additional surfaces that are difficult to cool.

Barchan dunes are commonly-seen features on Earth. They have streamlined shape along the wind flow direction, featured by a crescentic platform with two gradually-widened horns pointing downstream [25,26]. When airflow passes over it, symmetric vortex structures would be formed behind the dune. Due to its unique shape, the continual suction induced by the vortices generates a "quiet" wake flow behind the dune. As a result, sand particles can settle down on the ground behind the dune, instead of being blown away by the incoming flow. Inspired by the unique shape of Barchan dune to prevent sand particles on the ground from being blown away by the oncoming airstream, we proposed a Barchan-dune-shaped injection compound (BDSIC) for film cooling, upgraded from our previous film cooling concept [24]. Similar as the sand particles settling down on the ground behind the dune, the coolant streams exhausted from BDSIC will be able to flow over the surface of interest more steadily to provide a better film cooling protection to the surface. Furthermore, the shape of Barchan dune is also found to be able to minimize the friction loss of the airstream flowing over the dune.

Therefore, an experimental study was conducted to evaluate the effectiveness of film cooling of the BDSIC with different dune geometries, in comparison with using conventional circular hole as the baseline. In the present study, a high-resolution Particle Image Velocimetry (PIV) system was used to conduct detailed flow field measurements to understand the dynamic mixing process between the coolant stream and the mainstream flows behind the BDSIC. The Pressure Sensitive Paint (PSP) technique was used to map the corresponding adiabatic film cooling effectiveness on the surface of interest based on a mass-flux analog to traditional temperature-based cooling effectiveness measurements. The effects of geometrical parameters, mass flux ratio, density ratio, and hole interaction of the BDSIC on the film cooling effectiveness were examined in great detail based on the quantitatively PIV and PSP measurements. The detailed PIV flow field measurements were correlated with the adiabatic cooling effectiveness maps to reveal inherent physics in order to optimize/explore design paradigms for improved film cooling effectiveness in order to protect the crucial components of turbine blades from harsh environments.

2. Experimental Setup and Test Model

2.1 Experimental model and test rig.

The experimental studies were conducted in a low-speed, open-circuit wind tunnel located at the Department of Aerospace Engineering of Iowa State University. The tunnel has an optically-transparent test section with a cross section of 200 mm×125 mm and is driven by an upstream blower. With honeycombs and screen structures installed ahead of the contraction section, the tunnel can supply uniform low-turbulence oncoming flow into

the test section. The mainstream turbulence intensity of airflow in the test section was found to be about 1.5%, as measured by a hotwire anemometer.

In present study, all test models including test plate and dunes were made of hard ABS-like plastic material and manufactured by a rapid prototyping 3D-printer that built the models layer-by-layer with a resolution of about 25 microns. Figure 1 (a) shows the Barchan-dune-shaped injection compound (BDSIC) film cooling configuration, where the dune was affixed on the surface of the test plate by using a layer of 80 μm-thick double sided tape. For the circular hole case, everything remained the same except for the removal of the dune and cleaning of tape adhesive residue. The coolant stream was injected through a single cylindrical holes with diameter D=12mm at an injection angle 35° relative to the upper surface of the flat test plate. The entry length of the coolant hole is 2.5D. The inlet and outlet of the hole was sharp edged, and the interior was smoothed using sand paper. The test plate was mounted on a plenum chamber (115 mm ×115 mm ×90 mm) and sealed by a thin latex rubber gasket. The pressure inside plenum was monitored by four pressure taps installed on each face.

Figure 1 (b) shows the detailed dimensions of the hollowed Barchan dunes used in the present study. There are three types of dunes including the shorted dune, normal dune, and elongated dune. The height of the dune is H=0.6D, and the wall thickness of the model is 0.1D at the peak location. The normal dune herein is the standard for other two models, which was generated from a stereoscopic topographic map of idealized Barchan dune [25,27–29]. The curvature of the model shape truthfully reflects the curvature of dune encountered in deserts. Also the dimensions of the normal dune fall within the range of the published data found in natural environments. The shorted dune was obtained by

reducing the horn length of the normal dune to 1.3*D*, while the other dimensions remained the same. Similar for the elongated dune, only the front part of the normal dune was extended from 1.35*D* to 2*D*. This was to ensure fully cover of injection from circular hole. The hollowed dunes were generated by cutting off an extra Barchan-dune-shaped part from the base of the original models, in order to form a dune-shaped injection to further lower the aerodynamic loss. Also the morphology of hollowed parts were carefully manipulated to maintain the same exit area as the circular hole. The exit of the dune can be approximately viewed as a semi-ellipse with 2*D* major axis and 1*D* minor axis. All these models were built by the lofting command through Solidworks along a series of parabolic guidelines (obtained from scaled-down dune), which has a smooth surfaces in the windward side (convex face). It is worth noted that the coolant stream in BDSIC is designed to tangentially inject into the mainstream flow in order to minimize the turbulent mixing within shear layers. And the front part of BDSIC can be cooled intensively by the impingement cooling, while film cooling can be used for the rear part.

Figure 2 shows the schematic of the PSP experimental setup used in the present study. A constant UV light (LM2X-DM, ISSI) with a wavelength of 390 nm was used as the excitation source for the PSP measurements. A 14-bit (2048 pixel × 2048 pixel) charge-coupled device (CCD) camera (PCO2000, Cooke Corp.) fitted with a 610 nm long-pass filter was used to record the intensity of the photoluminescence light emitted by excited PSP molecules. The PSP paint used in the study was Uni-FIB provided by ISSI. This type of paint has a low sensitivity to temperature variation (~0.5%/°C) making it an ideal candidate for the study. The tests were conducted in a place (~22°C) where the temperature fluctuation was kept to a minimum. During the experiment, the mainstream flow from the

wind tunnel was used to simulate the hot gas flow in a typical turbine stage. The test section had a constant speed of $U_\infty = 25$ m/s in the study. The coolant jet flow, supplied by the pressurized gas cylinder (99.99% purity), passed through control valves to enter the plenum chamber. In the present study, the N_2, CO_2, and mixture of SF_6 and CO_2 were chosen to study the density ratio effects on film cooling effectiveness in order to simulate the temperature differences between hot gas and coolant stream in real engine. The corresponding density ratios ($DR = \rho_c / \rho_\infty$) were 0.97, 1.53 and 2.1 respectively. A two-in.-wide 32 grit sand paper was employed at the leading edge of test section (i.e., 12D distance upstream of coolant hole) to trip the oncoming boundary layer to ensure a fully developed boundary layer flow over the flat plate. The boundary layer profile was measured immediately upstream of the coolant holes (with no coolant flow). It was determined to resemble a fully-developed turbulent boundary layer with thickness of $\delta_{99} \approx 0.72D$, momentum thickness $\theta \approx 0.08D$ (corresponding $Re_\theta \approx 1.5$K), and shape factor 1.33. The experiment was performed at mass flux ratios ($M = \rho_c V_c / \rho_\infty V_\infty$) ranging from 0.3 to 1.5.

2.2 Adiabatic film cooling effectiveness measurement using the PSP technique.

Adiabatic film cooling effectiveness η is traditionally expressed as,

$$\eta = \frac{T_\infty - T_{aw}}{T_\infty - T_c} \quad , \tag{1}$$

where T_∞ is the temperature of the main-stream, T_{aw} is the adiabatic wall temperature of the surface under inspection, and T_c is the hole exit temperature of the coolant stream.

In the present study, the film cooling effectiveness was measured by using a pressure sensitive paint (PSP) technique [30] rather than conducting temperature-based measurements on the surface of interest (such as using thermocouples, liquid crystal thermometry, infrared thermography, or temperature sensitive paint). The PSP technique is based on mass transfer analogy, which is free from heat conduction related errors encountered in non-isothermal experiments. When the value of the *Lewis number* ($Le = \alpha/D_s$) is about 1, the thermal boundary layer and concentration boundary layer thickness are of the same order. Therefore, the differential equations regarding heat and mass transfer can be treated as analogous [31,32], which is the case for present study ($Le \approx 1$).

In order to perform the PSP experiments, the surface of interest was coated with an oxygen-sensitive layer of paint. This paint consists of luminophores molecules held together through gas-permeable polymeric binder. When excited by certain UV light, the luminophores molecules in PSP paint will emit light. However, the excited molecules may return to ground state via a reduced or radiationless emission in the presence of oxygen molecules. This process is called oxygen quenching [30], where the intensity of the photoluminescence is inversely proportional to the concentration of local oxygen. Consequently, the concentration of oxygen against the interested surface can be calculated by recorded light intensity through the use of a calibrated curve. Applying the concentrations of oxygen rather than the temperature into Eq. (1), the adiabatic cooling effectiveness can be expressed as Eq. (2), as described by Charbonnier *et al* [33], where *MW* is the ratio of molecular weights of the coolant gas to the freestream gas..

$$\eta = 1 - \frac{1}{\left[\left(\left(p_{o_2}\right)_{air} / \left(p_{o_2}\right)_{mix}\right)_{wall} - 1\right] MW + 1}, \qquad (2)$$

The pressures in Eq. (2) can be computed using the recorded intensity of emission light, which is directly related to the partial pressure of oxygen. The mathematic function between normalized intensity and partial pressure can be obtained through a dedicated PSP calibration process. Detailed information on how to perform a PSP calibration can be found in references [34,35].

For the PSP image processing, in order to reduce the effects of camera noise on the measurements, spatial averaging was performed in the present study on square interrogation windows of 9×9 pixels with 50% overlap to ensure complete sampling of the measurement data. The acquired PSP images have a magnification of 0.085 mm/pix, which results in a spatial resolution of 0.34 mm or 0.03*D* for the PSP measurement results. The measurement uncertainty for the centerline effectiveness in the present study was estimated to be on the order of 3% for $\eta = 0.5$ and 5% for $\eta = 0.3$ (absolute uncertainty within $\Delta\eta$=0.02 throughout the entire interest). For laterally-averaged effectiveness, it was about 7% for $\eta = 0.3$ and 10% for $\eta = 0.2$ (absolute uncertainty within $\Delta\eta$=0.03). These estimations were predicted based on the Taylor Series Method [36,37]. Further measurement uncertainty analysis of using PSP technique can be found in Johnson and Hu [38].

2.3 Flow field measurements using the PIV and stereoscopic PIV (sPIV) technique.

A high-resolution PIV system was used to conduct detailed flow field measurements to quantify the dynamic interaction and mixing processes between the coolant and mainstream flows over the test plate. Figure 3 shows the schematic of the experimental

setup for the PIV measurement. During the experiment, the mainstream airflow and the cooling jets were seeded with ~1 μm oil droplets generated by a theatrical fog machine and an oil droplet generator, respectively. Illumination was provided by a double-pulsed Nd:YAG laser (NewWave Gemini 200) adjusted on the second harmonic and emitting two pulses of 200 mJ with the wavelength of 532 nm at a repetition rate of 10 Hz. Using a set of high-energy mirrors and optical lenses, the laser beam was shaped into a thin light sheet with a thickness in the measurement interest of less than 1 mm. The illuminating laser sheet was first aligned along the mainstream flow direction, bisecting the coolant hole in the middle of the test plate, to conduct PIV measurements in the *X*-*Y* plane. The laser sheet was then rotated 90 degrees to reveal the flow structures in the cross plane normal to the mainstream direction. This allowed us to perform sPIV measurements in the *Y*-*Z* planes at several locations downstream of the coolant exits.

For the sPIV measurements in the *Y*-*Z* planes, two high resolution 14-bit (2048 pixel × 2048 pixel) high-resolution CCD cameras (PCO2000, Cooke Corp.) were used for the sPIV image acquisitions. The two cameras were placed downstream of the test plate, with an angular displacement configuration (~45 degrees) to get a large overlapped view. With the installation of tilt-axis mounts, laser illumination plane, the lenses and camera bodies were adjusted to satisfy the Scheimpflug condition. The CCD cameras and double-pulsed Nd:YAG laser were both connected to a Digital Delay Generator (Berkeley Nucleonics, Model 565), which controlled the time interval of the lasers and image acquisition. A general in-situ calibration procedure was conducted to obtain the mapping functions between the image planes and object planes for the sPIV measurements. A target plate (~150 × 100 mm^2) with 1.0 mm-diameter dots spaced at intervals of 2.0 mm was used for

the in-situ calibration. The mapping function used in the present study was a multi-dimensional polynomial function, which is fourth order for the directions parallel to the laser illumination plane (i.e., *Y* and *Z* directions), and second order for the direction normal to the laser sheet plane (i.e., *X* direction). The coefficients of the multi-dimensional polynomial were determined from the calibration images by using a least-square method. For the PIV image processing, instantaneous PIV velocity vectors were obtained by using a frame-to-frame cross-correlation technique with an interrogation window size of 32 pixels ×32 pixels. An effective overlap of 50% of the interrogation windows was employed in PIV image processing, which results in a spatial resolution of 0.7 mm (0.06*D*) for the PIV measurement results. Similar process methodology was used for sPIV image processing, except a recursive interrogation window size changing from 64^2 pixels to 32^2 pixels was utilized for the sPIV processing to acquire the two-dimensional instantaneous velocity vectors. The acquired instantaneous vectors were then used to reconstruct all three components of the velocity vectors in the laser sheet planes through the mapping functions obtained by the calibration procedure. After the instantaneous velocity vectors (u_i, v_i, w_i) were determined, the distributions of the ensemble-averaged quantities such as mean velocity, normalized stream-wise vorticity ($\overline{\omega}_x = \frac{D}{U_\infty}(\frac{\partial w}{\partial y} - \frac{\partial v}{\partial z})$), and normalized turbulence kinetic energy (i.e., $N.TKE = 0.5\left(\overline{u'^2} + \overline{v'^2} + \overline{w'^2}\right)\Big/U_\infty^2$) were obtained from a sequence of 1000 realizations of instantaneous vector fields. The measurement uncertainty level for the velocity vectors is estimated to be within 3%, while the uncertainties for the measurements of ensemble-averaged flow quantities such as Reynolds stress and turbulent kinetic energy distributions are about 5%.

3. Results and Discussion

The reliability of the PSP technique as an effective experimental tool for turbine film cooling had been validated through a series of comparisons in previous work [24,35], using the PSP measurements against those derived directly from temperature-based measurements. The measured PSP results were found to agree well with the archived film cooling results. Therefore, the PSP technique is a suitable method to study the effectiveness of film cooling in the present study.

3.1 Effect of dune shape on film cooling effectiveness.

The film cooling performance of three types of BDSICs were examined in great detail in comparison with the circular hole to study the dune shape effect on film cooling. Figure 4 shows the spatial distribution of film cooling effectiveness for (a) circular hole, (b) BDSIC with shorted dune, (c) BDSIC with normal dune, and (d) BDSIC with elongated dune, respectively. As shown clearly in Figure 4, the film coverages of BDSICs were found to be more uniform and wider than the circular. For M=0.6, though the circular hole was found to exhibit a decent film coverage, the BDSIC cases demonstrated an even wider spatial distribution than the baseline with the help of dune cover. Increasing M to 0.9 and 1.2, the contours of the circular hole became narrower and shorter. It manifests the high momentum jets could have separate from the test surface. On the contrary, the film coverages of BDSIC cases, which were significant higher than the circular hole, were found to keep increasing as the M increased. In addition, it is obviously that the BDSIC with the elongated dune presented the widest spatial distribution among all BDSICs.

More quantitative information of cooling performance can be found in Figure 5, which shows the detail comparisons of effectiveness of film cooling between circular hole and BDSICs, where the lateral-averaged effectiveness was computed over a domain of -1.5<z/*D*<1.5. It is obviously that both the centerline and lateral-averaged effectiveness of BDSICs were found to be much higher than that of the circular hole, especially for high mass flux ratio cases. The circular jet tends to take off from the plate and penetrates into the freestream as the jet momentum increases. As for the BDSICs, the inclined jet would be, however, suppressed down by the dune cover and spread uniformly on the test plate, which leads to significantly higher effectiveness than circular hole.

Analyzing the results of all cases, the BDSIC with elongated dune was found to demonstrate the highest cooling performance, followed closely by the normal and the shorted dune. For the BDSIC film cooling, the coolant stream would first bleed out of the circular tube, then impinge on the dune cover, and tangentially inject into the mainstream flow. During this process, the length of the dune cover is a critical parameter that affects the coolant jet behavior. A dune with longer cover would be able to completely prevent the separation of coolant jet from surface, otherwise a small part of gas would escape from the cover and pierce into the cross-flow, resulting in reduced cooling performance. Therefore the BDSIC with elongated dune is able to provide an enhanced effectiveness in comparison to the other two dunes.

In general, the BDSIC with elongated dune can greatly improve the effectiveness of circular hole, exhibiting an augmentation of over 30%, 150%, and 500% in lateral effectiveness at *M*=0.6, 0.9, and 1.2 respectively. From now on, all of the following BDSIC configuration represents the elongated dune case in the present paper.

3.2 PIV measurements for circular hole and BDSIC configuration.

As described above, a high-resolution PIV system was used in the present study to conduct detailed flow field measurements to reveal the dynamic interactions between the mainstream and coolant stream ejected from BDSIC in comparison to that of circular hole, where the laser sheet was aligned along the middle plane of coolant hole (i.e., *X*-*Y* plane as shown in Fig.3). Figure 6 shows the PIV measurements for circular hole and BDSIC with elongated dune at *M*=0.9, where the carbon dioxide was used as coolant and the corresponding velocity ratio (U_c/U_∞) was 0.6. The measured PIV results are in the terms of instantaneous vorticity, ensemble-averaged velocity field, and normalized in-plain TKE ($0.5\left(\overline{u'^2}+\overline{v'^2}\right)\Big/U_\infty^2$).

As shown clearly in Fig. 6 (a), a series of unsteady vortex structures were found to be generated and shed periodically from the interface of jet and cross-flow. It indicates that the coolant jet was mixed intensively with the mainstream flow, which would dilute the potential of coolant as a heat sink to lower the mean temperature of the turbine blade. In Fig. 6 (b), it is obvious that the coolant from the circular hole was found to lift off from the surface and penetrate into the mainstream. However, the jet from the elongated BDSIC was found to tangentially inject out of the dune and remained on the surface as designed. It reveals that the effectiveness of BDSIC should be much higher than the circular hole, which is consistent with the PSP results shown in Fig. 5. It is well-known that a coolant jet would take off from the surface if its momentum is sufficient to overcome the resistance from cross-flow. It is what happed in circular hole at *M*=0.9. With the help of hollowed

dune, the inclined jet would be bent to level as it impinges on the dune, ensuring the attachment of coolant stream. Therefore the BDSIC configuration can greatly enhance the coolant coverage of the original hole, especially for high momentum cases.

Turbulence kinetic energy (*TKE*), as an index to evaluate the level of the fluid mixing, is an important turbulent quantity that can be applied to reflect the extent of heat transfer process. The heat transfer process pertinent to film cooling is closely related to the magnitude of *TKE*. A jet-in-cross-flow characterized with high *TKE* in turbine engine could lead to enhanced heat transfer between hot gas and engine parts. Fig. 6 (c) shows the comparison of normalized in-plain *TKE* distribution between circular hole and BDSIC film cooling. As shown clearly in the figure, there was a drastic increase of in-plain *TKE* level at the near hole region for circular hole, then decreased gradually as flow moved downstream. But, the BDSIC case avoided the severe flow interaction at the exit of hole. Due to the appearance of dune, the coolant stream was guided tangentially into the cross-flow, where the turbulent mixing within them was greatly alleviated. Also, the in-plan *TKE* distribution of BDSIC film cooling was found to be a bit lower than that of circular hole at the surface of interest, especially for the near hole region. Thus, the heat transfer coefficient in BDSIC might be lower than circular hole due to the weaker *TKE* level behind the dune. In general, the BDSIC could improve the film cooling effectiveness without enhancing the in-plain *TKE* level.

3.3 Stereoscopic PIV measurements for circular hole and BDSIC configuration.

Film cooling as a state of art, fundamentally, is a jet-in-cross-flow (JICF) problem. The dominated features of a JICF include jet shear-layer vortices formed at the leading

edge of jet, horseshoe vortices around the jet, CRV pair in the jet, and wake vortices downstream of jet flow [39,40]. One major problem of film cooling technique is the separation of coolant jet from blade surface, caused by the CRV, leading to a deteriorated cooling performance in the engine. Researchers are trying to reduce the detrimental vortex induction by introducing a pair of Anti-CRV to cancel the vorticity of CRV from the coolant stream. Proposed designs such as anti-vortex hole (Heidmann *et al.* [13] and Dhungel *et al*. [14]), vortex generators (Zaman *et al*. [20], Shinn *et al*. [21], and Zhou and Hu[24]) had been studied and proved a vorticity cancellation effect that postponed the jet separation. All of these ideas achieved reduced strength of CRV, but it will be much better if the CRV can be completely eliminated.

To reveal the underlying physics pertinent to BDSIC film cooling, a stereoscopic PIV measurement was performed to study the turbulent quantities, such as vorticity and turbulence kinetic energy. The measured results are shown in Fig. 7, where the mainstream flow was directed in positive *X*-direction (inside the paper), and the plotted vectors were the resultant vectors of in-plane velocities (*V* and *W*). As shown clearly in Fig. 7 (a), the CRV pair was found to be the salient feature for the circular case. It is obviously that the coolant gas in circular hole was found to roll up from the near-wall region and pumped into the mainstream, causing the formation of strong upwash flow. However, the flow behind BDSIC changed remarkable that only a pair of Anti-CRV was captured in *Y-Z* plane at *x/D*=5.0, while the complete disappearance of CRV pair is particularly interesting. When the incoming flow approaches the dune, the flow near the center plane of dune would climb over the crest and interact with the jet stream. Away from the center of dune, the energetic flow would impinge on the horns, and part of the stream would diverge and

travel forward, while some would stagnate there. As a results, the pressure of the stagnation flow is much higher than the inner side of dune, thus it would circularly roll over the horns and generate the Anti-CRV in the wake. This process is similar to the formation of wingtip vortex. Due to the sustained entrainment of coolant from stream to surface, the formed Anti-CRV is able to create symmetric downwash regions, resulting in wider coolant coverage on the surface of interest. As for the elimination of CRV, it is the result of inner channel of dune. Similar to a tangential slot, the inclined coolant would be guided tangentially out once it hits the cover, therefore coolant stream would be able to remain on the plate.

Fig. 7 (b) shows the normalized vorticity evolution along the streamwise direction for the circular and BDSIC cases at x/D=-1, 5, 10. It is apparent that the vorticity field of circular hole was characterized with a pair of CRV, which was found to decrease gradually as it flowed downstream to x/D=10. But the horseshoe vortex wasn't obvious in the figure due to its relative weak strength. Comparing to the circular case, the vorticity field of BDSIC was slightly different. The Anti-CRV in the BDSIC configuraton was found to be located at each side of dune rather than stay together within the coolant jet, and the signs of vorticity were opposite to that of CRV, as expected.

The comparison of $N.TKE$ contours between the circular and BDSIC cases was shown in Fig. 7 (c), which was found to display a similar magnitude with the in-plain TKE distribution in Fig. 6 (c). Due to the intensive interaction within coolant and mainstream, the $N.TKE$ level of circular hole at x/D=-1 is significant higher than that of the BDSIC. But it dropped down to a level close to the BDSIC case at x/D=5, and slightly lower magnitude at further downstream x/D=10. It is because the downstream coolant has

already lifted off and mixed well with the mainstream. Also, the evolution of *N.TKE* distribution in the circular hole confirmed the separation of coolant stream from the surface, while it remains attached on the surface for the BDSIC.

3.4 Influence of mass flux ratio.

To study the influence of mass flux ratio on effectiveness of film cooling, a series of PSP experiments were conducted at M=0.6, 0.9, 1.2, and 1.5, respectively. As revealed in Fig. 8, the effectiveness of BDSIC were found to keep increasing as the mass flux ratio increased. With the assistance of dune cover, the coolant jet from BDSIC, unlike traditional cooling holes, would stay attached on the surface despite its momentum augmentation, which is a crucial feature for fluctuated coolant supply condition in a real engine. The results also reveal that the enhanced ratio of effectiveness was found to be smaller at a higher M. An increase in M would improve the amount of coolant gas, but this beneficial effect is counteracted by a more rapid rate of mixing between the coolant and cross-flow, which results in larger amount of mainstream gas entrainment. The net result is that effectiveness becomes less sensitive to mass flux ratio. Also, this phenomenon is partially attributed to the insufficient length of dune cover. In fact, a small part of the coolant was found to inject into the cross-flow at high M and interact with it at the exit of the dune. Therefore, further improvement of BDSIC film cooling can be achieved by the extension of dune length.

In the present study, the incoming boundary layer was tripped by a Barchan dune, and the ‘leaked’ gases from the inclined jet interacted with cross-flow that facilitated the transition of flow from laminar to turbulence. Therefore the BDSIC’s cooling concept was

more complex than the slot film cooling, and all existing slot models [41] failed to correlate the measured effectiveness. For a certain amount of coolant, the best cooling strategy is all the coolant spread uniformly on the test plate, such as slot cooling, which is the highest effectiveness that BDSIC could possible reach. A slot model proposed by Ballal and Lefebvre [42] (Eq. (3)) was used to compute the ideal cooling effectiveness shown in Fig. 9. It is as expected that the effectiveness of the slot was found to be higher than that of BDSIC configuration. The difference between the model and measured effectiveness indicates that the ideal potential of BDSIC can be achieved by further optimization.

$$\eta = 1.28\left(\frac{\mu_c}{\mu_\infty}\right)^{0.15}\left(\frac{x}{s}\right)^{-0.2}\left(\frac{t}{s}\right)^{-0.2} \tag{3}$$

where s is the height of dune (assuming coolant flowed out from equal-area slot, $\pi D/8$), μ_c and μ_∞ are the dynamic viscosity of coolant and mainstream respectively, and t is the lip thickness ($0.1D$).

3.5 Influence of density ratio.

Figure 9 shows the influence of density ratio on film cooling effectiveness between the circular hole and BDSIC at M=0.9. The desired density ratios (DR=0.97, 1.53, and 2.1) were achieved by using N_2, CO_2 and a mixture of SF_6 and CO_2, respectively. As revealed clearly in Fig. 9, the effectiveness of circular hole was found to increase as the density ratios increase, similar to published results [7]. At a fixed M, the jet momentum is higher for a lighter coolant, leading to jet detaching and lower effectiveness, vice versa, thus denser coolant tends to stay closer to the surface. But, the effectiveness of BDSIC were

similar at different ratios, indicating a weak dependent upon the density ratio. Due to the appearance of dune cover, the coolant jet would hit the inner surface and inject tangentially into the cross-flow disregarding the density difference, resulting in close effectiveness. Inspection of the curves in Figure 9, the BDSIC exhibited a slight increase in effectiveness near the hole region as the density ratio increased, while decreasing in the far field range. As discussed above, the jet momentum of denser coolant is lower, which leads the coolant to accumulate near the hole region. What's more, the amount of gas that can be used to cool the surface is smaller compared to a lighter case. These are the reasons why the profiles were shifted in the far field region. Since similar phenomenon can be observed for M=0.6 case, only M=0.9 case is shown here for conciseness.

3.6 Hole interaction effect on film cooling.

In order to explore the hole interaction effect on film cooling, a PSP measurement was performed over a single BDSIC and an array of BDSICs respectively, as shown in Figure 10. The BDSIC array consists of three identical dunes and the span-wise pitch is 3D between these holes. Up until now, all of the BDSICs discussed above are single dune. As shown in Figure 10, it is interesting that the centerline effectiveness of single BDSIC was slightly higher than that of BDSIC array, while lateral-averaged effectiveness was lower. This phenomenon is caused by the "Bernoulli's principle" -- a jet tends to be attracted to the nearby object. Since the physical distance between dunes is small, the middle jet was attracted by the adjacent streams to spread wider over the surface, leading to higher lateral-averaged effectiveness, but lower centerline values. This process can be seen clearly in the lateral distributions shown in Figure 10 (e) & (f), where the profiles were obtained by

extracting the effectiveness from the spatial distributions of film cooling at x/D=6, 10, respectively.

3.7 Aerodynamic loss.

The aerodynamic loss coefficient was studied to yield some insight into the nature of loss generated in BDSIC film cooling. There are varieties of methods to calculate the aerodynamic loss, such as based on thermodynamic loss, entropy loss, total pressure loss, and so on. As for more information, please refer to the review paper by Ligrani [43]. Based on total pressure deficit, Lee *et al.* [44] investigated the aerodynamic loss of a compounded film-cooling jet. But, this method fails to deliver the actual net aerodynamic loss in film cooling since the energy from the coolant jet doesn't take into account. To account for the total pressure of coolant into mainstream, the aerodynamic loss in present study was computed using the kinetic energy loss method (Eq. (6)), proposed by Sargison[15], which gives a more realistic picture of the aerodynamic penalty incurred by film cooling. It is worth mentioning that the coolant used here is air (DR=1). There are four pressure taps around the plenum that used to monitor the total pressure of jet. The wall pressure downstream was measured by a row of pressure taps. Performing the kinetic energy balance in a defined control volume ($-2D<x<10D$, $0<y<2.5D$, and $-3D<z<3D$), the aerodynamic loss was acquired through computing the energy difference between flow-in and flow-out. The measurement uncertainty is estimated to be about 10%.

$$Loss = 1 - \frac{0.5\rho v_2^3 A}{\frac{\dot{m}_m}{\rho_m}\left(P_{om} - P_2\right) + \frac{\dot{m}_c}{\rho_c}\left(P_{oc} - P_2\right)} \tag{4}$$

where A is the area of cross-section located 10D downstream (15D^2); ρ is the density of mixed gas downstream; v_2 is the velocity downstream (bulk velocity was used here); P_2 is the wall pressure downstream; $\dot{m}_m$ is the mainstream mass flow rate; P_{oc} is the coolant total pressure; and P_{om} is the freestream total pressure.

Figure 11 illustrates the aerodynamic loss coefficient as a function of mass flux ratio for a circular hole and single BDSIC. For the circular hole, the entrance loss (penetration process) and mixing loss are the major losses encountered in film cooling. It is similar for BDSIC film cooling except the additional profile loss generated by the dune, which is about 3.5% when the coolant was off. As shown in Figure 11, the aerodynamic loss of circular hole was found to be slightly lower than that of BDSIC at first, but it gradually caught up and surpassed BDSIC at about M=1.3. If the profile loss was excluded from the BDSIC, the loss of circular hole was found to exceed the BDSIC as M>0.9. At low M, such as M=0.6, the boundary layer mixing loss is the primary loss since both jets stay on the surface. Due to the wider film coverage, the mixing loss of BDSIC is slightly higher than the circular hole. But, the flow feature changed dramatically as the coolant momentum increased. From the PIV results (Fig. 6), the circular coolant jet was found to lift off and penetrated into the mainstream flow at a high M, but it remained on the surface with the help of dune cover. Therefore the loss generated by the penetration process in the circular hole, which is directly proportional to the strength of jet momentum, is greater

than that of BDSIC configuration. Therefore the BDSIC does help reduce the aerodynamic loss at a relatively high mass flux ratio.

4. Conclusion

An experimental study was performed to examine the film cooling effectiveness of proposed Barchan-Dune-Shaped Injection Compounds (BDSIC). The PSP technique was used to measure the adiabatic film cooling effectiveness on the surface of interest, while a high-resolution PIV system was used to conduct detailed flow field measurements in order to reveal the underlying physics pertinent to film cooling. The effects of dune shape (shorted, normal, and elongated dune), mass flux ratio (M=0.6, 0.9, 1.2, 1.5), density ratio (DR=0.97, 1.5, 2.1), and hole interaction on the film cooling effectiveness were studied in great detail based on quantitative PSP and PIV measurements. In addition, the aerodynamic loss coefficient was studied to uncover the nature of loss generated in BDSIC film cooling.

It was found that the BDSICs can significantly enhance the film cooling performance of a circular hole, especially the BDSIC with the elongated dune. Comparing to the circular hole, there are over 30%, 150%, and 500% gains in lateral effectiveness for BDSIC with elongated dune at M=0.6, 0.9, and 1.2 respectively. Investigation of flow physics using PIV and stereo-PIV showed three distinct mechanisms for the enhancement of effectiveness in BDSIC with elongated dune (i) continual suppression on the coolant stream provided by the arched dune, leaded to a stable and uniform coolant coverage, whose function is similar to a tangential slot, (ii) complete elimination of the CRV pair prevented the jet from lifting off, and (iii) the formation of Anti-CRV pair in Y-Z plane

generated downdraught of coolant from the jet core, and enhanced the lateral film coverage. Unlike traditional cooling holes, the effectiveness of BDSIC was found to keep increasing as the mass flux ratio increased. Meanwhile the potential of BDSIC film cooling which may be achieved by further optimization was revealed clearly by a slot model.

It is well-known that the density ratio has a great effect on the effectiveness of film cooling. However, the BDSIC exhibited a weak dependent upon the density ratio. Due to the appearance of dune, the coolant jet would hit the inner surface and eject tangentially into the main flow disregarding the density difference, leading to a close effectiveness. As for the hole interaction effect, the BDSIC array showed slightly higher lateral-averaged effectiveness than a single dune, which is caused by the Bernoulli's principle. Considering the aerodynamic loss, though the BDSIC displayed augmented loss at first, the circular hole gradually caught up and exceeded BDSIC at a high *M*. Detailed analysis showed that the loss generated by the penetration process in the circular hole was much greater than that of BDSIC. With the help of dune cover, the aerodynamic loss was reduced at a high mass flux ratio.

All in all, the BDSIC configuration is a hybrid of Barchan dune and tangential slot film cooling, which inherits the merits from both dune and ideal slot. It is able to produce a greatly enhanced effectiveness with less aerodynamic loss at high mass flux ratio. This innovative design provides a promising solution for film cooling. It has self-cooling ability that the front part of BDSIC can be cooled intensively by the impingement cooling, while the tail part by the film cooling.

Reference

[1] Goldstein, R., 1971, "Film cooling," Advances in heat transfer 7.1, pp. 321–379.

[2] Bogard, D. G., and Thole, K. A., 2006, "Gas Turbine Film Cooling," J. Propuls. Power, **22**(2), pp. 249–270.

[3] Bogard, D. G., 2006, "Airfoil film cooling," The Gas Turbine Handbook, National Energy Technology Laboratory, Section 4.2.2.1.

[4] Baldauf, S., Schulz, A., and Wittig, S., 2001, "High-Resolution Measurements of Local Effectiveness From Discrete Hole Film Cooling," J. Turbomach., **123**(4), p. 758.

[5] Baldauf, S., Scheurlen, M., Schulz, A., and Wittig, S., 2002, "Correlation of Film-Cooling Effectiveness From Thermographic Measurements at Enginelike Conditions," J. Turbomach., **124**(4), p. 686.

[6] Wright, L. M., Gao, Z., Varvel, T. A., and Han, J.-C., 2005, "Assessment of Steady State PSP, TSP, and IR Measurement Techniques for Flat Plate Film Cooling," Heat Transfer: Volume 3, ASME, pp. 37–46.

[7] Han, J., Dutta, S., and Ekkad, S., 2012, Gas turbine heat transfer and cooling technology, Taylor and Francis, New York.

[8] Schmidt, D. L., Sen, B., and Bogard, D. G., 1996, "Film Cooling With Compound Angle Holes: Adiabatic Effectiveness," J. Turbomach., **118**(4), p. 807.

[9] Pedersen, D., 1977, "Film cooling with large density differences between the mainstream and the secondary fluid measured by the heat-mass transfer analogy," J. Heat Transfer, **99**(4), pp. 620–627.

[10] Sinha, A. K., Bogard, D. G., and Crawford, M. E., 1991, "Film-Cooling Effectiveness Downstream of a Single Row of Holes With Variable Density Ratio," J. Turbomach., **113**(3), p. 442.

[11] Bunker, R. S., 2005, "A Review of Shaped Hole Turbine Film-Cooling Technology," J. Heat Transfer, **127**(4), p. 441.

[12] Goldstein, R. J., Eckert, E. R. G., and Burggraf, F., 1974, "Effects of hole geometry and density on three-dimensional film cooling," Int. J. Heat Mass Transf., **17**(5), pp. 595–607.

[13] Heidmann, J. D., and Ekkad, S., 2008, "A Novel Antivortex Turbine Film-Cooling Hole Concept," J. Turbomach., **130**(3), p. 031020.

[14] Dhungel, A., Lu, Y., Phillips, W., Ekkad, S. V., and Heidmann, J., 2009, "Film Cooling From a Row of Holes Supplemented With Antivortex Holes," J. Turbomach., **131**(2), p. 021007.

[15] Sargison, J. E., 2001, "Development of a Novel Film Cooling Hole Geometry," PhD Dissertation, Dept. of Engineering Sci., University of Oxford.

[16] Bunker, R. S., 2002, "Film Cooling Effectiveness Due to Discrete Holes Within a Transverse Surface Slot," Volume 3: Turbo Expo 2002, Parts A and B, ASME, pp. 129–138.

[17] Lu, Y., Faucheaux, D., and Ekkad, S. V., 2005, "Film Cooling Measurements for Novel Hole Configurations," ASME 2005 Summer Heat Transfer Conference collocated with the ASME 2005 Pacific Rim Technical Conference and Exhibition on Integration and Packaging of MEMS, NEMS, and Electronic Systems, ASME, pp. 59–66.

[18] Gräf, L., and Kleiser, L., 2014, "Film Cooling Using Antikidney Vortex Pairs: Effect of Blowing Conditions and Yaw Angle on Cooling and Losses," J. Turbomach.

[19] Zaman, K. B. M. Q., and Foss, J. K., 1997, "The Effect of Vortex Generators on a Jet in a Cross-Flow," Phys. Fluids, **9**, pp. 106–114.

[20] Zaman, K. M., Rigby, D., and Heidmann, J., 2010, "Inclined Jet in Crossflow Interacting With a Vortex Generator," J. Propuls. Power, **26**(5), pp. 947–954.

[21] Shinn, A. F., and Pratap Vanka, S., 2013, "Large eddy simulations of film-cooling flows with a micro-ramp vortex generator," J. Turbomach., **135**(1), p. 011004.

[22] Na, S., and Shih, T., 2007, "Increasing adiabatic film-cooling effectiveness by using an upstream ramp," J. Heat Transfer, **129**(4), pp. 464–471.

[23] Sakai, E., Takahashi, T., and Agata, Y., 2013, "Experimental Study on Effects of Internal Ribs and Rear Bumps on Film Cooling Effectiveness," J. Turbomach., **135**(3), p. 031025.

[24] Zhou, W., and Hu, H., 2015, "An Experimental Study on Film Cooling Performance Behind Barchan Dune-Shaped Ramps Using PSP and PIV Techniques," Volume 5B: Heat Transfer, ASME, p. V05BT12A043.

[25] Palmer, J. A., Mejia-Alvarez, R., Best, J. L., and Christensen, K. T., 2011, "Particle-image velocimetry measurements of flow over interacting barchan dunes," Exp. Fluids, **52**(3), pp. 809–829.

[26] Christensen, K. T., Kazemifar, F., Blois, G., Barros, J. M., Tang, Z., Hamed, A., Kim, T., and Best, J. L., 2014, "Quantitative Studies of Environmental Flows at the Micro- and Macro-Scales," 16th International Symposium on Flow Visualization, Okinawa, Japan.

[27] Andreotti, B., Claudin, P., and Douady, S., 2002, "Selection of dune shapes and velocities Part 1: Dynamics of sand, wind and barchans," Eur. Phys. J. B - Condens. Matter, **28**(3), pp. 321–339.

[28] Horvat, B., "Barchan dunes Seminar 2," p. http://www–f1.ijs.si/~rudi/sola/Sem4.pdf.

[29] Hersen, P., Andersen, K., Elbelrhiti, H., Andreotti, B., Claudin, P., and Douady, S., 2004, "Corridors of barchan dunes: Stability and size selection," Phys. Rev. E, **69**(1), p. 011304.

[30] Bell, J. H., Schairer, E. T., Hand, L. A., and Mehta, R. D., 2001, "SURFACE PRESSURE MEASUREMENTS USING LUMINESCENT COATINGS 1," Annu. Rev. Fluid Mech., **33**(1), pp. 155–206.

[31] Eckert, E. R. G., 1992, "Similarity analysis of model experiments for film cooling in gas turbines," Wärme- und Stoffübertragung, **27**(4), pp. 217–223.

[32] Shadid, J. N., and Eckert, E. R. G., 1991, "The Mass Transfer Analogy to Heat Transfer in Fluids With Temperature-Dependent Properties," J. Turbomach., **113**(1), p. 27.

[33] Charbonnier, D., Ott, P., Jonsson, M., Cottier, F., and Köbke, T., 2009, "Experimental and Numerical Study of the Thermal Performance of a Film Cooled Turbine Platform," Proc. Asme Turbo Expo 2009, Vol 3, Pts A B, pp. 1027–1038.

[34] Yang, Z., and Hu, H., 2011, "Study of Trailing-Edge Cooling Using Pressure Sensitive Paint Technique," J. Propuls. Power, **27**(3), pp. 700–709.

[35] Johnson, B., Tian, W., Zhang, K., and Hu, H., 2014, "An experimental study of density ratio effects on the film cooling injection from discrete holes by using PIV and PSP techniques," Int. J. Heat Mass Transf., **76**, pp. 337–349.

[36] Sajben, M., 1993, "Uncertainty estimates for pressure sensitive paint measurements," AIAA J., **31**(11), pp. 2105–2110.

[37] Coleman, H. W., and Steele, W. G., 2009, Experimentation, Validation, and Uncertainty Analysis for Engineers, John Wiley & Sons.

[38] Johnson, B. E., and Hu, H., 2014, "Measurement Uncertainties Analysis in the Determination of Adiabatic Film Cooling Effectiveness by Using Pressure Sensitive Paint (PSP) Technique," Volume 1D, Symposia: Transport Phenomena in Mixing; Turbulent Flows; Urban Fluid Mechanics; Fluid Dynamic Behavior of Complex Particles; Analysis of Elementary Processes in Dispersed Multiphase Flows; Multiphase Flow With Heat/Mass Transfer in Process Tec, ASME, p. V01DT40A001.

[39] Fric, T. F., and Roshko, A., 1994, "Vortical structure in the wake of a transverse jet," J. Fluid Mech., **279**, pp. 1–47.

[40] Peterson, S. D., and Plesniak, M. W., 2004, "Evolution of jets emanating from short holes into crossflow," J. Fluid Mech., **503**, pp. 57–91.

[41] Lefebvre, A. H., and Ballal, D. R., 2010, Gas turbine combustion; alternative fuels and emissions, CRC Press.

[42] Ballal, D., and Lefebvre, A., 1973, "A proposed method for calculating film-cooled wall temperatures in gas turbine combustion chambers," ASME.

[43] Ligrani, P., 2012, "Aerodynamic Losses in Turbines with and without Film Cooling, as Influenced by Mainstream Turbulence, Surface Roughness, Airfoil Shape, and Mach," Int. J. Rotating Mach., **2012**, p. 28.

[44] Lee, S., Kim, Y., and Lee, J., 1997, "Flow characteristics and aerodynamic losses of film-cooling jets with compound angle orientations," J. Turbomach., **119**, pp. 310–319.

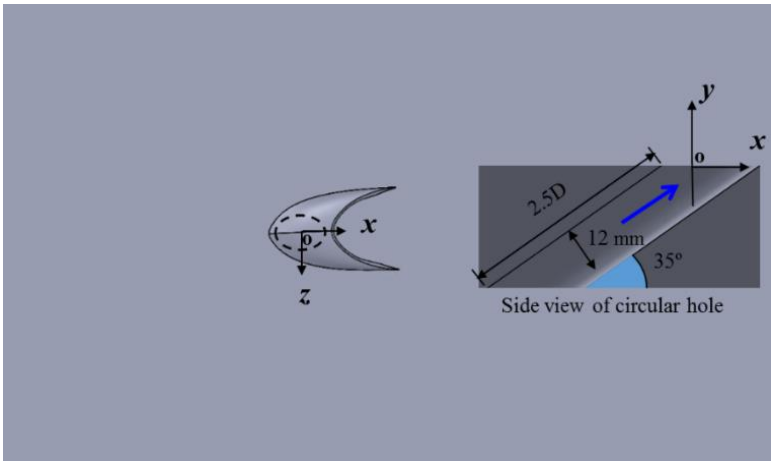

(a) BDSIC film cooling configuration (single hole)

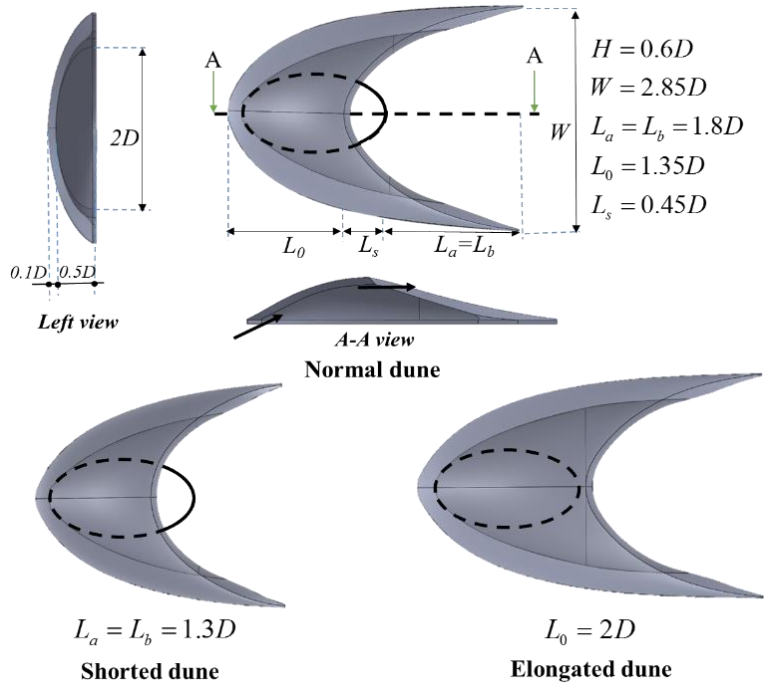

(b) Detailed dimensions of hollowed Barchan dune

Figure 1. *Schematic of the test models used in the present study (D is the diameter of coolant hole).*

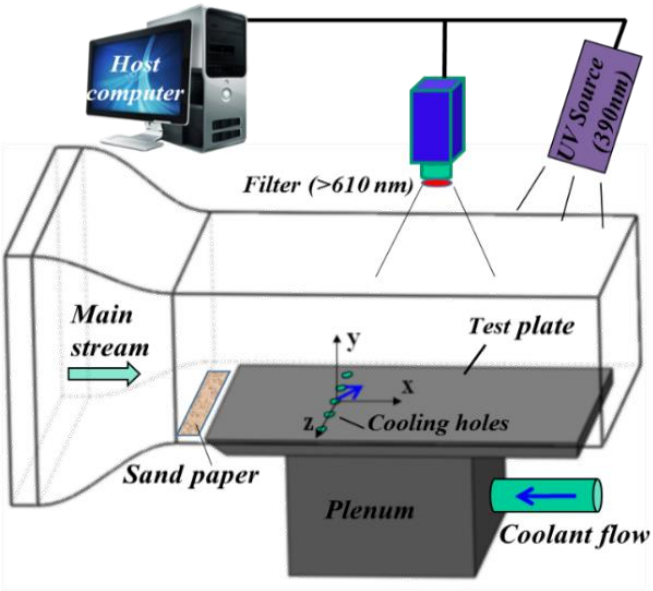

Figure 2. *Experimental setup for PSP measurements.*

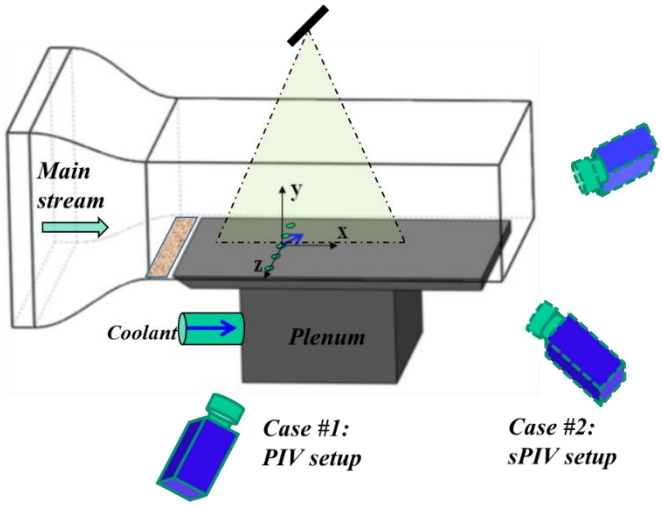

Figure 3. *Experimental test rig for PIV measurements.*

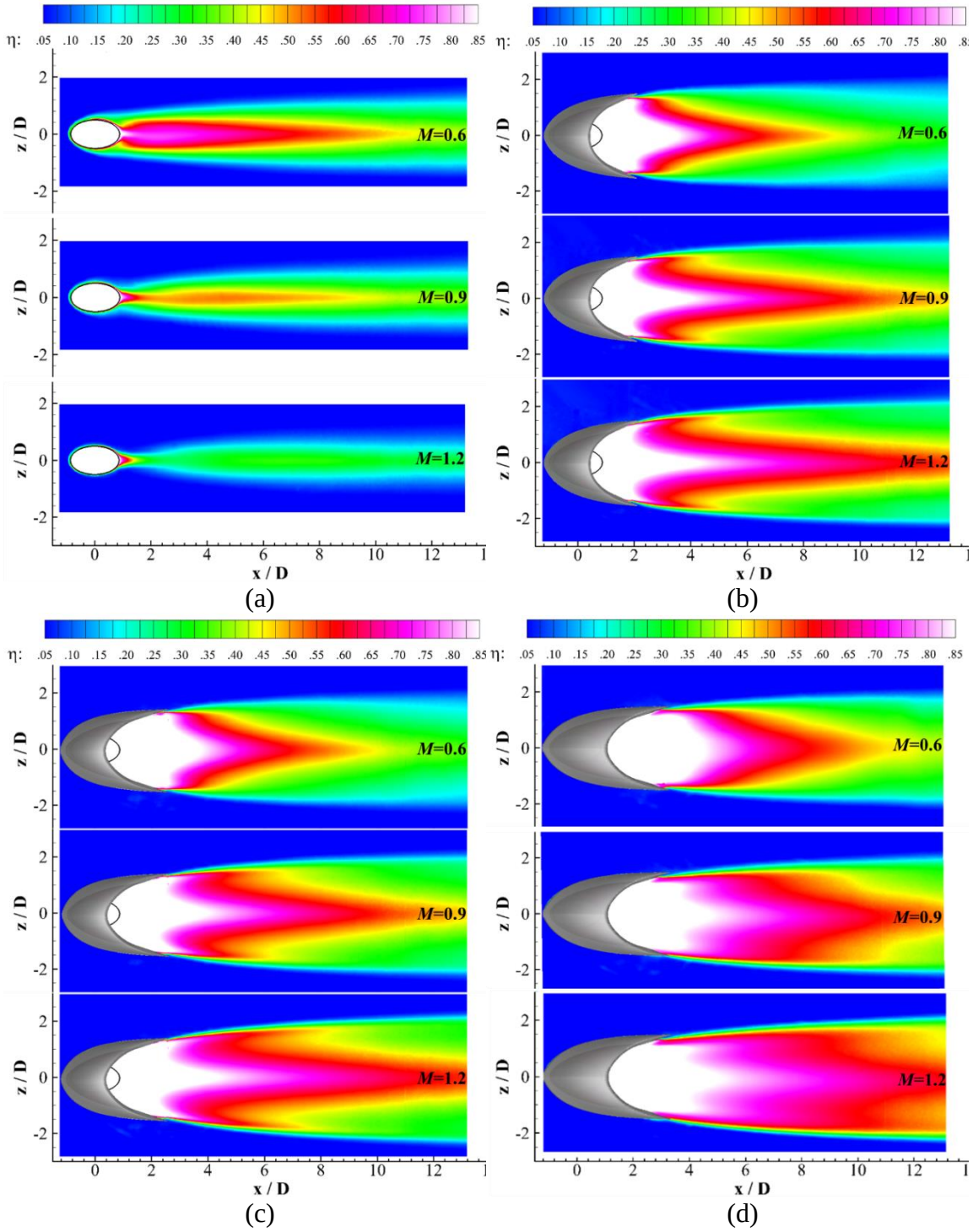

Figure 4. *Spatial distribution of film cooling effectiveness for different configurations at three mass flux ratios M=0.6, M=0.9, and M=1.2 , DR=1.53: (a) circular hole, (b) BDSIC with shorted dune, (c) BDSIC with normal dune, and (d) BDSIC with elongated dune.*

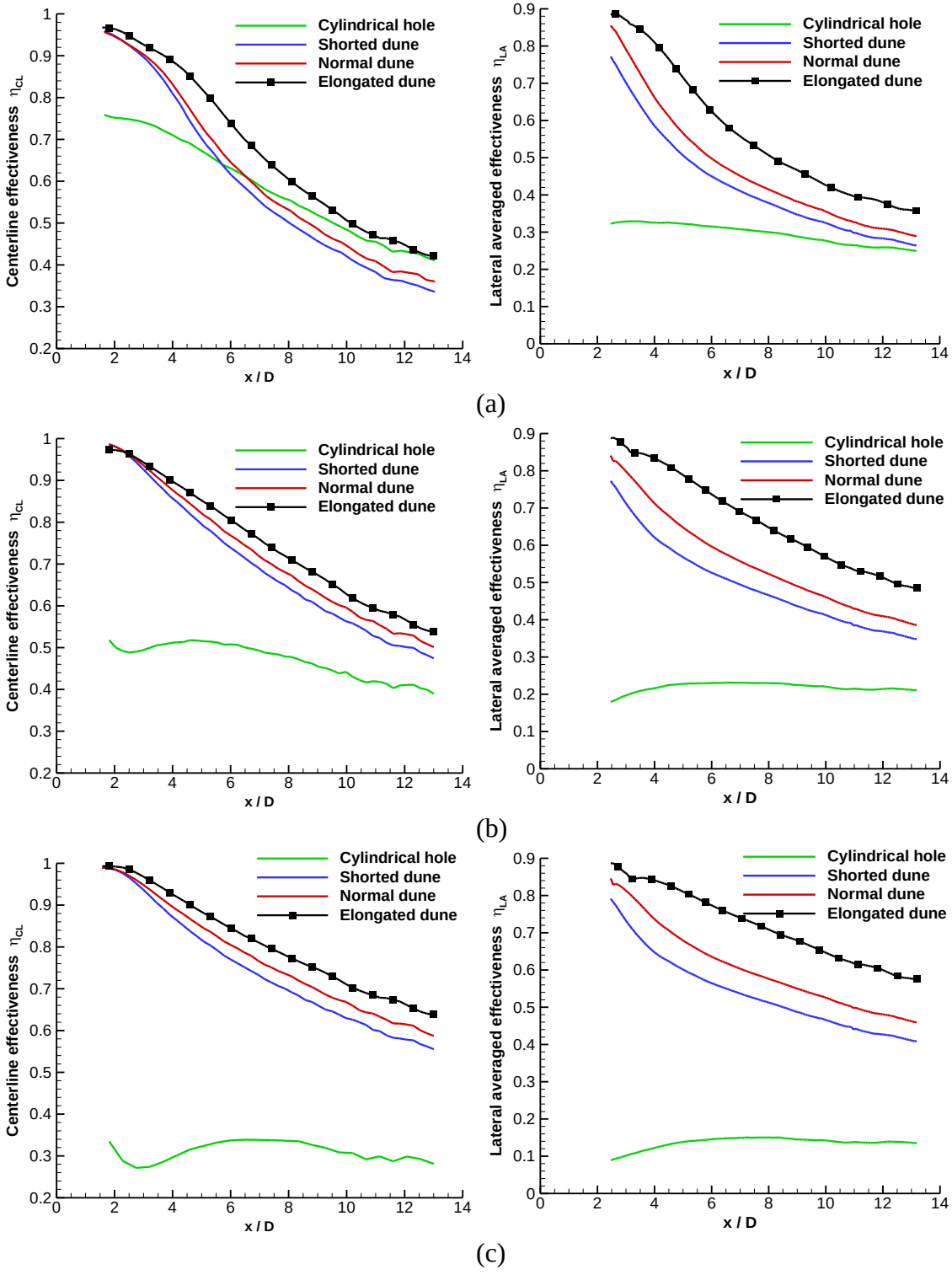

Figure 5. *Detailed film cooling effectiveness for different configurations at (a) M=0.6, (b) M=0.9, and (c) M=1.2 respectively, where DR=1.53.*

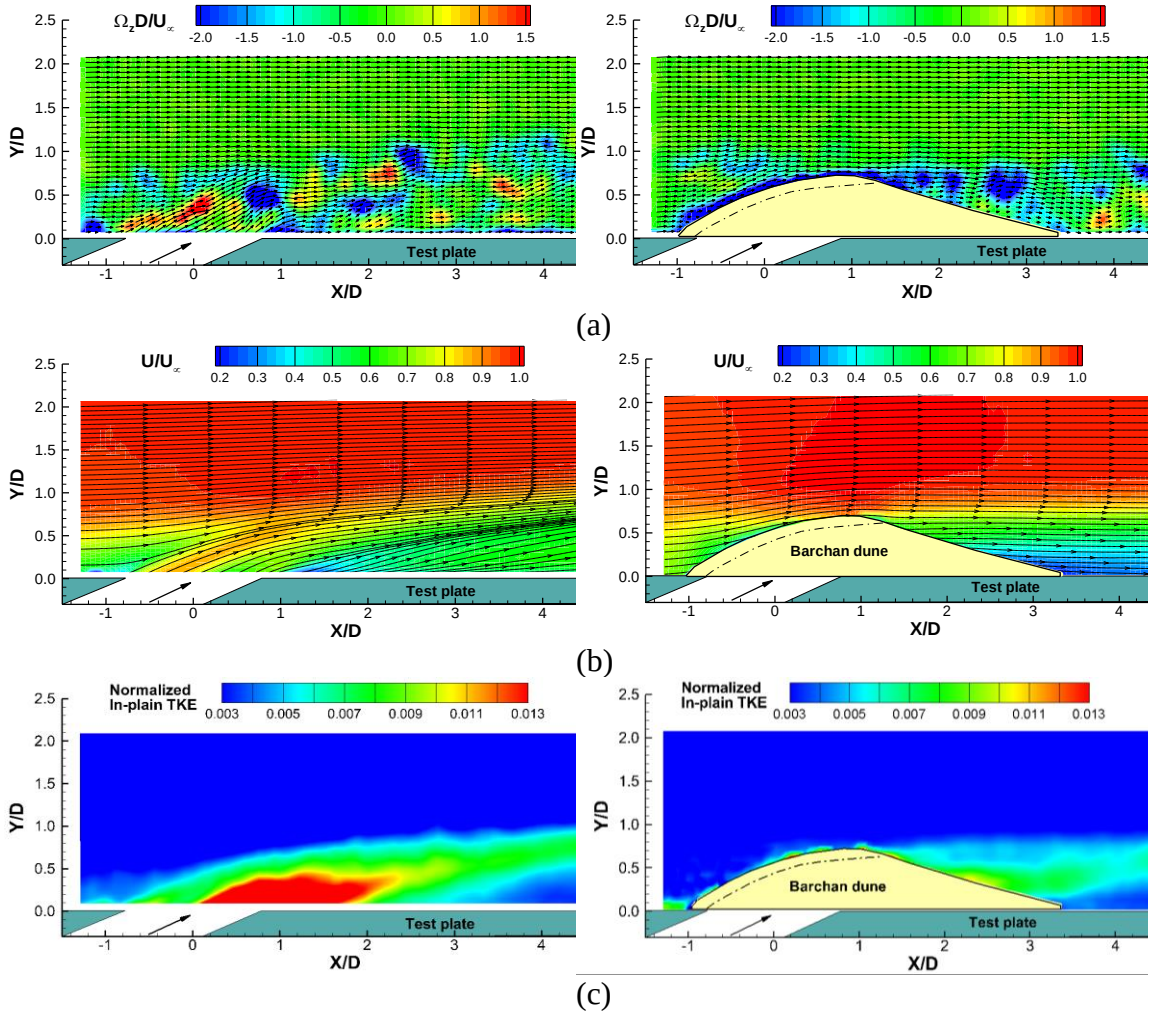

Figure 6. *Measured PIV results for circular hole (left) and BDSIC configuration (right) at M=0.9, DR=1.53: (a) instantaneous vorticity, (b) ensemble-averaged velocity, and (c) normalized in-plain TKE* $0.5\left(\overline{u'^2}+\overline{v'^2}\right)\Big/U_\infty^2$.

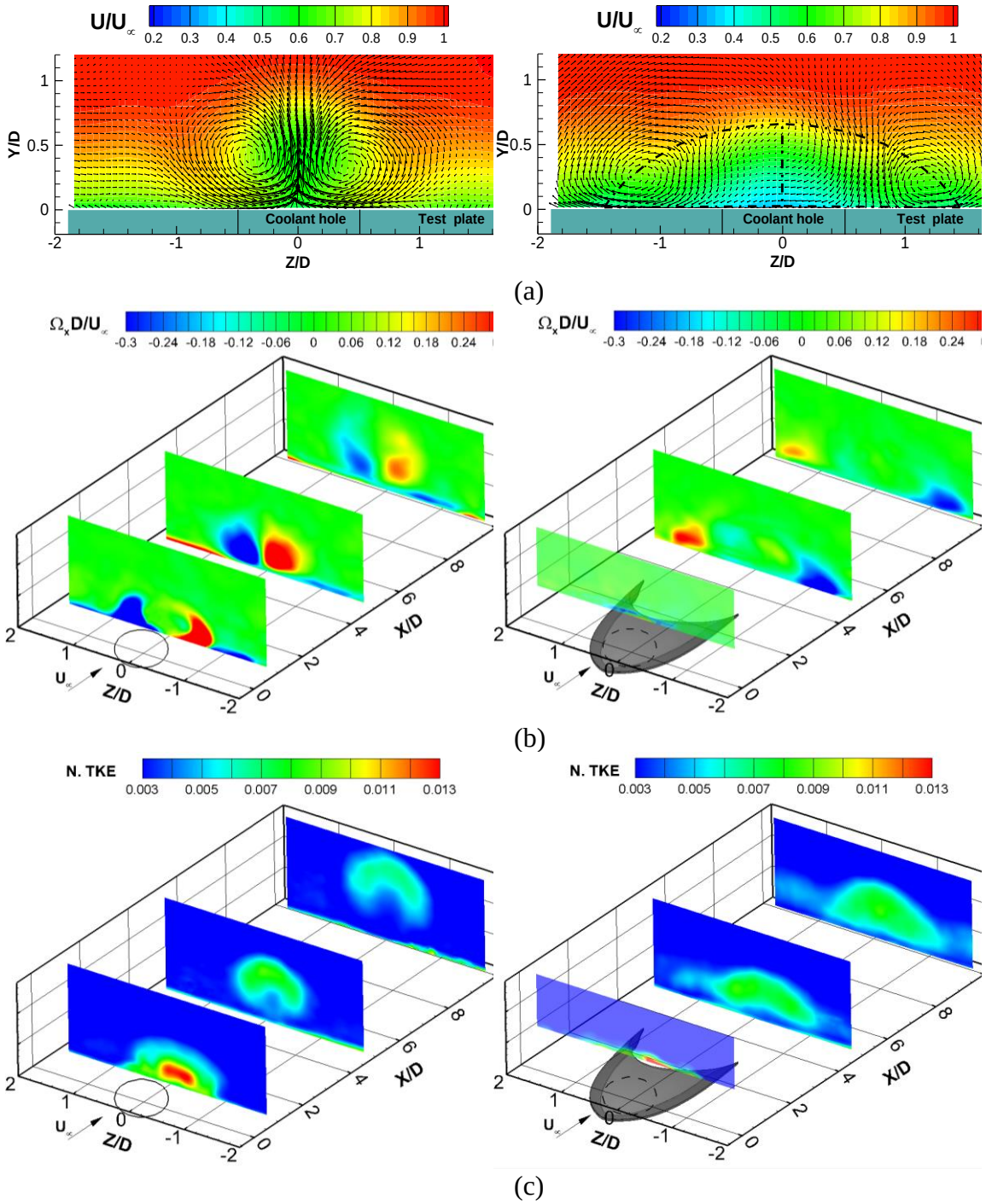

Figure 7. *Stereoscopic PIV results for circular hole (left) and BDSIC configuration (right) at M=0.9, DR=1.53: (a) ensemble-averaged velocity at the x/D=5.0 plane, (b) vorticity evolution along streamwise direction, and (c) N.TKE* $0.5\left(\overline{u'^2}+\overline{v'^2}+\overline{w'^2}\right)\Big/U_\infty^2$ *evolution along streamwsie direction.*

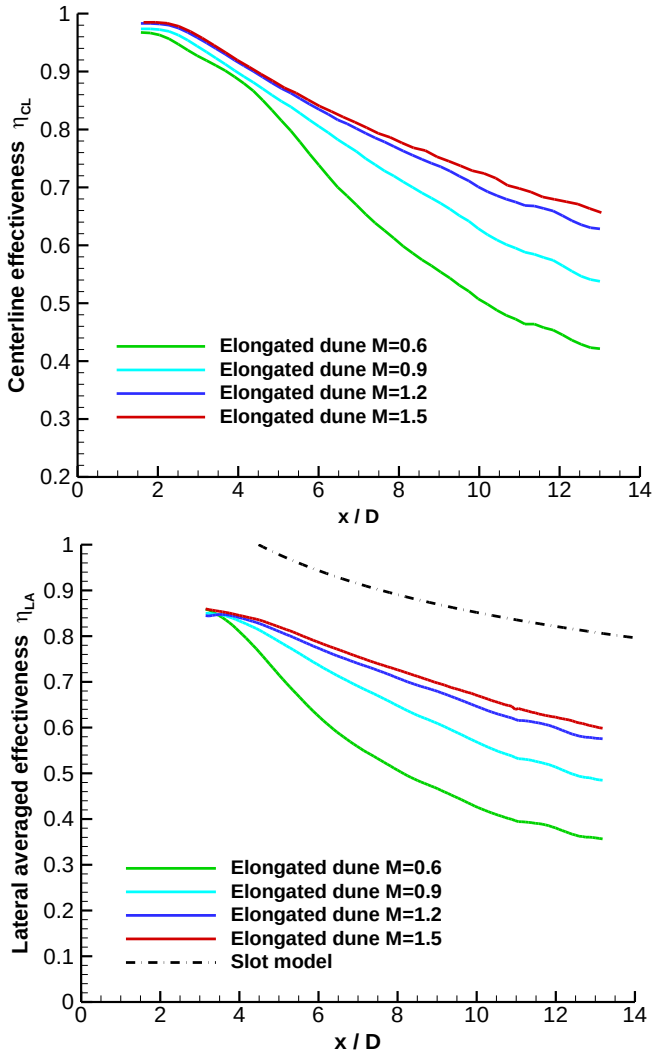

Figure 8. *Film cooling effectiveness as function of mass flux ratio at M=0.6, 0.9, 1.2, 1.5, where DR=1.53.*

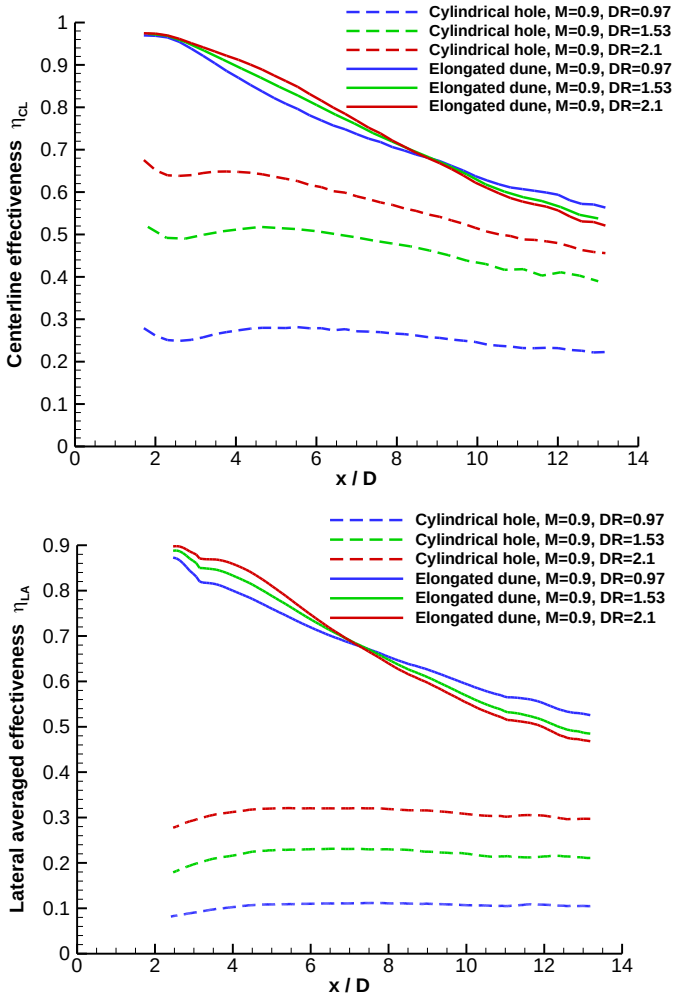

Figure 9. *Density ratio effect on film cooling effectiveness at M=0.9.*

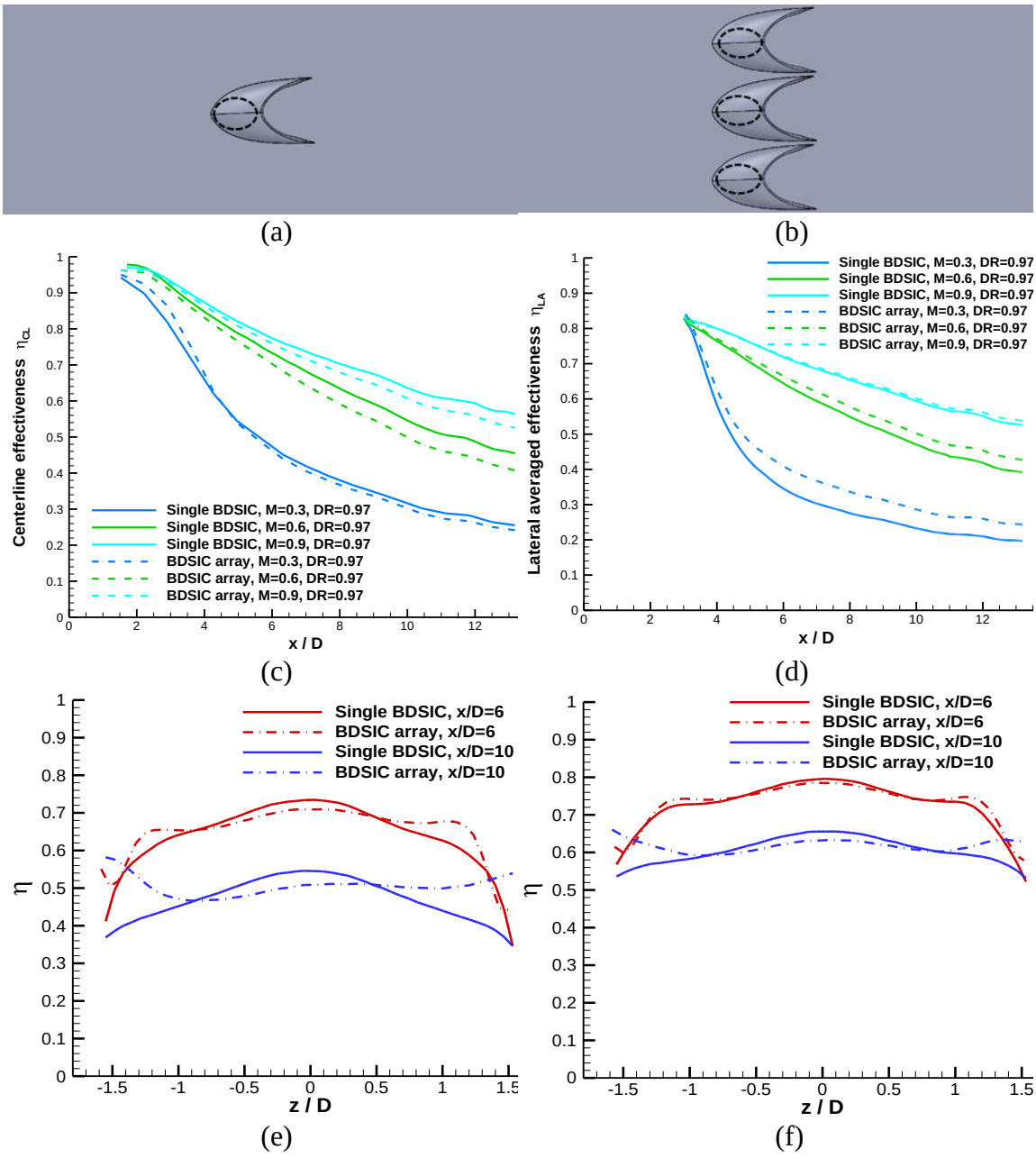

Figure 10. *Hole interaction effect on film cooling effectiveness at M=0.3, 0.6, 0.9: (a) Single BDSIC configuration, (b) BDSIC array configuration, (c) centerline effectiveness, (d) lateral-averaged effectiveness, (e) lateral effectiveness distribution at M=0.6, and (f) lateral effectiveness distribution at M=0.9.*

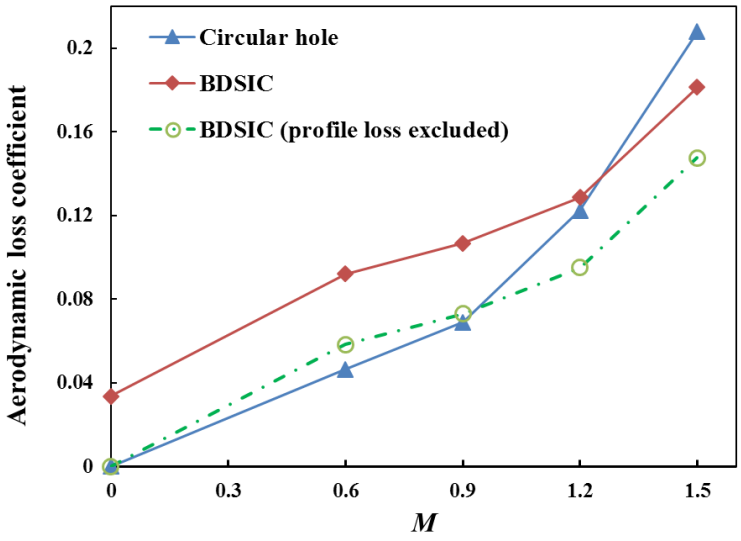

Figure 11. *Aerodynamic loss as function of mass flux ratio for circular hole and single BDSIC.*

CHAPTER 4

AN EXPERIMENTAL STUDY OF COMPRESSIBILITY EFFECTS ON THE FILM COOLING EFFECTIVENESS USING PSP AND PIV TECHNIQUES

Wenwu Zhou, Blake Johnson, Hui Hu

Department of Aerospace Engineering, Iowa State University, Ames, IA 50011, USA

ABSTRACT

An experimental study was performed to examine the compressibility effect (Ma=0.07, 0.30, 0.50, 0.70) on film cooling effectiveness by using the PSP and PIV techniques. The measured PSP results showed that the cooling effectiveness of circular hole was found to vary little at low mass flux ratio, but marginally increased at high mass flux ratio, as the external Mach number increased. Investigation of flow physics using the PIV technique showed similar velocity distributions for both Ma=0.07 and 0.30 at M=0.4, but slightly different velocity distribution was found at M=1.25, which were consistent with the PSP measurements.

1. Introduction

In search of higher thermal efficiency and power output of gas turbine engines, the turbine inlet temperature is continuously being pushed upward, causing the protection of turbine blades from extreme temperatures to be of critical importance. Film cooling technology has developed out of the necessity to protect turbine blades from damage mechanisms, such as corrosion and melting, despite the severe temperatures in which they operate. By releasing a film of coolant gas on the blade surface, the solid components can

be isolated from the hot gases in the turbine stage, hence increasing their lifetime. There is an inherent desire to optimize the cooling systems to further increase the efficiency of gas turbines, which can result in significant economic savings. Therefore, a better understanding of the physics of the film behavior is essential for such optimization.

A number of experimental studies have been conducted in recent years to understand the fundamental principle of film cooling and further improve the cooling effectiveness. Goldstein *et al.* [1] reported a remarkable enhancement of film cooling effectiveness by using fan-shaped holes, which employ a diffuser to reduce the momentum of the jet at the exit of the hole. Baldauf *et al*. [2,3] studied the influence of the mass flux ratio, density ratio, and other factors on film cooling effectiveness over a flat surface by using infrared thermography. Similar conclusions were reported by Johnson *et al.* [4], who studied the effect of density ratio on effectiveness of film cooling using the PSP and PIV techniques. Bogard [5,6] and Thole [6] provided a decent literature review of film cooling study, and found that the proposed empirical correlations failed to characterize the curvature effect, hole shape effect, and other effects on film cooling effectiveness of circular hole. As for more detailed information, please refer to the review papers by Bogard and Thole [6], and Bunker [7].

Up to now, comprehensive studies have been performed to understand the physics of film cooling. However, most of these experiments were conducted at relatively low Mach numbers (i.e., Ma<0.15) with the incoming airflow being incompressible. While the gas flow passing turbine blades is usually transonic, very little can be found in the literature examining the compressibility effect on film cooling effectiveness. One exception is Gritsch *et al*.[8], who measured the cooling effectiveness of single coolant hole over a

range of external Mach numbers (0.3, 0.60 and 1.2). Their infrared thermography results showed that the measured effectiveness has little dependence on Mach number. Liess [9] performed a similar study, but with positive pressure gradient along the test plate, that showed limit effect of compressibility on cooling performance. Researchers such as Dellimore *et al.* [10], Repukhov [11] and Parthasarathy *et al.* [12] studied the influence of compressibility on tangential-slot film cooling. They reported contradictory results and no consensus regarding the effect of compressibility had emerged. Therefore it is necessary to sort out these discrepancies by conducting film cooling study over a row of circular holes at relatively high subsonic Mach number, which is essential for understanding the coolant behavior under transonic conditions.

In the present study, an experimental investigation was performed to examine the compressibility effect, mass flux ratio effect, and density ratio (*DR*) effect on effectiveness of film cooling by using the Pressure Sensitive Paint (PSP) and Particle Image Velocimetry (PIV) techniques, where the freestream Mach numbers (Ma) were 0.07, 0.30, 0.50 and 0.70, respectively. The PSP technique was used to map the detailed effectiveness distribution on the surface of interest based on a mass-flux analogy, in contrast to traditional temperature-based effectiveness measurements. A high-resolution PIV system was used to conduct detailed flow field measurements to correlate with the adiabatic effectiveness to reveal inherent physics in order to optimize design paradigms for improved effectiveness.

2. Experimental Setup and Test Model

2.1 Test facility and experimental model.

The experimental studies were conducted in a transonic, open-circuit wind tunnel located at the Department of Aerospace Engineering of Iowa State University, shown in Figure 1(a). The tunnel has an optically-transparent test section with 63.5 mm×25.4 mm cross section and is driven by three pressurized tanks, each with about 8 m^3 volume and 10 atmospheres of pressure at full capacity. A ceramic flow straightener with square 1 mm^2 cells is installed upstream of the contraction to create a uniform low-turbulence incoming flow. In order to monitor the temperature and pressure variation during the experiment, six pressure taps and two K-type thermocouples were placed along the test rig to acquire the instantaneous temperature and pressure data inside the test section and plenum. The density of gas and speed of sound were correlated by the measured pressures and temperatures, respectively. With the three tanks fully opened, Ma=0.70 flow can be achieved after a 20 s transient period and maintained stably (variation within 2.0%) for about 5 minutes, while each PSP test requires less than 3 minutes. A temperature drop of less than 5°C was recorded in the freestream flow over that time.

The circular-hole test plate, shown in Figure 1(b), is made of a hard plastic material and manufactured by a rapid prototyping 3D printer that builds the model layer by layer with a resolution of about 25 microns. The span-wise pitch is 3*D* on-center between adjacent holes and the entry length of hole is 5*D*, where *D*=2 mm is the hole diameter. The coolant was injected through a row of five circular holes at an injection angle 35° relative to the test plate surface. The test model was mounted on a plenum chamber and sealed by a thin latex runner gasket and silicon.

Figure 1(c) shows the schematic of the PSP experimental setup used in the present study. A constant UV light (LM2X-DM, ISSI) with wavelength of 390 nm was used as the excitation source for the PSP measurements. A 14-bit (2048 pixel × 2048 pixel) charge-coupled device (CCD) camera (PCO2000, Cooke Corp.) fitted with a 610 nm long-pass filter was used to records the intensity of the photoluminescence light emitted by excited PSP molecules. The PSP paint used in the study was Uni-FIB provided by ISSI. This type of paint has a low sensitivity to temperature variation (~0.5%/°C) making it an ideal candidate for the study. As mentioned above, the freestream temperature was found to drop less than 5°C, thus the measurement uncertainty caused by temperature variation was less than 2.5%.

In the present study, the mainstream flow from the wind tunnel was used to simulate the hot gas flow in typical turbine stage. The coolant jet flow, supplied by a pressurized gas cylinder (99.99% purity), passed through a long pipeline and heat exchanger to reach room temperature and finally enter the plenum chamber. All tests were conducted at constant temperature (22°C) with temperature fluctuation of less than 0.5°C. A 1.0 mm high obstruction was applied at the leading edge of test section (i.e., 28D upstream of coolant hole) to trip the mainstream flow and ensure a fully-developed turbulent boundary layer over the flat plate. The incoming flow boundary layer thickness (δ_{99}≈1.2D) of the 25 m/s case, upstream of coolant hole with coolant off, was found to be slightly larger than that of the Ma=0.3 case (δ_{99}≈1.0D). Meanwhile the momentum thicknesses of the two cases were found to be 0.09D and 0.08D, and the corresponding shape factors were 1.5 and 1.4 for Ma=0.07, 0.3, respectively.

During the experiment, N_2, CO_2, and a mixture of SF_6 and CO_2 were chosen to investigate the density ratio ($DR = \rho_c / \rho_\infty$) effects on film cooling effectiveness to simulate the temperature differences between the hot gas and coolant streams in the turbine stage of the engine. The corresponding density ratios were 0.97, 1.53, and 2.0, respectively. The Mach number of the mainstream flow was held at four pre-set numbers (0.07, 0.30, 0.50, and 0.70), accurately determined by the high-resolution PIV system. The mass flux ratios ($M = \rho_c V_c / \rho_\infty V_\infty$) was adjusted in the range of 0.40 to 1.25, and was monitored simultaneously by mass flow meters (Omega, FMA-1600A). Detailed information about test cases can be found in Table 1.

2.2 Adiabatic film cooling effectiveness measurement using the PSP technique.

Adiabatic film cooling effectiveness η is traditionally expressed as,

$$\eta = \frac{T_\infty - T_{aw}}{T_\infty - T_c} \ , \tag{1}$$

where T_∞ is the temperature of the main-stream, T_{aw} is the adiabatic wall temperature of the surface under inspection, and T_c is the hole exit temperature of the coolant stream.

In the present study, the effectiveness of film cooling was measured by using pressure sensitive paint (PSP) technique [13] rather than conducting temperature-based measurements on the surface of interest (such as using thermocouples, liquid crystal thermometry, infrared thermography, or temperature sensitive paint). The PSP technique is based on mass transfer analogy, which is free from heat conduction related errors encountered in non-isothermal experiments. The Lewis number ($Le = \frac{\alpha}{D_s}$, where α is

thermal diffusion coefficient, D_s is concentration diffusion coefficient) is approximate one at atmospheric condition, which means the thermal boundary layer and concentration boundary layer are of the same order, then the differential equations involving heat and mass transfer can be approximated as analogous[14–16]. As for transonic flow condition, the mass transfer analogy is still valid because the pressure (*P)* effect on the thermal diffusion coefficient $\alpha = \frac{\lambda}{\rho c_p} = \left(\frac{\lambda RT}{c_p}\right)\frac{1}{P}$ and concentration coefficient $D_s = D_{s,atm}\left(\frac{T}{T_{20°C}}\right)\frac{P_{atm}}{P}$ will be cancelled out in the Lewis number.

In order to perform the PSP experiments, the surface of interest was coated with an oxygen-sensitive layer of paint. This paint consists of luminophores molecules held binded within a gas-permeable polymeric binder. When excited by certain UV light, the luminophores molecules in PSP paint will emit light. However, the excited molecules may return to ground state via a reduced or radiationless emission in the presence of oxygen molecules. This process is called oxygen quenching [13], where the intensity of the photoluminescence is inversely proportional to the concentration of local oxygen. Consequently, the concentration of oxygen against the interested surface can be calculated by recorded light intensity through the using of calibration curve. Applying the concentrations of oxygen rather than the temperature into Eq. (1), the adiabatic cooling effectiveness can be expressed as Eq. (2), as described by Charbonnier *et al* [17], where *MW* is the ratio of molecular weights of the coolant gas to the freestream gas.

$$\eta = 1 - \frac{1}{\left[\left(\left(p_{o_2}\right)_{air} / \left(p_{o_2}\right)_{mix}\right)_{wall} - 1\right] MW + 1}, \tag{2}$$

the pressures in Eq. (2) can be computed using the recorded intensity of emission light, which is directly related to the partial pressure of oxygen. The mathematical function between normalized intensity and partial pressure can be obtained through a dedicated PSP calibration process. Detailed information on how to perform PSP calibration can be found in references [4, 18].

For the PSP image processing, in order to reduce the effects of camera noise on the measurements, spatial averaging was performed in the present study on square interrogation windows of 9×9 pixels with 50% overlap to ensure complete sampling of the measurement data. The acquired PSP images have a magnification of 0.055 mm/pix, which results in a spatial resolution of 0.2 mm for the PSP measurement results. The measurement uncertainty, taking account of the temperature effect within the test, for the centerline effectiveness in present study was estimated to be on the order of 4% for $\eta = 0.5$ and 6% for $\eta = 0.3$ (absolute uncertainty within $\Delta\eta$=0.03 throughout the entire interest). For laterally-averaged effectiveness, it was about 8% for $\eta = 0.3$ and 11% for $\eta = 0.2$ (absolute uncertainty within $\Delta\eta$=0.04). These estimations were predicted based on Taylor Series Method [19, 20]. Further measurement uncertainty analysis using the PSP technique can be found in Johnson and Hu [21].

2.3 Flow field measurements utilizing the PIV technique.

A high-resolution PIV system was used to conduct detailed flow field measurements to quantify the dynamic interaction and mixing processes between the coolant and mainstream flows over the test plate. During the experiment, the mainstream airflow and the coolants were seeded with ~0.5 μm oil droplets generated by a Six-Jet Atomizer (TSI,

Model 9306) and Atomizer Aerosol Generator (TOPAS, model ATM 210), respectively. The generated seedings were found to be able to reach 99% of the freestream velocity (i.e., Ma=0.70) in less than 0.60 μs after ~0.5 mm acceleration distance, estimated based on the method of Melling [22].

A Nd:YAG laser (NewWave Gemini 200) was utilized to emit two pulses of 200 mJ light at 532 nm wavelength with a repetition rate of 5 Hz. Using a set of high-energy mirrors and optical lenses, the laser beam was shaped into a thin light sheet with a thickness in the measurement interest of less than 1 mm. In order to reveal the interaction between the coolant flow and the mainstream flow, the illuminating laser sheet was aligned along the mainstream flow direction, bisecting the coolant hole in the middle of the test plate. A 14-bit digital camera (PCO2000) was used for the PIV acquisition with a field of view 7×15 mm^2 and a magnification of 0.014 mm/pix. The camera and laser were both connected to a Digital Delay Generator (Berkeley Nucleonics, Model 565), which controlled the time interval of the lasers (3.2 μs for Ma=0.07, 0.8 μs for Ma=0.3) and image acquisition process.

After PIV image acquisition, instantaneous PIV velocity vectors were obtained by using a frame-to-frame cross-correlation technique with an interrogation window size of 32×32 pixels. An effective overlap of 50% of the interrogation windows was employed in PIV image processing. After the instantaneous velocity vectors (u_i , v_i) are determined, the distributions of the ensemble-averaged quantities such as averaged velocity and normalized turbulence kinetic energy ($N.TKE = \frac{1}{2}\left(\overline{u'^2} + \overline{v'^2}\right) \Big/ U_\infty^2$) were obtained from a sequence of 1000 realizations of instantaneous PIV measurements. The measurement

uncertainty level for the velocity vectors is estimated to be within 3.0%, while the uncertainties for the measurements of ensemble-averaged flow quantities such as Reynolds stress and turbulent kinetic energy distributions are about 6.0%.

3. Results and Discussion

In the present study, the reliability of the PSP technique as an effective measurement tool for film cooling study had been examined through a series of comparisons in previous tests [4, 14, 23], where the measured results were consistent with the archived effectiveness that obtained from temperature-based measurements. Therefore, the PSP technique is a suitable method to study the effectiveness of film cooling in present study.

Figure 2 shows the comparison of film cooling effectiveness between the Ma=0.07 and Ma=0.70 cases at various mass flux ratios. In general, the spatial distributions of these cases were found to be similar in both pattern and footprint length. When M is relatively small (i.e., M=0.4), the coolant jet streams were found to remain attached on surface of near field, resulting in uniform and wide coverage of coolant film. Increasing M to 0.85 and 1.25 the spatial contours, however, were found to become narrower and shorter, which indicated that the high momentum coolant streams could separate from the plate.

More quantitative information of the effectiveness can be acquired through detailed comparisons of the centerline and laterally-averaged effectiveness between them, shown in Fig. 2(c) & 2(d). Noting that the laterally-averaged effectiveness is performed over a span-wise domain of $-4.5 < z/D < 4.5$, or three periods of hole spacing. It is obvious that the cooling effectiveness of Ma=0.70 at M=0.4 almost collapsed with the measurements of the low speed case within the whole field. Increasing M to 0.85 and 1.25, the

effectiveness of the Ma=0.70 cases were found to be slightly higher than that of the Ma=0.07 cases. This phenomenon was consistent with the spatial distribution of film cooling in that the shape of the high effectiveness region (red and white color) for the Ma=0.70 case was found to be sharper than that of the Ma=0.07 case. Since the mainstream velocity of the Ma=0.70 case was larger than the low speed case, the jet stream for the Ma=0.70 case would be suppressed more severely by the incoming flow in the near-hole field, leading to slightly enhanced effectiveness. Note that, though the momentum ratio is the same, the momentum difference between coolant and freestream becomes larger as the velocity increases.

Figure 3 shows the effect of density ratio on film cooling effectiveness with transonic mainstream condition (Ma=0.70), where the three density ratios (*DR*=0.97, 1.53, 2.00) were achieved by using N_2, CO_2, and mixture of SF_6 and CO_2, respectively. It is apparent that the effectiveness of various density coolants were found to be similar at *M*=0.40, indicating that the coolant remained attached on the surface. However, the cooling effectiveness was found to depend upon the density ratio as *M* increased to 0.85 (our results for the *M*=1.25 case were not shown here for conciseness) in that denser coolant resulted in increased effectiveness. At fixed *M*, the jet momentum is lower for a denser coolant ($I = M^2 / DR$), thus the coolant tends to stay closer to the surface than lighter coolants, resulting in enhanced effectiveness.

In order to obtain more quantitative information about the effects of compressibility on film effectiveness, a series of measurements were performed under a range of freestream Mach numbers, the results of which are shown in Fig. 4. Obviously, the mainstream Mach number was found to have limited effect on effectiveness of film

cooling at M=0.40, which demonstrates consistent cooling performance for test cases. But, as for M=0.85 and 1.25, the effectiveness for the Ma=0.30, 0.50 and 0.70 cases was found to be marginally higher than that of the baseline (Ma=0.07) case, largest differences within 15% for centerline effectiveness, 25% for laterally-averaged. The phenomenon is similar to what was discussed in Fig. 2. Careful inspection of the spatial distributions of these cases indicates that the film coverage was found to increase slightly as the Mach number increased, perhaps due to the 'Bernoulli's principle' that a jet tends to be attracted to a nearby object. If the gas diffusion is taken into account, the physical distance between coolant jets would be much smaller than the span-wise pitch (3D). Thus, the middle jet of the high speed cases would attract the adjacent streams to pull them down slightly and spread them more widely over the surface, leading to increased effectiveness. And the attraction force is proportional to the magnitude of relative velocity, which is the difference ($V_\infty - V_c$) between mainstream (V_∞) and coolant (V_c), namely, larger relative velocity indicating augmented force. Also increasing mainstream velocity and mass flux ratio, on the contrary, will decrease the growth rate of the shear layers within the freestream and coolant, forcing the impingement point farther downstream (Dellimore *et al*. [10]), therefore slightly enhancing the effectiveness of film cooling.

Though we know the effectiveness of high Mach number flow is slightly higher than that of low speed at M=0.85 and 1.25, the underlying flow physics pertinent to film cooling needs to be addressed. In order to gain more insight into the dynamic mixing between the coolant and mainstream flows, a high resolution PIV system was used to conduct detailed flow field measurements over the flat plates near the coolant jet region. Since the oil atomizer could only supply sufficient seed for flow with freestream Ma<0.30 in the present

study, the PIV experiments were performed at Ma=0.07 and 0.30. Figure 5 shows the comparison of PIV measurements between the Ma=0.07 and Ma=0.30 cases at *M*=0.40 and 1.25. Instantaneous velocity fields shown in Fig. 5 demonstrate an intensive fluid mixing within the jet and mainstream flow. Concentrating on the flow fields of *M*=0.40, the streamlines from both Ma=0.07 and 0.30 cases indicated that the coolant remained attached to the model surface, indicating good cooling performance for both cases, which is consistent with the PSP measurements. However, the phenomenon completely changed for *M*=1.25 in that the streamlines from both jets were found to separate from the surface and penetrate into the mainstream, resulting in poor cooling effectiveness. Though the mean velocity distributions of these two cases are similar, the predicted thickness of the coolant jet based on streamline distribution in the *x*–*z* plane for Ma=0.07 (~0.4D) is smaller than that of Ma=0.3 (~0.6*D*), manifesting that the coolant stream of the Ma=0.3 case remains slightly closer to the test plate in comparison to the low speed case. This effect can be used to understand why the effectiveness of higher Mach number cases are marginally higher than the baseline.

Figure 6 shows the comparison of area-averaged effectiveness as a function of Mach number at *M*=0.40, 0.85, and 1.25, which can be used to yield some insight into the effect of compressibility on film cooling effectiveness. The area-averaged effectiveness was computed by $\frac{\iint \eta_{xz}\, dA}{A}$, where *A* is the total area of interest (from *x/D*=1–20; *z/D*= -4.5*D*–4.5*D*), and η_{xz} is the effectiveness at the corresponding location. As shown clearly in Fig. 5, the area-averaged effectiveness is independent of the Mach number at *M*=0.40, exhibiting almost constant value. As for *M*=0.85 and 1.25, only marginal enhancement

(~13% for *M*=0.85, and ~15% for *M*=1.25) was observed at Ma=0.70 in comparison to the baseline Ma=0.07 cases. Therefore, it is acceptable to study the film cooling performance of transonic speed flow by performing experiments in a relatively low-speed wind tunnel when mass flux ratio is not particularly high.

4. Conclusion

In the present study, an experimental study was performed to measure the film cooling effectiveness of a row of cylindrical holes over a flat plate with mainstream Mach number at 0.07, 0.30, 0.50 and 0.70. The effects of mass flux ratio (*M*=0.40, 0.85, and 1.25), density ratio (*DR*=0.97, 1.53, and 2.0), and mainstream Mach number (Ma=0.07, 0.30, 0.50, and 0.70) on effectiveness of film cooling were examined in great detailed based on the quantitative PSP and PIV results.

It was found that, at *M*=0.40, the mainstream Mach number had limited effect on film cooling effectiveness, which was demonstrated by a similar effectiveness for all tests. This had been verified by the similar flow field from PIV measurements. Increasing *M* to 0.85 and 1.25, the measured effectiveness for the Ma=0.30, 0.50, and 0.70 cases were found to be marginally higher than those at Ma=0.07. Due to the Bernoulli's principle, the middle jet for the high speed cases was attracted by the adjacent streams to descend slightly and spread out more widely over the surface. Also the growth rate of the shear layers was decreased as the mainstream velocity and the mass flux ratio increased. Meanwhile the PIV measurements demonstrated that the coolant gas for the Ma=0.3 case at *M*=1.25 stayed slightly closer to the surface as compared to that of the Ma=0.07 case, which is consisted with the measured PSP results. In general, the difference of area-averaged

effectiveness were found to be within 15% between high speed and low speed cases. Therefore, when the mass flux ratio is not particularly high, it is acceptable to study the film cooling effectiveness of transonic speed flow by performing experiments in a relatively low-speed wind tunnel.

Reference

[1] Goldstein, R. J., Eckert, E. R. G., and Burggraf, F., 1974, "Effects of hole geometry and density on three-dimensional film cooling," Int. J. Heat Mass Transf., **17**(5), pp. 595–607.

[2] Baldauf, S., Schulz, A., and Wittig, S., 2001, "High-Resolution Measurements of Local Effectiveness From Discrete Hole Film Cooling," J. Turbomach., **123**(4), p. 758.

[3] Baldauf, S., Scheurlen, M., Schulz, A., and Wittig, S., 2002, "Correlation of Film-Cooling Effectiveness From Thermographic Measurements at Enginelike Conditions," J. Turbomach., **124**(4), p. 686.

[4] Johnson, B., Tian, W., Zhang, K., and Hu, H., 2014, "An experimental study of density ratio effects on the film cooling injection from discrete holes by using PIV and PSP techniques," Int. J. Heat Mass Transf., **76**, pp. 337–349.

[5] Bogard, D. G., 2006, "Airfoil film cooling," The Gas Turbine Handbook, National Energy Technology Laboratory, Section 4.2.2.1.

[6] Bogard, D. G., and Thole, K. A., 2006, "Gas Turbine Film Cooling," J. Propuls. Power, **22**(2), pp. 249–270.

[7] Bunker, R. S., 2005, "A Review of Shaped Hole Turbine Film-Cooling Technology," J. Heat Transfer, **127**(4), p. 441.

[8] Gritsch, M., Schulz, A., and Wittig, S., 1998, "Adiabatic Wall Effectiveness Measurements of Film-Cooling Holes With Expanded Exits," J. Turbomach., **120**(3), p. 549.

[9] Liess, C., 1975, "Experimental Investigation of Film Cooling With Ejection From a Row of Holes for the Application to Gas Turbine Blades," J. Eng. Power, **97**(1), p. 21.

[10] Dellimore, K. H., Marshall, A. W., and Cadou, C. P., 2010, "Influence of Compressibility on Film-Cooling Performance," J. Thermophys. HEAT Transf., **24**(3), pp. 506–515.

[11] Repukhov, V. M., 1970, "Effects of compressibility and nonisothermal conditions on the performance of film cooling," J. Eng. Phys. Thermophys., **19**(5), pp. 1401–1408.

[12] Parthasarathy, K., and Zakkay, V., 1970, "An experimental investigation of turbulent slot injection at Mach 6," AIAA J., **8**(7), pp. 1302–1307.

[13] Bell, J. H., Schairer, E. T., Hand, L. A., and Mehta, R. D., 2001, "SURFACE PRESSURE MEASUREMENTS USING LUMINESCENT COATINGS 1," Annu. Rev. Fluid Mech., **33**(1), pp. 155–206.

[14] Wright, L. M., Gao, Z., Varvel, T. A., and Han, J.-C., 2005, "Assessment of Steady State PSP, TSP, and IR Measurement Techniques for Flat Plate Film Cooling," Heat Transfer: Volume 3, ASME, pp. 37–46.

[15] Eckert, E. R. G., 1992, "Similarity analysis of model experiments for film cooling in gas turbines," Wärme- und Stoffübertragung, **27**(4), pp. 217–223.

[16] Shadid, J. N., and Eckert, E. R. G., 1991, "The Mass Transfer Analogy to Heat Transfer in Fluids With Temperature-Dependent Properties," J. Turbomach., **113**(1), p. 27.

[17] Charbonnier, D., Ott, P., Jonsson, M., Cottier, F., and Köbke, T., 2009, "Experimental and Numerical Study of the Thermal Performance of a Film Cooled Turbine Platform," Proc. Asme Turbo Expo 2009, Vol 3, Pts A B, pp. 1027–1038.

[18] Yang, Z., and Hu, H., 2011, "Study of Trailing-Edge Cooling Using Pressure Sensitive Paint Technique," J. Propuls. Power, **27**(3), pp. 700–709.

[19] Sajben, M., 1993, "Uncertainty estimates for pressure sensitive paint measurements," AIAA J., **31**(11), pp. 2105–2110.

[20] Coleman, H. W., and Steele, W. G., 2009, Experimentation, Validation, and Uncertainty Analysis for Engineers, John Wiley & Sons.

[21] Johnson, B. E., and Hu, H., 2014, "Measurement Uncertainties Analysis in the Determination of Adiabatic Film Cooling Effectiveness by Using Pressure Sensitive Paint (PSP) Technique," Volume 1D, Symposia: Transport Phenomena in Mixing; Turbulent Flows; Urban Fluid Mechanics; Fluid Dynamic Behavior of Complex Particles; Analysis of Elementary Processes in Dispersed Multiphase Flows; Multiphase Flow With Heat/Mass Transfer in Process Tec, ASME, p. V01DT40A001.

[22] Melling, A., 1997, "Tracer particles and seeding for particle image velocimetry," Meas. Sci. Technol.

[23] Zhou, W., and Hu, H., 2015, "An Experimental Study on Film Cooling Performance Behind Barchan Dune-Shaped Ramps Using PSP and PIV Techniques," Volume 5B: Heat Transfer, ASME, p. V05BT12A043.

Table 1. *Experimental cases of present study.*

Mach number of mainstream flow	*DR*	*M*	Mach number of coolant
0.07 (25m/s)	1.53	0.40, 0.85, 1.25	-
0.30	1.53	0.40, 0.85, 1.25	0.07–0.25
0.50	1.53	0.40, 0.85, 1.25	0.13–0.40
0.70	0.97	0.40, 0.85	0.29–0.61
	1.53	0.40, 0.85, 1.25	0.18–0.57
	2.00	0.40, 0.85	0.14–0.30

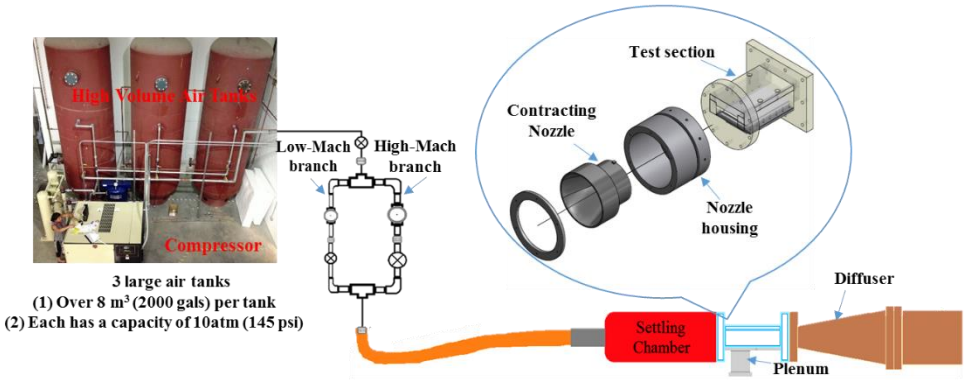

(a) Transonic flow wind tunnel

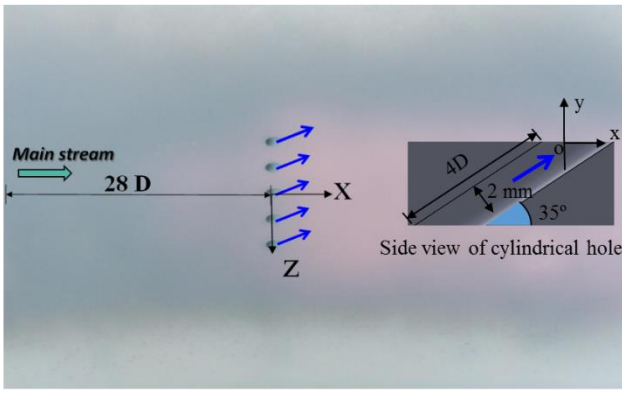

(b) Setup for PSP measurements

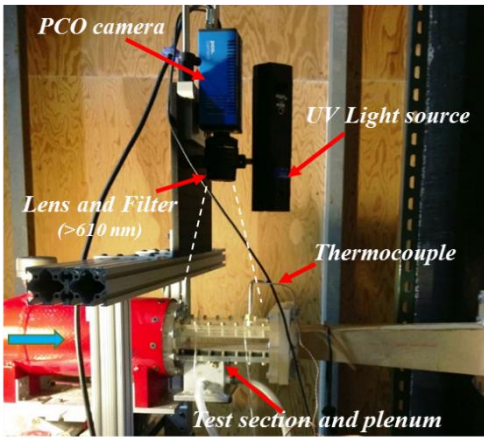

(c) cylindrical hole test model

Figure 1. *Schematic of the experimental rig for the present study.*

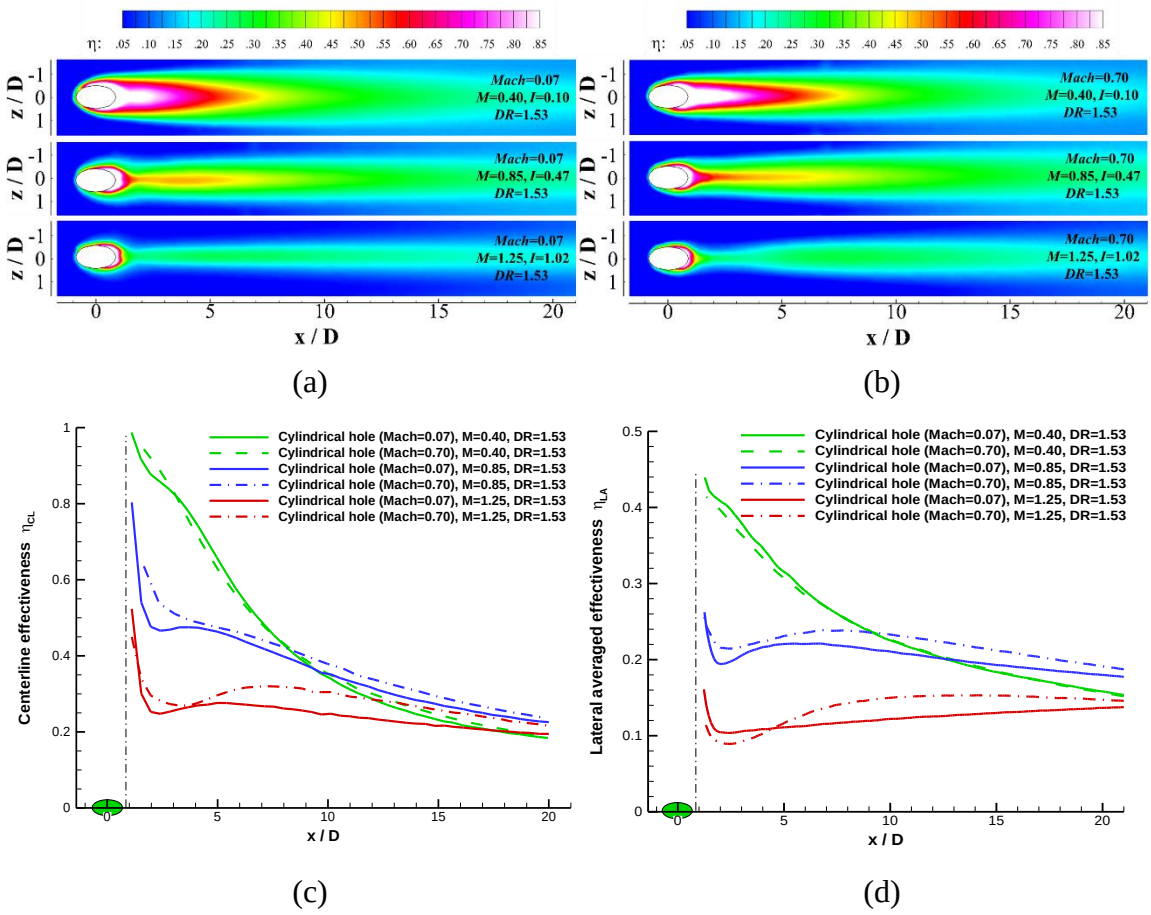

Figure 2. *Comparison of film cooling effectiveness between mainstream in Ma=0.07 and Ma=0.70 tests at M=0.40, 0.85, 1.25. (a) Spatial distribution at Ma=0.07, (b) Spatial distribution at Ma=0.70, (c) centerline effectiveness, (d) lateral-averaged effectiveness.*

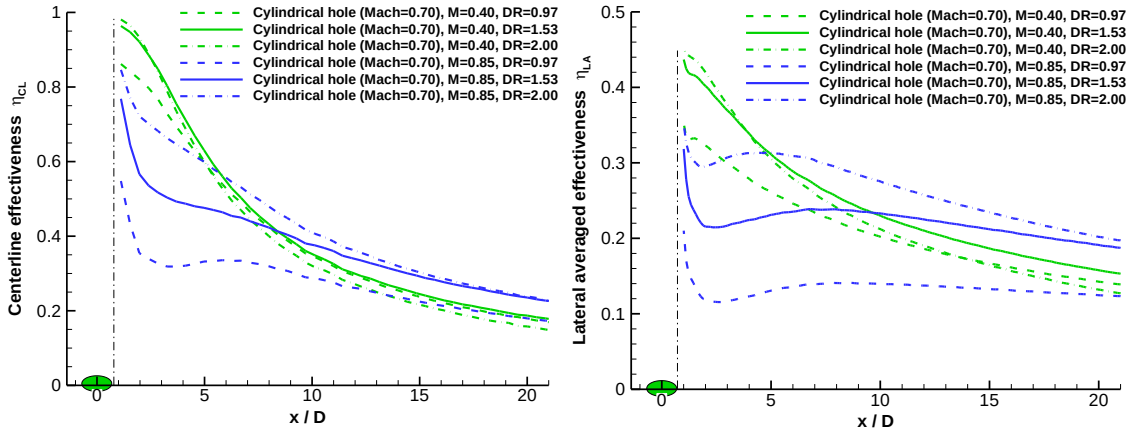

Figure 3. *Density ratio effect on film cooling effectiveness at Ma=0.70.*

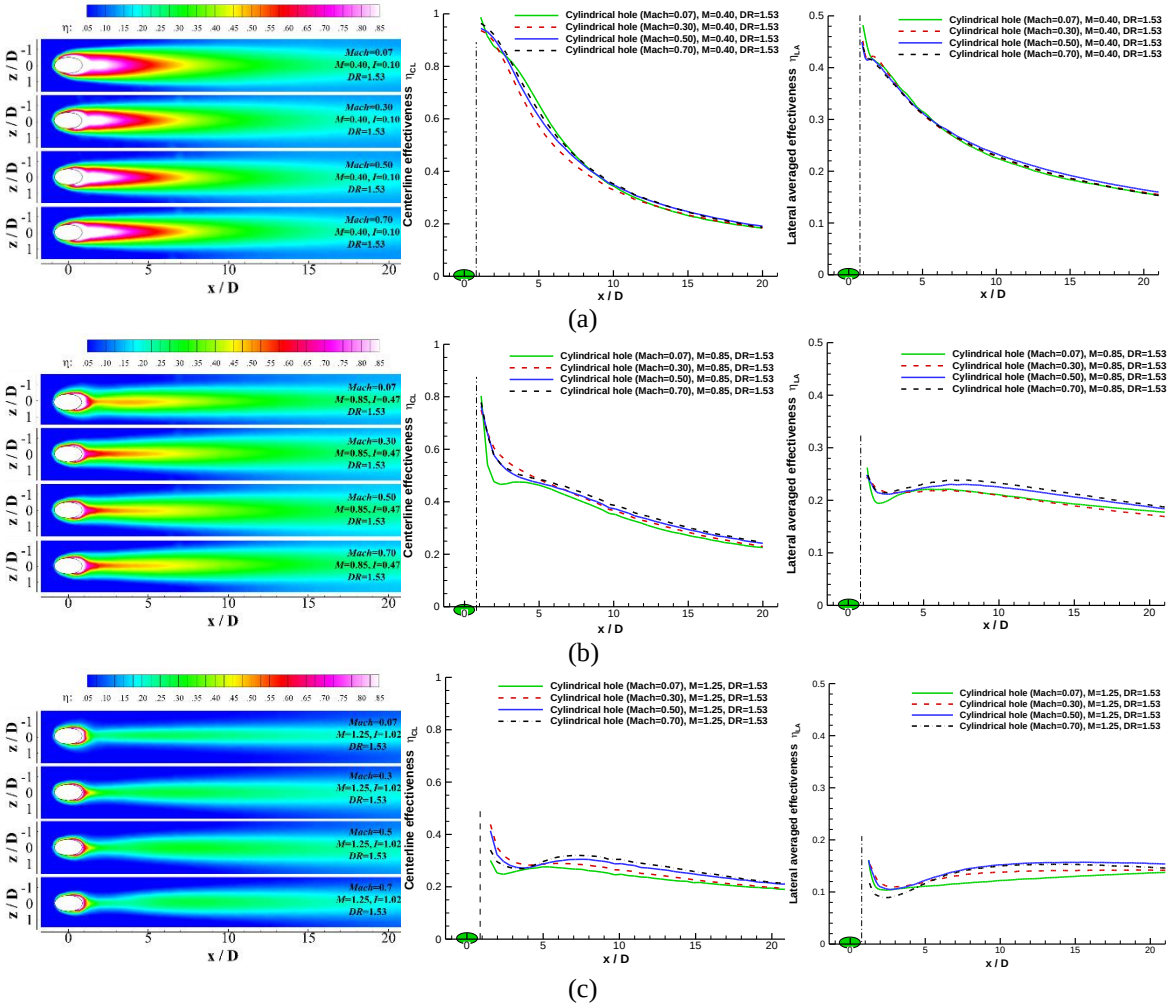

Figure 4. *Film cooling effectiveness as function of Mach number for M=0.40, 0.85, 1.25: (a) Film cooling effectiveness at M=0.40, (b) Film cooling effectiveness at M=0.85, (c) Film cooling effectiveness at M=1.25.*

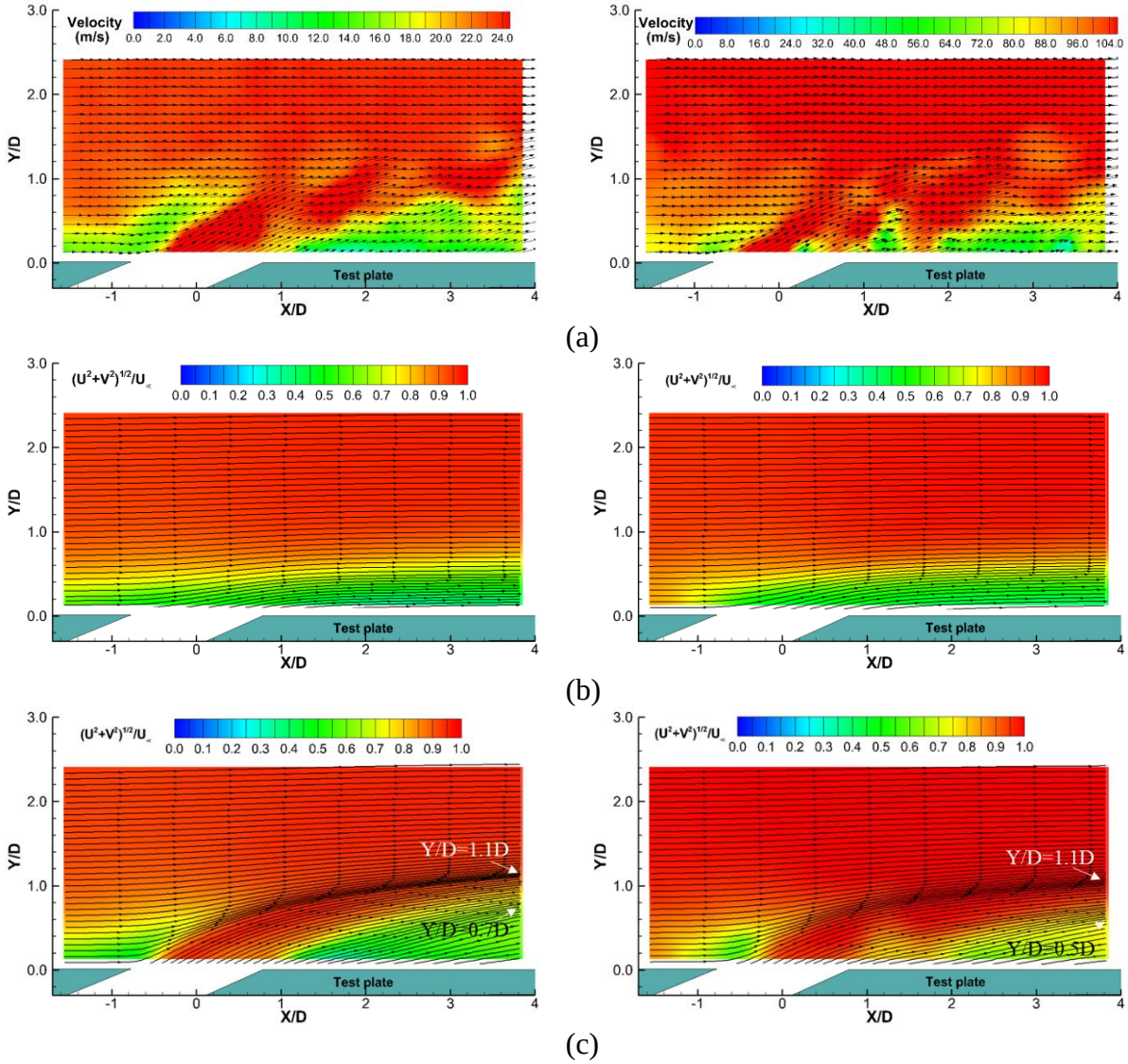

Figure 5. *Comparison of PIV measurement results between Ma=0.07 (left) and Ma=0.30 (right) cases at M=0.40 and 1.25: (a) Instantaneous velocity at M=1.25, (b) Ensemble-averaged velocity at M=0.40, (c) Ensemble-averaged velocity at M=1.25.*

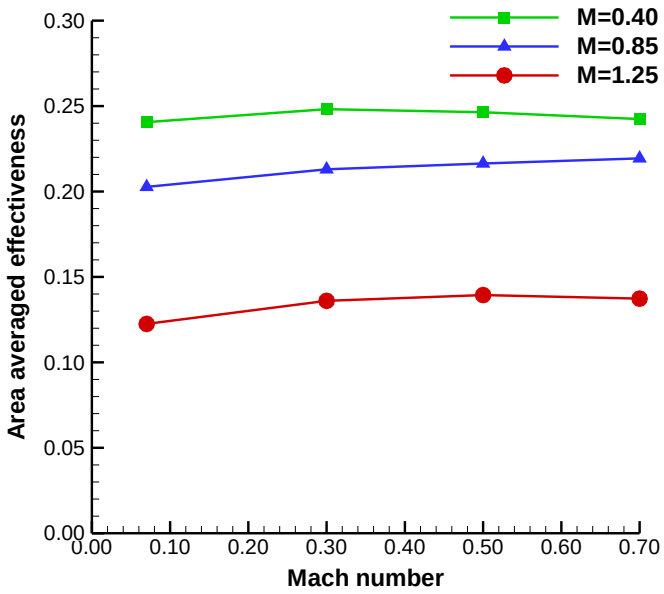

Figure 6. *The area-averaged film cooling effectiveness as function of Mach number at M=0.40, 0.85, 1.25.*

CHAPTER 5

AN EXPERIMENTAL INVESTIGATON ON THE CHARACTERISTICS OF TURBULENT BOUNDARY LAYER FLOWS OVER A DIMPLED SURFACE

Wenwu Zhou[1], Yu Rao[2] and Hui Hu[1] (✉)

[1] Department of Aerospace Engineering, Iowa State University, Ames, IA 50011, USA
[2] Gas Turbine Research Institute, School of Mechanical Engineering, Shanghai Jiao Tong University, Shanghai 200240, P.R. China.
✉ Corresponding authors. E-mail: huhui@iastate.edu

ABSTRACT

An experimental investigation was conducted to quantify the characteristics of the turbulent boundary layer flows over a dimpled surface in comparison to those over a conventional flat plate. In addition to measuring surface pressure distributions to determine the friction factors of the test plates and to map the surface pressure inside the dimple cavity, a high-resolution digital Particle Image Velocimetry (PIV) system was used to achieve detailed flow field measurements to quantify the characteristics of the turbulent boundary layer flows over the test plates and the evolution of the unsteady vortex structures inside the dimple cavity at the middle of the dimpled test plate. It was found that the friction factor of the dimpled plate would be about 30% ~ 80% higher than that of the flat plate, depending on the Reynolds number of the test cases. In comparison with those over a conventional flat surface, the flow characteristics of the turbulent boundary layer flows over the dimpled surface were found to be much more complicated with much stronger near-wall Reynolds stress and higher turbulence kinetic energy (TKE) levels, especially in the region near the back rims of the dimples. Many interesting flow features over the dimple surface, such as the separation of oncoming boundary layer flow from the

dimpled surface when passing over the dimple front rim, the formation and periodic shedding of unsteady Kelvin–Helmholtz vortices in the shear layer over the dimple, the impingement of the high-speed incoming flow onto the back rim of the dimple, and the subsequent generation of strong upwash flow in the boundary flow to promote the turbulent mixing over the dimpled surface, were revealed clearly and quantitatively from the PIV measurement results. The quantitative measurement results are believed to be the first of its nature, which depict a vivid picture about the unique flow features over dimpled surfaces and their correlations with the enhanced heat transfer performance reported in previous studies.

1. Introduction

Modern gas turbines operate at a peak turbine inlet temperature well beyond the maximum endurable temperature of the turbine blade material. As a result, hot gas-contacting turbine blades have to be cooled intensively by using various cooling techniques, such as internal convective cooling [1–20] and film cooling [21–24] on the blade exterior, in order to ensure a good structural integrity of the turbine blades. Dimple arrays, which can be placed throughout the entire internal cooling passage of turbine blades incorporating with other augmentation methods (such as impingement holes, rib turbulator, pin-fins), have become a magnet in forced convective heat transfer studies in recent years [1–19]. Due to its good heat transfer enhancement performance with comparatively smaller pressure loss penalties in comparison to other types of heat transfer augmentation devices such as pin-fins and rib tabulators, a dimpled surface (i.e., a flat

surface with dimple arrays) provides a desirable alternative for the internal cooling of turbine blades, especially in the rear regions of turbine blades.

A number of experimental and numerical studies have been conducted in recent years to investigate heat transfer augmentation performance of dimpled surfaces [3–7,9–13,15–19]. It is found that the heat transfer performance of a dimpled surface is greatly affected by the configuration of the dimples, including dimple diameter, dimple depth ratio, distribution pattern and shape of the dimples. Terekhov *et al*. [12] conducted an experimental study to measure the heat transfer coefficient and aerodynamic resistance of a dimpled surface, and found that the augmentation of heat transfer is much greater than that of flow resistance, leading to an overall increase in the rate of heat transfer process. Mahmood *et al*. [7] and Ligrani *et al*. [3,19] studied the local heat transfer and flow structures over dimpled surfaces experimentally with Reynolds numbers (based on channel height *H*) changing from 1,250 to 61,500, dimple depth ratio of 0.2, and channel height to dimple diameter ratio of 0.5. Based on qualitative flow visualization with smoke wires, Ligrani *et al*. [3,19] suggested that unsteady vortex structures shedding from dimples (including upwash flows and packets of vortices generated from the dimples) would enhance the turbulent mixing between the mainstream coolant flow and the hot flow inside the dimple cavity, therefore, leading to an augmentation of local *Nusselt* numbers over dimpled surfaces. Mahmood and Ligrani [15] conducted an experimental study to investigate the combined influences of channel height ratios (0.2, 0.25, 0.5 and 1.0), temperature ratios (0.78~0.94), Reynolds number (600~11,000) and flow structures on the heat transfer process over dimpled surfaces. They found that, as the channel height *H/D* decreases, both the shedding of unsteady vortex structures and local *Nusselt numbers*

become greater. Mitsudharmadi *et al*. [5] investigated the effects of round edged dimple arrays on the development of boundary layer flows over dimpled surfaces with depth ratios of 4%, 8% and 12%. Their measurements revealed that the flow separation observed for the test case with deeper edged dimples has similar flow structures as those of the cases with sharp dimple edge. Jordan *et al.* [6] conducetd detailed measurements of *Nusselt number* distributions over an array of V-shaped dimples using both transient liquid crystal and temperature sensitive pain technique. Their measurements results indicate that V-shaped dimples appear to enhance heat transfer augmentation with Reynolds number increasing, while marginal increase of pressure drop. As reported in Bunker *et al*. [17], dimple arrays were found to enhance heat transfer process not only in rectangular channels, but also in circular tubes was well. Based on the numerical simulation results with a large eddy simulation (LES) method, Turnow *et al*. [16] claimed that the fluctuations of streamwise velocity and the turbulent vortex structures are responsible for the augmentation of heat transfer over a dimpled surface. More recently, Xie *et al*. [4] conducted a numerical study to compare the surface heat transfer enhancement of six different shaped dimples, and found that the greatest heat transfer enhancement would be reached when the largest cross-section area of the dimple is oriented to be perpendicular to the incoming flow direction. Rao *et al.* [9] conducted an experimental and numerical study on teardrop shaped dimples and reported that teardrop shaped dimples exhibit the highest heat transfer ratio among all the tested shapes, which is about 18% higher than conventional spherical dimples.

While many significant findings have already been uncovered through those previous studies, most of the previous studies focused mainly on global features of the enhanced

heat transfer over dimpled surfaces, very few studies can be found in literature to provide detailed flow field measurements to quantify the unique characteristics of the boundary layer flows over dimpled surfaces and/or inside dimple cavities. While the unsteady vortex structures generated inside dimple cavities were suggested to play a very important role for the heat transfer augmentation over dimpled surfaces [3,7,19], most of the previous studies were conducted by using smoke wires to qualitatively visualize the unsteady vortex structures over dimpled surfaces or/and inside dimple cavities, no quantitative measurements have ever been available to characterize the evolution of the unsteady vortex structures over dimpled surfaces and/or inside dimple cavities. Such quantitative information is highly desirable to elucidate underlying physics for improved heat transfer performance of dimpled surfaces.

In the present study, an experimental investigation was conducted to quantify the characteristics of the turbulent boundary layer flows over a dimpled surface with staggered dimple arrays, in comparison to those over a conventional flat plate. The experimental study was conducted in a low speed, open-circuit wind tunnel with the Reynolds number (i.e., based on the hydraulic diameter of the dimpled channel and freestream velocity) in the range of Re=8,200 to 50,500, i.e., in the range of the Reynolds numbers for internal cooling channel of gas turbine blades. In addition to measuring surface pressure distributions to determine the friction factors of the test plates, a high-resolution digital Particle Image Velocimetry (PIV) system was utilized to achieve detailed flow field measurements to quantify the characteristics of turbulent boundary layer flows over the test plates and to reveal the evolution of the unsteady vortex structures inside the dimple cavity. The detailed flow field measurements were correlated with the surface pressure

measurement data to gain further insight into underlying physics to explore/optimize design paradigms for better internal cooling designs to protect turbine blades from the extremely harsh environments.

2. Test Models and Experimental Setup

2.1 Test models.

The experimental study was performed in a low speed, open-circuit wind tunnel located at the Department of Aerospace Engineering of Iowa State University. Similar as those used in previous studies[3,7,9,14,19], a rectangular channel with a small aspect ratio was designed to simulate the channel flow inside the internal cooling channel of gas turbine blades. The tunnel has an optically transparent test section of 20 mm×152 mm in cross section (H/W=0.132) with a corresponding hydraulic diameter (D_h) of 35.4mm (i.e., D_h=35.4mm). The airflow in the wind tunnel is driven by a centrifugal blower. A settling chamber with honeycomb, screen structures and a contraction section with an area ratio of 10:1 are installed at the upstream of the test section in order to provide uniform low turbulent incoming flow into the test section. The turbulence intensity level of the airflow in the test section of the wind tunnel was found to be about 1.0 %, as measured by hotwire anemometer. In the present study, two-inch-wide 64 grit sand papers were employed on both the top and bottom surfaces of the inlet duct (i.e., 14 D_h distance upstream of the test plate) in order to trip the oncoming boundary layer flow at the entrance of the test plate to ensure a fully developed turbulent boundary layer flow over the test plate.

Figure 1 shows the schematic of a dimpled test plate along with a conventional flat plate as the comparison baseline used in the present study. As shown in Fig. 1, the two

test plates are designed to have the same dimension, i.e., 275 mm in length, 170 mm in width and 12.7 mm in thickness. The test plates are made of hard plastic and manufactured by using a rapid prototyping machine. For the dimpled test plate, an array of spherical dimples with the same diameter of 20 mm and sharp edges (i.e., D=20 mm and spherical diameter of 29 mm) are distributed uniformly on the test plate in a staggered pattern. The distances between the adjacent dimples in both streamwise and spanwise directions are the same, i.e., P = 25 mm. The depth of the dimples is set to be h=4 mm with the corresponding depth ratio of h/D=0.2. It should be noted that the depth of the dimple is relatively large to the channel height, 20 mm. Considering fluid with 25% of local cross sectional change in the main flow direction, the flow inside dimple cavity could be regarded as pulsatile internal flow along the main stream, rather than the effect on single-surface boundary layer. During the experiments, the dimpled test plate was flush mounted onto the bottom plate of the test section to form a narrow test channel. The arrangement of dimple arrays over the dimpled test plate used in the present study is very similar as that used in Mahmood and Ligrani [15].

A total amount of 45 pressure taps with 0.5mm in diameter for each taps were arranged over the dimpled test plate in order to map the surface pressure distributions on the test plate. While 21 pressure taps were distributed uniformly inside the dimple at the center of the test plate, 5 pressure taps in each group were located at the leading and trailing edges of test plate, and the rest of the 14 pressure taps were arranged along the centerline of test plate. The pressure taps were connected to three units of digital sensor arrays (DSA3217, Scanivalve Corp, 16 channels for each unit) by using tygon tubing with 1.5 mm diameter and 0.5 m length for the pressure data acquisition. The DSA3217 system

incorporates temperature-compensated piezo-resistive pressure sensors with a pneumatic calibration valve, RAM, 16 bit A/D converter, and a microprocessor in a compact self-contained module. The precision of the pressure acquisition system is ±0.05 % of the ±10 inch H_2O full scale range. During the experiments, the instantaneous surface pressure measurement data for each pressure tap were acquired at a data acquisition rate of 300 Hz for 100 seconds.

It should be noted that, since Reynolds number based on either channel height or hydraulic diameter of the rectangular test channel has been widely used in the previous studies to investigate the flow characteristics and heat transfer performance of internal cooling designs of gas turbine blades, same definition of Reynolds number is also used in the present study in order to correlate the measurement results of the present study to those of the previous studies[3,7,9,10,14,15,19,25]. During the experiments, the bulk velocity of the rectangular test section was set to change from $\bar{U}$ = 4 m/s to 22 m/s, and the corresponding Reynolds number based on the hydraulic diameter (D_h) of the rectangular channel varies from *Re*=8,200 to 50,500, which is in the range of the typical Reynolds numbers of the channel flows to study internal cooling of gas turbine blades [9,15]. The Reynolds number levels of the test cases based on the dimple diameter (*D*) and the channel height (*H*) are also listed in Table 1 for comparison.

2.2 Experimental setup for PIV measurements.

Figure 2 shows the schematic of the experimental setup used for PIV measurements. The incoming airflow was seeded with ~1 μm oil droplets generated by a fog seeding machine. Illumination was provided by a double-pulsed Nd:YAG laser (NewWave

Gemini PIV 200) adjusted on the second harmonic and emitting two laser pulses of 200 mJ at the wavelength of 532 nm with a repetition rate of 5 Hz. The laser beam was shaped to a thin sheet by a set of mirrors, spherical, and cylindrical lenses. The thickness of the laser sheet in the measurement region was set to be about 0.8 mm. During the experiments, the illuminating laser sheet was first aligned vertically along the incoming flow direction (i.e., in the *X*-*Y* plane as shown in Fig. 2) passing the symmetric plane of the dimpled test plate, which were used to determine the ensemble-averaged velocity field, Reynolds stress and in-plane Turbulence Kinetic Energy (TKE) distributions of the boundary layer flow over the dimpled surface in the *X*-*Y* plane. Then, the illuminating laser sheet was rotated 90° for the PIV measurements in the *X*-*Z* plane at about 1.5mm above the dimpled test plate. A high-resolution 14-bit (2048 pixels × 2048 pixels) CCD camera (PCO2000, Cooke Corp) with its view axis normal to the illuminating laser sheet (i.e., for both of the test cases with the laser sheet in *X*-*Y* plane and *X*-*Z* plane) was used for PIV image recording, which has a field of view 45 × 25 mm^2 and a magnification of 0.025 mm/pix. The CCD camera and the double-pulsed Nd:YAG lasers were connected to a workstation (host computer) via a Digital Delay Generator (Berkeley Nucleonics, Model 565), which controlled the time interval of the laser illumination and the image acquisition.

In the present study, PIV measurements were also conducted with the CCD camera tilted at an angle of ~ 30° with respect to the vertically aligned illuminating laser sheet (i.e., *X*-*Y* plane) passing the symmetric plane of the dimpled test plate, as shown in Fig. 2, in order to quantify the turbulent flow and unsteady vortex structures inside the dimple cavity. A tilt-axis mount was installed between the lens and the camera body to satisfy the Scheimpflug condition to ensure that the tracer particles in the laser sheet (i.e., objective

plane) being focused on the image planes. Since the image plane of the CCD camera is tilted with respect to the objective plane for such a setting, the magnification factors between the image plane and the object plane are variable due to the perspective distortion. An *in-situ* calibration procedure as suggested by Soloff *et al*. [26] was conducted in the present study to obtain the quantitative mapping functions between the image plane and the object plane for the PIV measurements to reveal unsteady vortex structures inside the dimple cavity. It should also be noted that, in order to alleviate the contaminations of the strong laser reflection from the surfaces of the test plates to the acquired PIV raw images, the test plates were coated with a layer of Rhodamine 6G dye. Meanwhile, a 532 nm band pass filter was mounted in front of the optical lens of the CCD camera to filter out the laser-induced fluorescence from the Rhodamine 6G coated surfaces. Since the adhesion of tiny oil droplets (i.e., PIV tracers) onto the channel walls during the experiments may affect PIV measurements, the test plate was removed from the test rig for a thorough clean after each test run in order to minimize the effects of the oil droplet deposition on the PIV measurements.

After PIV image acquisition, instantaneous velocity vectors were obtained by frame to frame cross-correlation of particle images, using an interrogation window of 32 pixels × 32 pixels. An effective overlap of 50% of the interrogation windows was employed in PIV image processing, which results in a spatial resolution of 0.4 mm for the PIV measurements. After the instantaneous velocity vectors (u_i v_i) were determined, the distributions of the ensemble-averaged flow quantities such as averaged velocity, normalized Reynolds Shear Stress ($\tilde{\tau} = -\overline{u'v'}/\bar{U}^2$), and normalized in-plane turbulence

kinetic energy (i.e., $0.5(\overline{u'^2}+\overline{v'^2})/\bar{U}^2$ in X-Y plane or $0.5(\overline{u'^2}+\overline{w'^2})/\bar{U}^2$ in X-Z plane) were obtained from a sequence of about 1,000 frames of instantaneous PIV measurements, where $\bar{U}$ is the spatial averaged velocity of cross section (bulk velocity). The measurement uncertainty level for the instantaneous velocity vectors is estimated to be within 3.0%, while the uncertainties for the measurements of the ensemble-averaged flow quantities are estimated to be within 7.0%.

3. Results and Discussion

3.1 Characteristics of the oncoming boundary layer flow.

As described above, sand papers were employed on both the top and bottom surfaces of the inlet duct to trip the boundary layer flows over the top and bottom surfaces. Since the tripped boundary layer flows over both the top and bottom surfaces would develop and eventually merge at the center of test channel, the thickness (δ) of the boundary layer flows would be 0.5*H* (i.e., δ=10 mm) after becoming fully developed [12, 26]. In the present study, the characteristics of the oncoming boundary layer flow at the entrance of the test plate were measured by using the digital PIV system at three different test conditions (*Re*=8.2K, 36.7K and 50.5K). Figure 3 shows the measured velocity profiles of the oncoming boundary layer flow at the entrance of the test plate. It can be seen clearly that, except for the test case of *Re*=8.2K, the velocity profiles of the oncoming boundary layer flow are found to follow a 1/7th power law well, i.e., $U/U_0=(Y/\delta)^{1/7}$, where U_0 is the velocity at *Y=0.5H* height. It indicates a fully-developed turbulence boundary layer flow over the test plate. While the momentum thicknesses of the turbulent boundary layer flow

was found to be 0.099δ and 0.083δ, the corresponding shape factor (H^*) is 1.31 and 1.32 for the test cases of Re=36.7K and Re=50.5K, respectively. As for the test case of *Re*=8.2K, the momentum thickness of the boundary layer flow was found to be 0.114δ and shape factor of 1.54.

According to the logarithmic law ($U^+ = (1/\kappa) ln\, y^+ + A$, where $\kappa = 0.41$ and A=5.2) of the velocity profiles for a fully developed turbulent channel flow [28] , the friction velocity (u_*) and local wall shear stress (τ_w) were also estimated based on the measured flow velocity profiles ($30 \le y^+$, $y \le 0.3\delta$) at the entrance of the test plate, and the results are listed in Table 2.

3.2 Friction factor measurement results.

In the present study, the friction factors of the channel flows over the test plates were determined based on the measured surface pressure distributions on the test plates. For a fully-developed turbulent channel flow, the friction factor of a test plate can be calculated by using following equation [29–31]:

$$f = \frac{D_h \Delta p}{2L\rho \bar{U}^2} \tag{1}$$

Where D_h is the hydraulic diameter of the test section (i.e., D_h =35.4mm for the present study); Δp is the pressure loss along the dimpled test plate; L is the distance between the two rows of the pressure taps at the inlet and outlet of the dimpled test plate (i.e., L=220 mm); ρ is the density of air flow; $\bar{U}$ is the bulk velocity of the test section. Figure 4 gives the measured friction factors of the dimpled test plate in comparison with those of the flat test plate.

The applicability of Equation (1) to estimate the friction factor of a fully-developed turbulent channel flow was validated by quantitatively comparing the measured friction factors of the flat test plate with those predicted by using an empirical formula suggested by Dean [32] (i.e., $f = 0.073Re^{-0.25}, Re = \rho \bar{U} D_h / \mu$). As shown in Fig. 4, it is obvious that the measured friction factor of the flat test plate (solid circular marks) agree very well with those predicted by using the empirical formula suggested by Dean [32] within the entire Reynolds number range of the present study (i.e., 10,000< *Re* <60,000). It confirms the applicability of Equation (1) to estimate the friction factor of fully-developed turbulent channel flow over the flat test plate.

As clearly shown in Fig. 4, as the Reynolds number increases, while the friction factor of the flat test plate would decrease gradually, the friction factor of the dimpled surface (solid square marks) was found to increase rapidly at first, reaching the peak value at *Re* ≈33,000, then decrease slightly with the increasing Reynolds number until *Re* ≈40,000. The friction factor of the dimpled surface was found to become almost constant as the Reynolds number being greater than 41,000 (i.e., *Re* >41,000). In compared with those of the flat test plate, the friction factor of the dimpled surface was found to be about 30% ~ 80% greater at the same Reynolds number levels. Similar conclusions were also reported in the previous study of Han *et al.* [2]. The higher friction factor of the dimpled surface as shown in Fig. 4 is believed to be closely related to the more complicated turbulent flow structures induced by the dimple arrays, which will be discussed in the later sections of the present study.

3.3 Surface pressure distributions inside the dimple cavity.

As shown schematically in Fig. 2, 21 pressure taps are arranged inside the dimple at the center of the test plate in order to map the surface pressure coefficient ($C_p = (P - P_1) \Big/ \frac{1}{2}\rho \bar{U}^2$) inside the dimple cavity at different test conditions, where P_1 is the static pressure of the incoming flow measured at the inlet of the test plate. Figure 5 shows the measured surface pressure coefficient distributions inside the dimple cavity at the test conditions of *Re*=8.2K, 36.7K and 50.5K, respectively.

As shown clearly in Fig. 5, the distribution pattern of the surface pressure coefficients inside the dimple cavity was found to be quite similar in general at different Reynolds number levels. While the surface pressure was found to be relatively low (i.e., the region in blue color) in the region near the front rim of the dimple, a region with much high surface pressure (i.e., the region in red color) exists near the back rim of the dimple. Such a distribution pattern was found to be closely related to the unique flow characteristics inside the dimple cavity, i.e., the incoming mainstream flow would separate from the dimpled surface when passing over the front rim of the dimple, which leads to the formation of a recirculation region with relatively low surface pressure at the front portion of the dimple cavity. The low pressure at the front portion of the dimple would cause the mainstream flow to shift downward slightly and impinge onto the back rim of the dimple, resulting in a high pressure region near the back rim of the dimple.

While the global features of the surface pressure distribution pattern inside the dimple cavity were found to be quite similar for the three test cases, some differences still can be identified from the comparison of the surface pressure distributions given in Fig. 5. The

size of the region with relatively low surface pressure at the front of the dimple cavity was found to become greater as the Reynolds number increases, which is believed to be closely related to the stronger recirculating flow at the front of the dimple cavity for the cases with higher Reynolds numbers.

Figure 6 shows the transverse profiles of the surface pressure coefficients along the centerline of the dimple for the three test cases, which reveals the variations of the surface pressure inside the dimples cavity more clearly and quantitatively. As shown in the plot, the surface pressure inside the dimple cavity was found to decrease slightly at the front of the dimple (i.e., within the recirculation region as revealed from the PIV measurement results to be discussed later), then increase rapidly at the rear portion of the dimple cavity, and reach their peak values at the back rim of the dimple. As described above, while the general trend of the surface pressure profiles at different Reynolds number levels was found to be almost the same, the slightly earlier increase of the surface pressure inside the dimple cavity can be observed for the case with the lowest Reynolds number (i.e., *Re*=8.2K case).

3.4 PIV measurements to quantify the flow characteristics over the dimpled surface.

As described above, a high-resolution PIV system was used in the present study to conduct detailed flow field measurements to quantify the characteristics of the turbulent boundary layer flow over the dimpled test plate in comparison with those over the flat plate. The PIV measurements were conducted in the vertical plane passing the center of the dimple in the middle of the dimpled test plate, i.e., in the *X*-*Y* plane shown in Fig. 2. Figure 7 shows the typical PIV measurement results over the dimpled surface in the terms

of instantaneous velocity field, the instantaneous vorticity distribution, the ensemble-averaged flow velocity field and "*in-plane*" TKE of $0.5(\overline{u'^2}+\overline{v'^2})/\bar{U}^2$ for the test case of *Re* =50.5K. The PIV measurement results of the turbulent boundary layer flow over the flat surface were also given in the figure as the comparison baseline. It should be noted that PIV measurements were also conducted for the other test cases with *Re* = 8.2K and 36.7K. Since very similar flow features were seen for the other test cases, only the PIV measurement results for the test case of *Re* = 50.5K are shown here for conciseness.

As shown clearly and quantitatively in the instantaneous velocity and vorticity distributions given in Fig. 7, the vortex structures in the boundary layer flow over the dimpled surface were found to become much more complex in compared with those over the flat surface. While only very few vortex structures were identified in the boundary layer flow over the flat test plate, a series of unsteady vortex structures were found to be generated and shed periodically from both the front and back rims of the dimple as the incoming mainstream flow passing over the dimple. After shedding from the front and back rims of the dimple, the unsteady vortex structures were found to break down into smaller vortices as they moving downstream. As a result, the turbulent boundary layer flow over the dimpled surface was found to be filled with various vortex structures with different size and orientations. The instantaneous PIV measurement result also reveals clearly that a strong upwash flow was generated near the back rim of the dimple, which would greatly enhance the turbulent mixing between the low-momentum flow near the wall and the high-momentum freestream flow further away from the wall. As a result, the heat transfer process between the hot flow near the wall and the mainstream coolant flow would be augmented due to the existence of the dimple arrays over the dimpled plate. The

upwash flow generated at the back rim of the dimple and the enhanced turbulent mixing in the boundary layer flow over the dimpled surface can also be seen clearly in the ensemble-averaged velocity field and the in-plane TKE distributions given in Fig. 7.

Based on qualitative visualization with smoke wire, Ligrani *et al.* [3,19] conducted a series of experimental studies to examine the relationship between the enhanced local heat transfer and the characteristics of the flow structures over dimpled surfaces. They suggested that the vortex structures shedding from the dimples (including large upwash regions and packets of vortices generated from the dimples) would enhance the turbulence mixing between the mainstream coolant flow and the hot flow inside the dimples, therefore, leading to an augmentation of local heat transfer near the rims of dimples. The existence of the strong upwash flow and packets of unsteady vortex structures over the dimpled surface revealed quantitatively from the PIV measurements described above was found to be in good agreement with the qualitative smoke wire visualization results reported in Ligrani *et al.* [3,19]. While TKE level is usually used as an index to evaluate the extent of the fluid mixing in a turbulent flow, as shown quantitatively in the in-plane TKE distributions given in Fig. 7, the appearance of a region with high *in-plane TKE* levels near the back rim of the dimple illustrates a strong correlation between the enhanced turbulent mixing in the boundary layer flow over the dimpled surface with the improved local heat transfer in the region near the back rim of the dimple reported in Ligrani *et al.* [3,19], which will be addressed in further detail in the later section of the present study.

While the PIV measurement results given in Fig. 7 reveal the significant differences in the characteristics of the turbulent boundary layer flows over the dimpled surface, in comparison with those over a conventional flat surface, it is highly desirable to conduct

quantitative measurements to examine the flow features inside the dimple cavity in order to gain a more intuitive insight into the underlying physics. As described above, by tilting the camera for PIV image acquisition with an angle of 30° to the vertically aligned laser sheet along the middle plane of the dimpled test plate (i.e., *X*-*Y* plane as shown in Fig. 2), the flow field inside the dimple was also measured in the present study by using the high-resolution PIV system. Figure 8 to Fig. 10 give the typical PIV measurement results to reveal the flow characteristics inside the dimple cavity for the test cases with *Re* = 8.2K, 36.7K and 50.5K, respectively.

As revealed clearly in the PIV measurement results, the flow features inside the dimple cavity were found to be actually quite complicated. While the flow velocity inside the dimple was found to be relatively small in general as expected, a large recirculating flow was found to form inside the dimple. The high-speed incoming mainstream flow was found to separate from the wall surface when passing over the front rim of the dimple. Due to the Kelvin-Helmholtz instabilities [25] in the shear layer between the high-speed mainstream flow and the low-speed recirculating flow inside the dimple cavity, unsteady vortex structures were found to be generated and shed periodically along the interface between the two flow streams. It should be noted that Tollmien-Schlichting (T-S) instability may also contribute to the generation of unsteady vortices structures in the boundary layer flow over the dimpled surface.

The generation and periodic shedding of the unsteady Kelvin-Helmholtz vortices would cause intensive turbulent mixing in the boundary layer flow over the dimple not only by promoting the entrainment of high-speed mainstream flow from outside into the near-wall region, but also boosting the ejection of the low-speed recirculating flow out of

the dimple cavity. As a result, the heat transfer process between the high-speed coolant flow and the near-wall hot flow over the dimpled surface is greatly enhanced, as reported in Ligrani *et al.* [3,19].

The PIV measurement results also reveal clearly that, due to the existence of the low pressure at the front of the dimple cavity as shown clearly in Fig. 5, the high-speed mainstream flow would shift downward slightly and impinge onto the back rim of the dimple, creating a strong upwash flow near the back rim of the dimple. As described above, the impingement of the high-speed mainstream flow onto the back rim of the dimple would result in a high pressure region over the back portion of the dimple cavity, which is also revealed clearly and quantitatively from the surface pressure distributions given in Fig. 5. As shown clearly in the normalized in-plane TKE and Reynolds stress distributions given in Figs. 8 to 10, the regions with high TKE and Reynolds stress values were found to concentrate mainly in the shear layer between the high-speed mainstream flow and the low-speed recirculating flow inside the dimple cavity, which is correlated well with the shedding path of the unsteady Kelvin-Helmholtz vortices described above. Corresponding to the formation of the strong upwash flow near the back rim of the dimple, the TKE and Reynolds stress values were found to increase significantly in region near the back rim of the dimple.

While the global features of the flow characteristics inside the dimple were found to be quite similar in general for the test cases with different Reynolds number levels, some differences still can be identified by carefully inspecting the PIV measurement results for the three compared cases. As shown in the ensemble-averaged velocity fields and the corresponding streamline distributions, while the center of the recirculation zone inside

the dimple cavity was found to move further forward to the front rim of the dimple, the recirculating flow inside the dimple would much become stronger, as the Reynolds number increases. This explains the larger size of the region with relative low surface pressure at the front portion of the dimple for the cases with higher Reynolds numbers, as shown in Fig. 5. It can also be seen that, the upwash flow near the back rim of the dimple would become much stronger as the Reynold number increases, which results in higher normalized in-plane TKE and Reynolds stress levels in the boundary layer flow over the dimpled surface.

Figure 11 shows a schematic sketch of the flow features over a dimple, which vividly illustrates the unique flow characteristics and evaluation of the unsteady vortex structures revealed from the measured surface pressure distributions and PIV measurement results given above. As shown in the diagram, the incoming high-speed mainstream flow would separate from the dimpled surface when passing over the front rim of the dimple, which leads to the formation of a strong shear layer between the high-speed mainstream flow and the low-speed recirculating flow inside the dimple cavity. The separated boundary layer flow over the dimple would behave more like a free shear layer which is highly unstable, therefore, rolling up of unsteady vortex structures due to the Kelvin–Helmholtz instabilities would be readily realized. As shown schematically in Fig. 11, the unsteady Kelvin–Helmholtz vortices will not only promote the entrainment of high-speed mainstream flow from outside into the near-wall region, but also booster the ejection of the low-speed recirculating flow out of the dimple cavity. The ejection of the low-speed recirculating flow inside the dimple cavity into the high-speed mainstream flow will result in the formation of so-called “mushroom vortex” structures as described in Mahmood *et*

al.[7]. The existence of the low pressure region at the front portion of the dimple, which is correlated to the formation of the low-speed recirculating flow inside the dimple cavity, will cause the high-speed mainstream flow to shift downward slightly and impinge onto the back rim of the dimple. After the impingement, the flow would split into two streams with one stream recirculating inside the dimple cavity and the other ejected out of the dimple cavity as a strong upwash flow. With such a process, the dimple acts as a 'turbulator' to generate various unsteady vortex structures and strong upwash flow in the boundary layer flow over the dimpled surface to promote the turbulent mixing between the high-speed coolant flow and the hot low-speed flow inside the dimple cavity. This is believed to be the primary reason why a dimpled surface can have a good heat transfer enhancement performance with comparatively smaller pressure loss penalties, in comparison to other types of heat transfer augmentation devices such as pin-fins and rib turbulators used for the internal cooling of turbine blades.

It should also be noted that, while Mahmood *et al.* [7,15] and Ligrani *et al.* [3,19] conducted a series of experimentally studies to investigate the unsteady vortex and turbulent flow structures on and above dimple arrays as well as their correlations to the enhanced heat transfer performance of dimpled surfaces, most of the research findings were derived based on qualitative flow visualization images obtained with a smoke wire method to visualize flow features on and above dimpled surfaces, very limited quantitative information about the flow characteristics and unsteady vortex structures has ever been reported in previous studies. The quantitative measurement results given in the present study are believed to be the first of its nature to quantify the unique flow characteristics and evolution of the unsteady vortex structures inside the dimple cavity and the enhanced

turbulent mixing in the boundary layer flow over the dimpled surface. The formation and shedding of the unsteady Kelvin–Helmholtz vortices, the impingement of the high-speed mainstream flow onto the dimple back rim, and the subsequent generation of strong upwash flow to promote the turbulent mixing over the dimpled surface were revealed clearly and quantitatively from the PIV measurement results given above. In comparison with the qualitative flow visualization images reported in Mahmood *et al.* [7,15] and Ligrani *et al.* [3,19], the quantitative flow field measurement results given in the present study depict a much more vivid picture about the unique flow characteristics and evolution of the unsteady vortex structures on and above dimpled surface, which is highly desirable to elucidate underlying physics to gain further insight into underlying physics and to explore/optimize design paradigms for better internal cooling designs to protect turbine blades from the extremely harsh environments.

In the present study, PIV measurements were also conducted in a horizontal plane parallel to the dimpled test plate, i.e., in the *X*-*Z* plane as shown in Fig. 2. For the PIV measurements in the horizontal plane, the laser sheet was set to be about 1.5 mm away from the upper surface of the dimpled test plate (i.e., $Y/D \approx 0.08$) in order to minimize the strong reflection of the illuminating laser sheet from the upper surface of the test plate. Figure 12 shows typical PIV measurement results in the terms of the normalized in-plane *TKE* distribution (i. e., $0.5\left(\overline{u'^2}+\overline{w'^2}\right)\Big/\bar{U}^2$) for the test cases of *Re*= 36.7K and 50.5K. Corresponding to the generation of upwash flows near the back rims of the dimples as shown schematically in Fig. 11, regions with high *TKE* values can be seen clearly near the back rims of the dimples. It can also be seen that, while the magnitudes of the normalized

in-plane TKE values in the boundary layer flow over the dimpled surface were found to become greater as the Reynolds number increases, the regions with relatively greater *TKE* values near the back rims of the dimples were also found to become much wider for the case with higher Reynolds numbers.

It is well known that convective heat transfer process over a heated surface is closely related to the flow characteristics of the turbulent boundary layer over the surface. Turbulence kinetic energy (*TKE*) is one of the most widely used quantities to indicate the extent of turbulent mixing in a turbulent flow. A much higher TKE level would indicate more intensive mixing in the turbulent flow, which would lead to a stronger convective heat transfer process. With an infrared thermography technique to quantify local heat transfer characteristics of dimpled arrays at different Reynolds numbers, Mahmood and Ligrani [15] found that the regions with high local *Nusselt number* levels are usually located near the back rims of dimples, which is correlated very well with the regions with high turbulence kinetic energy (*TKE*) levels as shown in Fig. 12.

In the present study, by combining the 2-D PIV measurement results of the *in-plane* TKE in the vertical plane (i.e., $0.5\left(\overline{u'^2}+\overline{v'^2}\right)\Big/\bar{U}^2$ as shown in Figs. 8 to 10) and the horizontal plane (i.e., $0.5\left(\overline{u'^2}+\overline{w'^2}\right)\Big/\bar{U}^2$ as shown in Fig. 12), the normalized TKE *(i.e.,* $TKE=0.5(\overline{u'^2}+\overline{v'^2}+\overline{w'^2})/\bar{U}^2$) of the boundary layer flow over the dimpled surface can be determined. Figure 13(a) shows the profiles of the normalized *TKE* along the centerline of the dimple in the *Y/D*≈0.08 plane. The heat transfer measurement results of Mahmood and Ligrani [15] in the term of measured local *Nusselt* number along the centerline of a dimple at similar test conditions as those used in the present study were given in Fig. 13(b)

for qualitative comparison. As shown clearly in Fig. 13(a), the normalized TKE levels were found to decrease slightly in the region over the front portion of the dimple, and reaching their minimum values at the downstream location of $X/D \approx 0.2$. The normalized TKE values were found to increase gradually afterwards as the downstream distance increases, reaching their maximum peaks at the downstream location of $X/D \approx 1.1$, and then decrease gradually at further downstream locations. The general trend of the normalized TKE profiles of the present study was found to match well with that revealed from the measured local Nusselt number profiles of Mahmood and Ligrani [15] given in Fig. 13(b). As shown in schematically in Fig. 11, since the low-speed recirculating flow inside the dimple cavity would trap the hot fluid inside the dimple cavity, the heat transfer process over the wall surface near the front rim of the dimple would be deteriorated. As a result, the local Nusselt number was found to decrease gradually over the wall surface near the front rim of the dimple, as shown clearly in Fig. 13(b). Due to the impingement of the high-speed coolant flow onto the wall surface near the back rim of the dimple, a strong upwash stream is generated in the boundary layer flow over the back portion of the dimple, which would significantly enhance the turbulent mixing in the boundary layer flow over the back portion of the dimpled surface, consequently, augment the heat transfer process between the high-speed coolant flow and the low-speed hot flow over the wall surface near the back rim of the dimple. Therefore, the local Nusselt number was found to increase continuously over the surface at the back portion of the dimple. As described in Mahmood and Ligrani [15], the measured local Nusselt number would reach their minimum and maximum values at about $0.2D$ and $1.1D$ away from of the front rim of the dimple, which are found to correlate very well with the positions of the minimum and maximum peaks

of the normalized TKE (i.e., at the downstream locations of $X/D \approx 0.2$ and $X/D \approx 1.1$) revealed in the normalized TKE profiles shown in Fig. 13(a).

4. Conclusions

In the present study, an experimental investigation was conducted to quantify the characteristics of the boundary layer flow on and over a dimpled surface in comparison to those over a conventional flat plate. The experimental study was conducted in a low speed, open-circuit wind tunnel with the Reynolds number (i.e., based on the hydraulic diameter of the dimpled channel and freestream velocity) of the test cases in the range of Re=8,200 to 50,500. In addition to measuring surface pressure distributions to determine the friction factors of the test plates and to reveal detailed surface pressure map inside a dimple cavity, a high-resolution digital Particle Image Velocimetry (PIV) system was used to achieve detailed flow field measurements to quantify the characteristics of the turbulent boundary layer flows over the dimpled test plate and the evolution of the unsteady vortex structures inside the dimple cavity at the middle of the dimpled test plate.

It was found that the friction factor of the dimpled test plate would be about 30% ~ 80% higher than that of the conventional flat plate, depending on the Reynolds number of the test cases, which agrees well with the findings reported in previous studies. The detailed surface pressure measurements inside the dimple cavity at the middle of the dimpled test plate reveal clearly that, while the surface pressure in the front portion of the dimple was found to be relatively low, a region with much high surface pressure would exist near the back rim of the dimple. Such a surface pressure distribution pattern was found to be closely related to the unique flow characteristics inside the dimple cavity.

As shown clearly and quantitatively from the PIV measurement results, the high-speed incoming mainstream flow would separate from the dimpled surface when passing over the front rims of the dimples. The separated boundary layer flow was found to behave more like a free shear layer which is highly unstable, therefore, rolling up of unsteady vortex structures due to the Kelvin–Helmholtz instabilities in the shear layer between the high-speed mainstream flow and the low-speed recirculating flow inside the dimple cavity would be readily realized. The unsteady Kelvin–Helmholtz vortices were found to be able to not only promote the entrainment of high-speed mainstream flow into the near wall region, but also booster the ejection of the low-speed recirculating flow out of the dimple cavity. The existence of the low pressure region at the front portion of the dimple, which is correlated to the formation of the low-speed recirculation zone inside the dimple cavity, would cause the high-speed mainstream flow to shift downward slightly and impinge onto the back rim of the dimple. Consequently, a strong upwash stream was generated, which would significantly enhance the turbulent mixing in the boundary layer flow over the back portion of the dimpled surface. With such a process, a dimple would act as a 'turbulator' to generate unsteady vortex structures and a strong upwash to promote the turbulent mixing in the boundary layer flow over the dimpled surface, thereby, to enhance the heat transfer between the high-speed mainstream flow (i.e., coolant stream) and the low-speed near-wall flow (i.e., hot flow) over the dimpled surface. This is believed to be the primary reason why a dimpled surface can have a good heat transfer enhancement performance with comparatively smaller pressure loss penalties, in comparison to other types of heat transfer augmentation devices such as pin-fins and rib turbulators used for the internal cooling of turbine blades.

The quantitative measurement results given in the present study are believed to be the first of its nature to quantify the characteristics of the boundary layer flows over dimpled surfaces and evolution of the unsteady vortex structures inside dimple cavities, which depict a vivid picture about the unique flow features on and above a dimpled surface and their correlations with the enhanced heat transfer performance. Such quantitative information is highly desirable to elucidate underlying physics to gain further insight into underlying physics and to explore/optimize design paradigms for better internal cooling designs to protect turbine blades from the extremely harsh environments.

ACKNOWLEDGMENTS

The technical assistances of Mr. Bill Richard and Mr. Kai Zhang of Iowa State University are greatly appreciated. Support from the National Science Foundation with Grant Nos. IIA-1064235 and CBET-1064196, is gratefully acknowledged. Y. Rao also wants to thank the support from the National Natural Science Foundation of China (No.51176111).

Reference

[1] Han, J., Dutta, S., and Ekkad, S., 2012, Gas turbine heat transfer and cooling technology, Taylor and Francis, New York.

[2] Han, J., and Wright, L., 2006, Enhanced internal cooling of turbine blades and vanes, The Gas Turbine Handbook.

[3] Ligrani, P. M., Harrison, J. L., Mahmmod, G. I., and Hill, M. L., 2001, "Flow structure due to dimple depressions on a channel surface," Phys. Fluids, **13**(11), pp. 3442–3451.

[4] Xie, G., Liu, J., Ligrani, P. M., and Zhang, W., 2013, "Numerical Predictions of Heat Transfer and Flow Structure in a Square Cross-Section Channel with Various Non-Spherical Indentation Dimples," Numer. Heat Transf. Part A Appl., **64**(3), pp. 187–215.

[5] Mitsudharmadi, H., Tay, C., and Tsai, H., 2009, "Effect of rounded edged dimple arrays on the boundary layer development," J. Vis., **12**(1), pp. 17–25.

[6] Neil Jordan, C., and Wright, L. M., 2012, "Heat Transfer Enhancement in a Rectangular (AR = 3:1) Channel With V-Shaped Dimples," J. Turbomach., **135**(1), p. 011028.

[7] Mahmood, G., Hill, M., Nelson, D., and Ligrani, P., 2001, "Local heat transfer and flow structure on and above a dimpled surface in a channel," J. Turbomach., **123**(1), pp. 115–123.

[8] Chyu, M. K., and Siw, S. C., 2013, "Recent Advances of Internal Cooling Techniques for Gas Turbine Airfoils," J. Therm. Sci. Eng. Appl., **5**(2), p. 021008.

[9] Rao, Y., Feng, Y., Li, B., and Weigand, B., 2014, "Experimental and Numerical Study of Heat Transfer and Flow Friction in Channels With Dimples of Different Shapes," J. Heat Transfer, **137**(3), p. 031901.

[10] Rao, Y., Xu, Y., and Wan, C., 2012, "A Numerical Study of the Flow and Heat Transfer in the Pin Fin-Dimple Channels With Various Dimple Depths," J. Heat Transfer, **134**(7), p. 071902.

[11] Chyu, M., Yu, Y., and Ding, H., 1999, "Heat Transfer Enhancement in Rectangular Channels with Concavities," J. Enhanc. Heat Transf., **6**(6), pp. 429–439.

[12] Terekhov, V., Kalinina, S., and Mshvidobadze, Y., 1997, "Heat transfer coefficient and aerodynamic resistance on a surface with a single dimple," J. Enhanc. Heat Transf., **4**(2).

[13] Moon, H. K., O'Connell, T., and Glezer, B., 2000, "Channel Height Effect on Heat Transfer and Friction in a Dimpled Passage," J. Eng. Gas Turbines Power, **122**(2), pp. 307–313.

[14] Ligrani, P., 2013, "Heat transfer augmentation technologies for internal cooling of turbine components of gas turbine engines," Int. J. Rotating Mach., **2013**.

[15] Mahmood, G., and Ligrani, P., 2002, "Heat transfer in a dimpled channel: combined influences of aspect ratio, temperature ratio, Reynolds number, and flow structure," Int. J. Heat Mass Transf., **45**(10), pp. 2011–2020.

[16] Turnow, J., Kornev, N., Zhdanov, V., and Hassel, E., 2012, "Flow structures and heat transfer on dimples in a staggered arrangement," Int. J. Heat Fluid Flow, **35**, pp. 168–175.

[17] Bunker, R., and Donnellan, K., 2003, "Heat transfer and friction factors for flows inside circular tubes with concavity surfaces," ASME Turbo Expo 2003, collocated with the 2003 International Joint Power Generation Conference, American Society of Mechanical Engineers, pp. 21–29.

[18] Choi, E., Choi, Y., and Lee, W., 2013, "Heat transfer augmentation using a rib–dimple compound cooling technique," Appl. Therm. Eng., **51**(1), pp. 435–441.

[19] Ligrani, P. M., Oliveira, M. M., and Blaskovich, T., 2012, "Comparison of Heat Transfer Augmentation Techniques," AIAA J., **41**(3), pp. 337–362.

[20] Viswanathan, A. K., and Tafti, D. K., 2006, "A Comparative Study of DES and URANS for Flow Prediction in a Two-Pass Internal Cooling Duct," ASME J. Fluids Eng., **128**(6), p. 1336.

[21] Joo, J., and Durbin, P., 2009, "Simulation of Turbine Blade Trailing Edge Cooling," ASME J. Fluids Eng., **131**(2), p. 021102.

[22] Bogard, D. G., 2006, "Airfoil film cooling," The Gas Turbine Handbook, National Energy Technology Laboratory, Section 4.2.2.1.

[23] Ling, J., Rossi, R., and Eaton, J. K., 2014, "Near Wall Modeling for Trailing Edge Slot Film Cooling," ASME J. Fluids Eng., **137**(2), p. 021103.

[24] Farhadi-Azar, R., Ramezanizadeh, M., Taeibi-Rahni, M., and Salimi, M., 2011, "Compound Triple Jets Film Cooling Improvements via Velocity and Density Ratios: Large Eddy Simulation," ASME J. Fluids Eng., **133**(3), p. 031202.

[25] Yang, L., Ligrani, P., Ren, J., and Jiang, H., 2015, "Unsteady Structure and Development of a Row of Impingement Jets, Including Kelvin–Helmholtz Vortex Development," ASME J. Fluids Eng., **137**(5), p. 051201.

[26] Soloff, S. M., Adrian, R. J., and Liu, Z.-C., 1997, "Distortion compensation for generalized stereoscopic particle image velocimetry," Meas. Sci. Technol., **8**(12), pp. 1441–1454.

[27] Schlichting, Herrmann, Klaus Gersten, and K. G., 2000, Boundary-layer theory, Springer Science & Business Media.

[28] Pope, S., 2000, Turbulent flows, Cambridge university press, England.

[29] Munson, B., Rothmayer, A., and Okiishi, T., 2012, Fundamentals of fluid mechanics 6th edition, Wiley Global Education.

[30] Liu, T., Makhmalbaf, M. H. M., Vewen Ramasamy, R., Kode, S., and Merati, P., 2015, "Skin Friction Fields and Surface Dye Patterns on Delta Wings in Water Flows," ASME J. Fluids Eng., **137**(7), p. 071202.

[31] He, S., and Gotts, J. A., 2004, "Calculation of Friction Coefficients for Noncircular Channels," ASME J. Fluids Eng., **126**(6), p. 1033.

[32] Dean, R. B., 1978, "Reynolds Number Dependence of Skin Friction and Other Bulk Flow Variables in Two-Dimensional Rectangular Duct Flow," ASME J. Fluids Eng., **100**(2), pp. 215–223.

Table 1. *Reynolds numbers of the three test cases.*

Test Cases	Reynolds number based on hydraulic diameter, D_h	Reynolds number based on dimple diameter (D) or height (H)	Reynolds number based on momentum thickness (θ)
Case #1	8.2K	4.6K	306
Case #2	36.7K	20.7K	1187
Case #3	50.5K	28.5K	1370

Table 2. *Flow characteristics of the oncoming boundary layer flow over the test plate.*

Test Cases	Displacement thickness (δ^*)	Momentum thickness (θ)	Shape factor (H^*)	Friction velocity (m/s)	Wall shear stress (N/m^2)
Re=8.2K	0.175δ	0.114δ	1.54	-	-
Re=36.7K	0.130δ	0.099δ	1.31	0.90	0.96
Re=50.5K	0.110δ	0.083δ	1.32	1.14	1.53

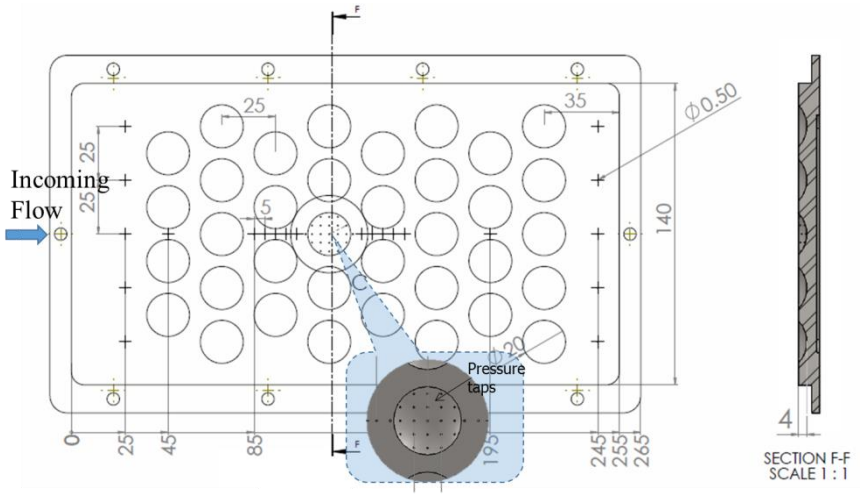

(a) A dimpled test plate

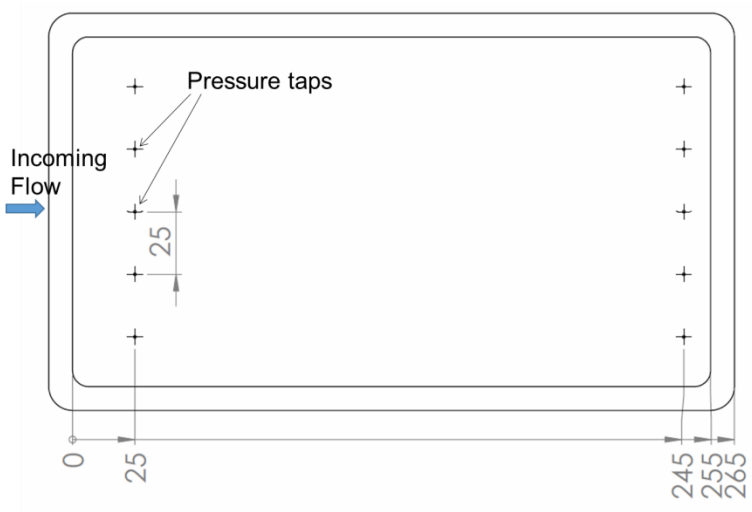

(b) A conventional flat test plate

Figure 1. *Schematic of the two test plates used in the present study (unit in mm).*

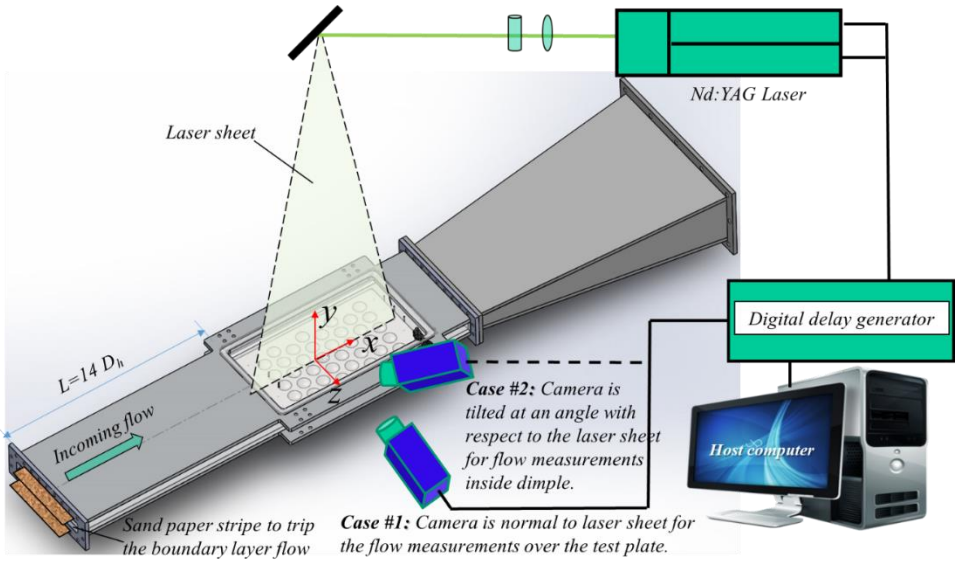

Figure 2. *Experimental setup for PIV measurements.*

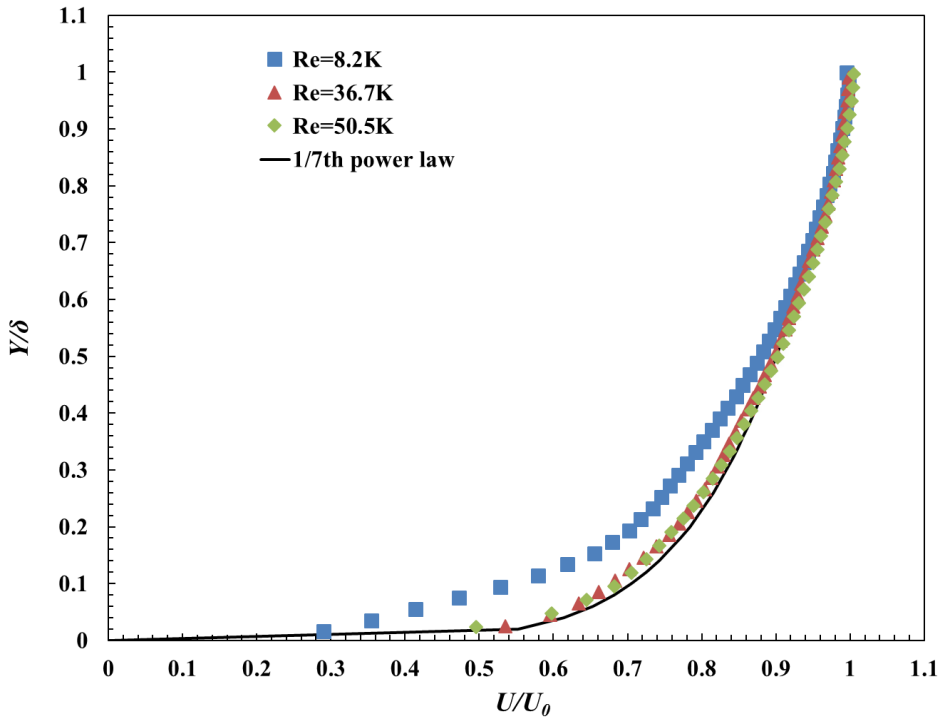

Figure 3. *Measured velocity profiles of the oncoming boundary layer flow at the entrance of test plate for the test cases of Re=8.2K, 36.7K and 50.5K respectively (where U_0 is the maximum flow velocity inside the channel.*

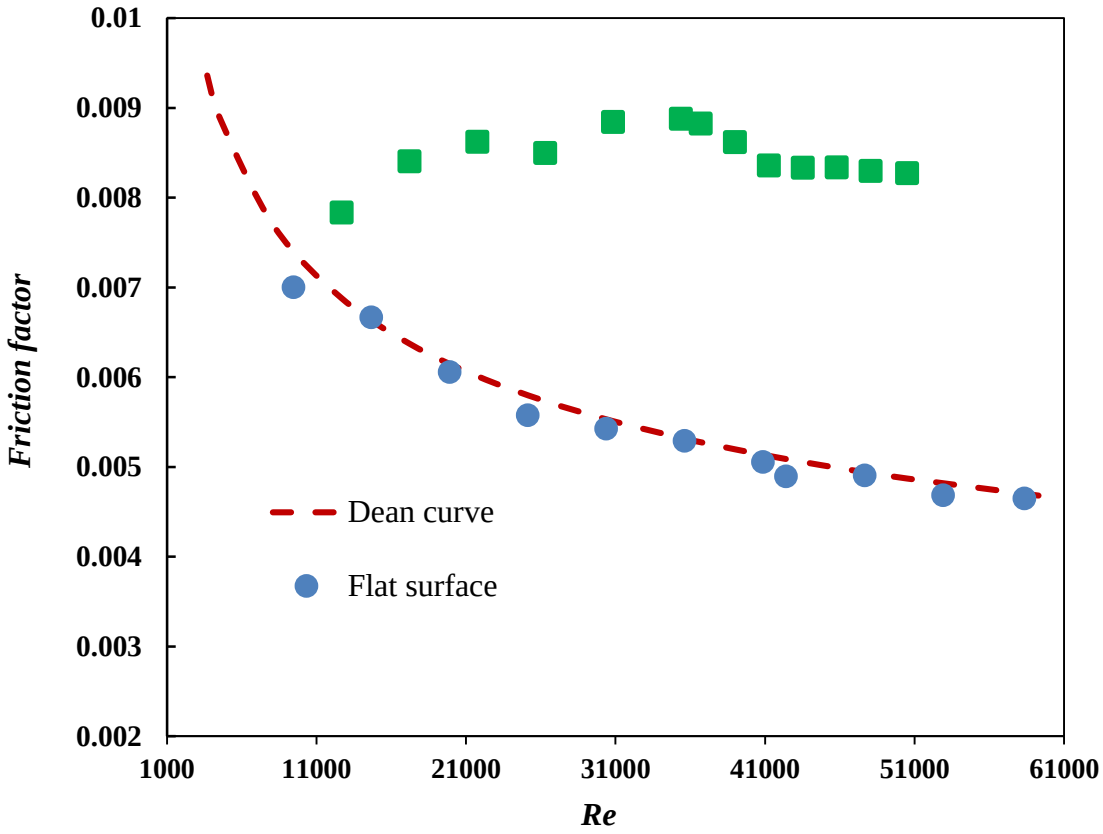

Figure 4. *Measured friction factors of the test plates a function of the Reynolds number.*

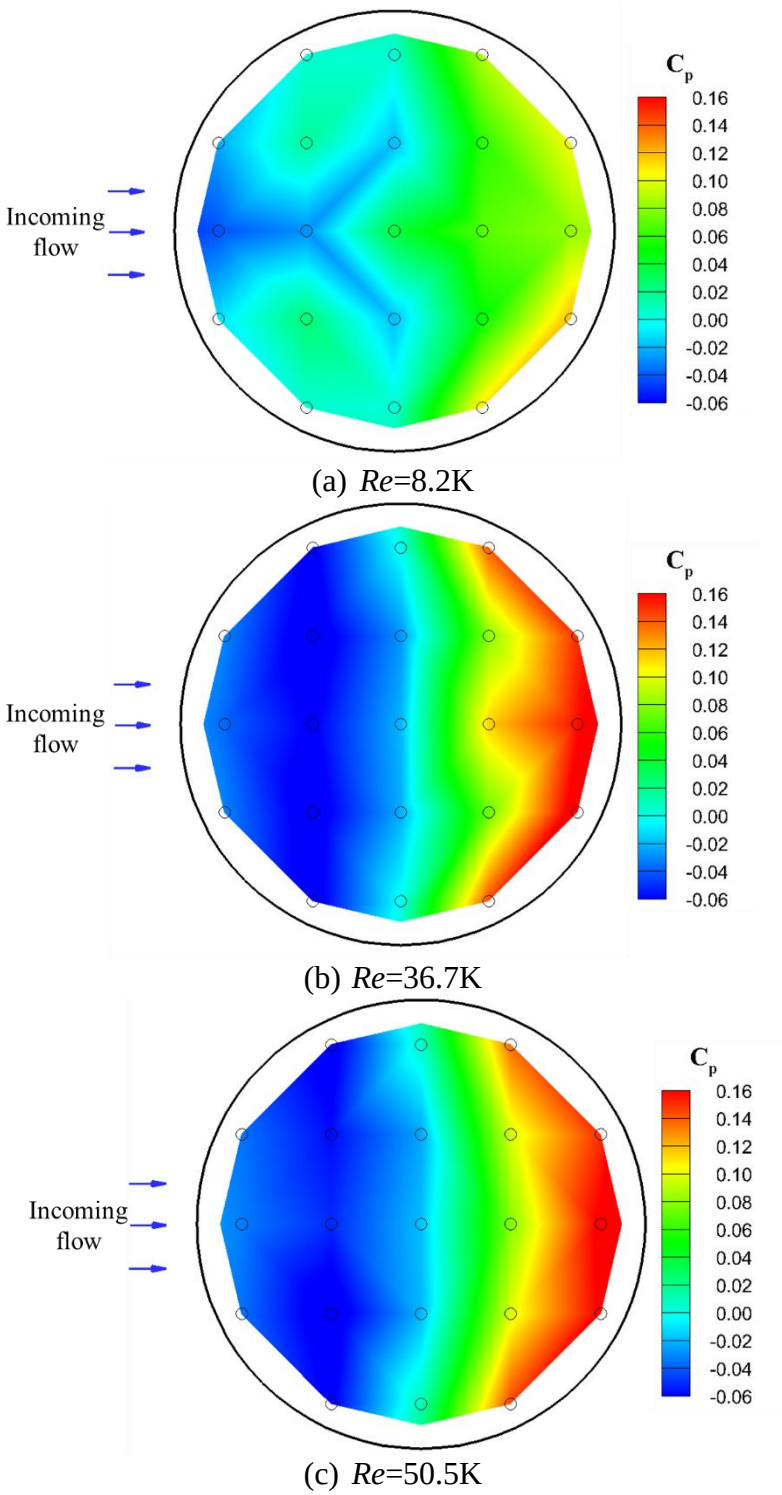

Figure 5. *Measured surface pressure coefficient distributions inside the dimple cavity.*

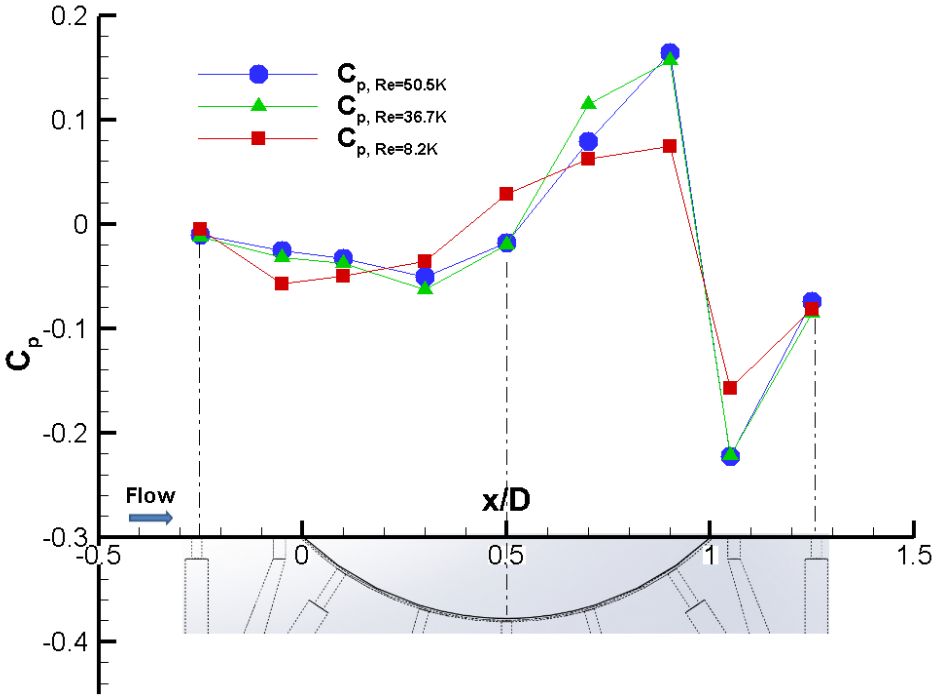

Figure 6. *The profiles of the surface pressure coefficient along the centerline of the dimple.*

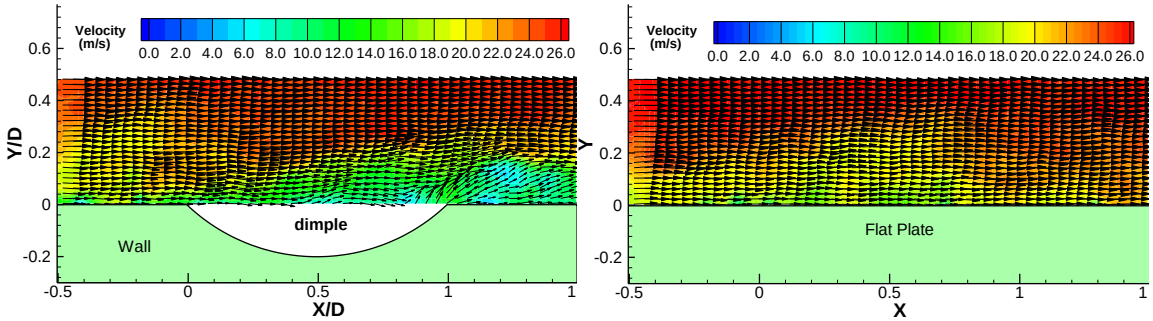

(a) Instantaneous velocity field over the dimpled (left) and flat (right) surfaces

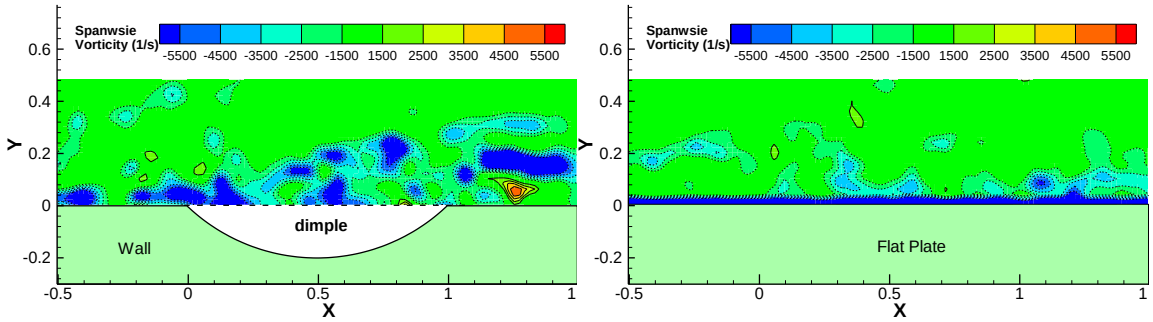

(b) Instantaneous vorticity distributions over the dimpled (left) and flat (right) surfaces

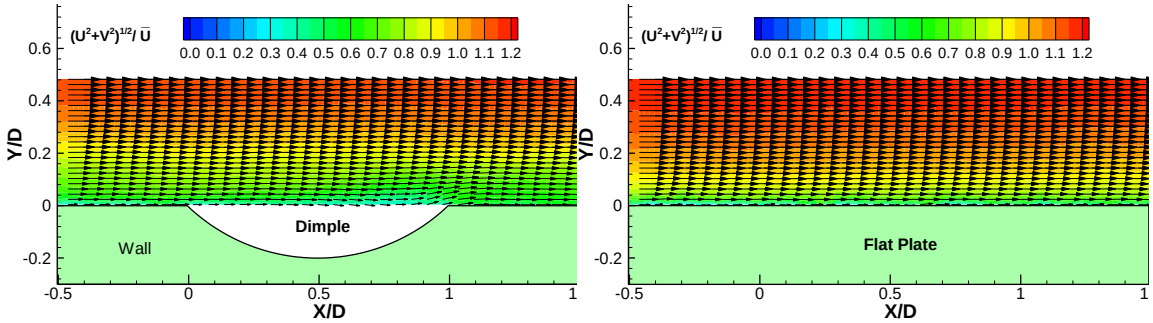

(c) Mean velocity field over the dimpled (left) and flat (right) surfaces

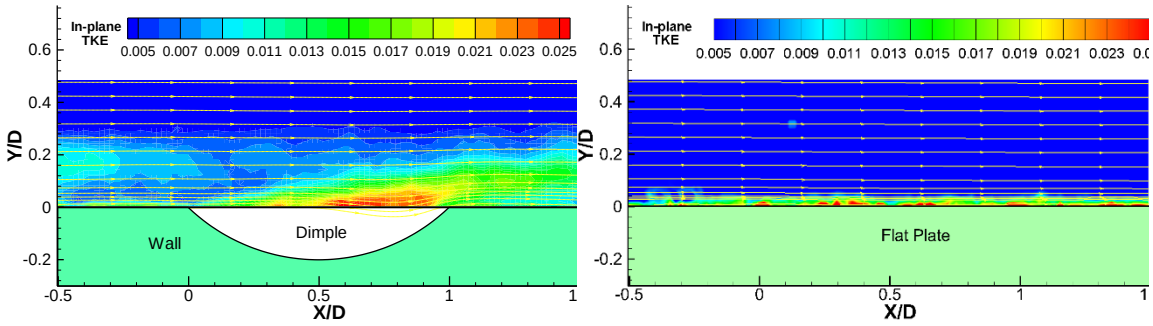

(d). In-plane TKE distribution over the dimpled (left) and flat (right) surfaces

Figure 7. *PIV measurements of the flow field over the dimpled and flat surfaces at Re=50.5K.*

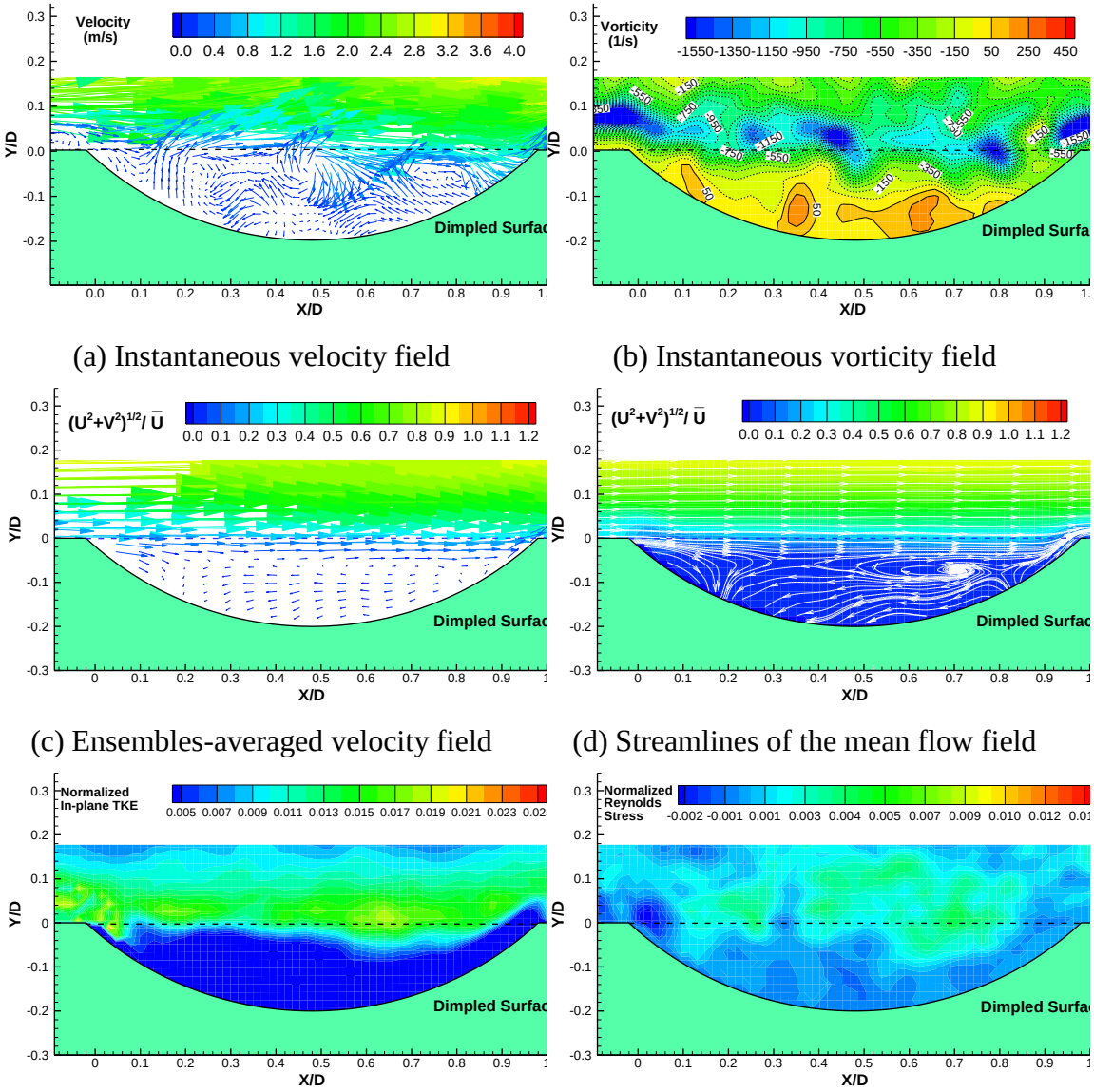

(a) Instantaneous velocity field

(b) Instantaneous vorticity field

(c) Ensembles-averaged velocity field

(d) Streamlines of the mean flow field

(e) Normalized in-plane TKE

(f) Normalized Reynolds stress

Figure 8. *PIV measurement results of the flow field inside the dimple at* Re=*8.2K.*

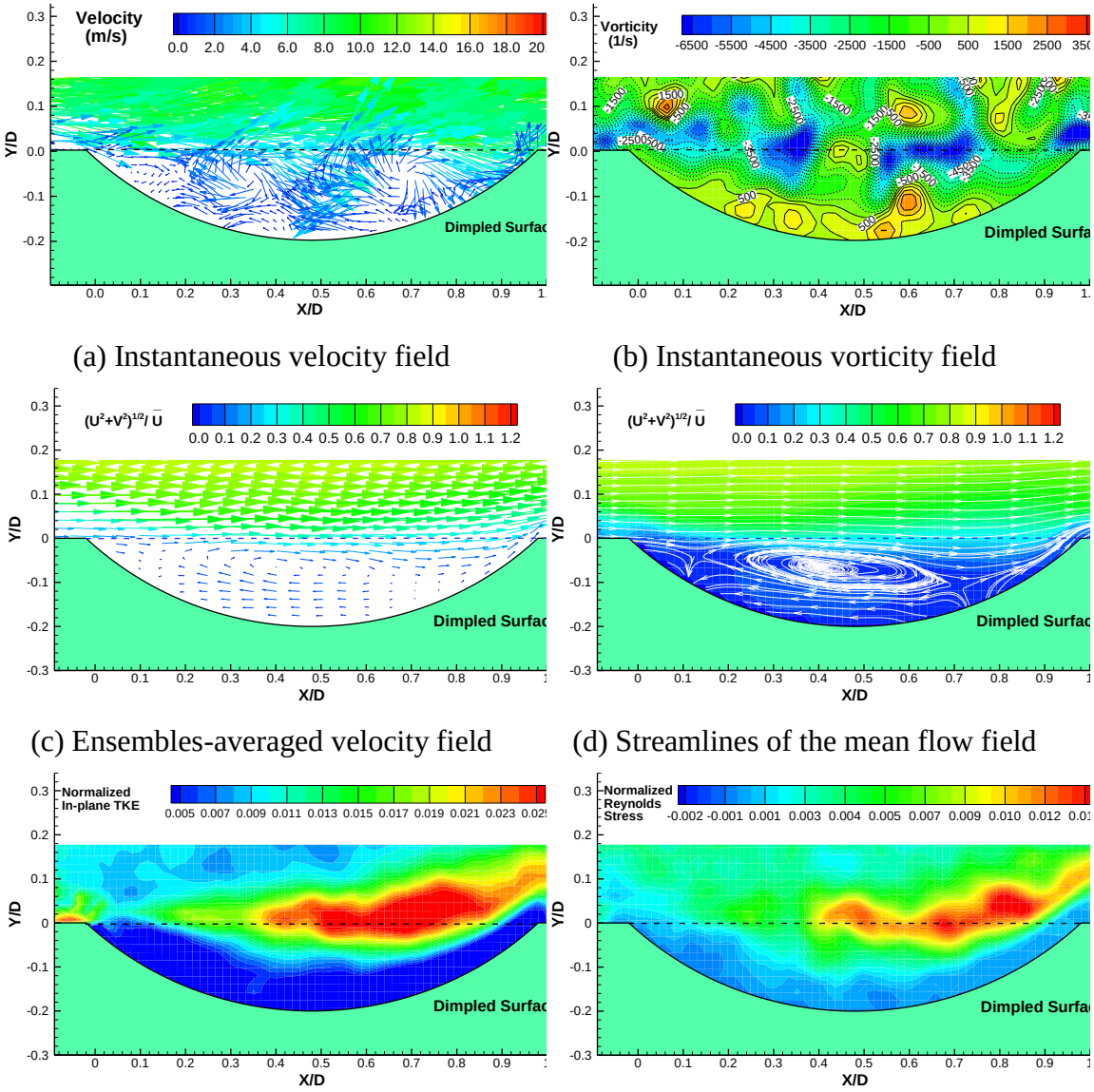

(a) Instantaneous velocity field

(b) Instantaneous vorticity field

(c) Ensembles-averaged velocity field

(d) Streamlines of the mean flow field

(e) Normalized in-plane TKE

(f) Normalized Reynolds stress

Figure 9. *PIV measurement results of the flow field inside the dimple at* Re*=36.7K.*

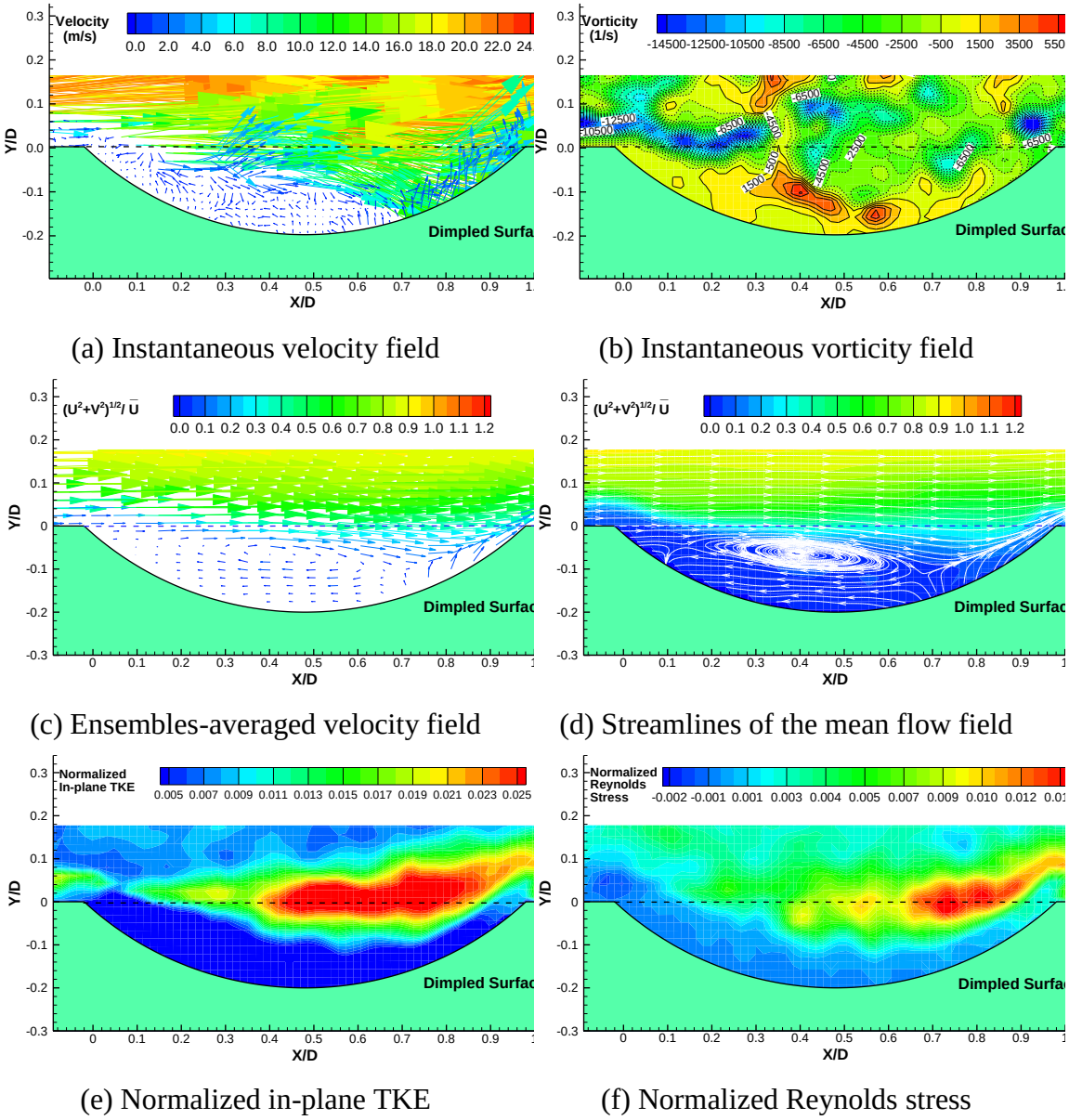

(a) Instantaneous velocity field

(b) Instantaneous vorticity field

(c) Ensembles-averaged velocity field

(d) Streamlines of the mean flow field

(e) Normalized in-plane TKE

(f) Normalized Reynolds stress

Figure 10. *PIV measurement results of the flow field inside the dimple at* Re=*50.5K.*

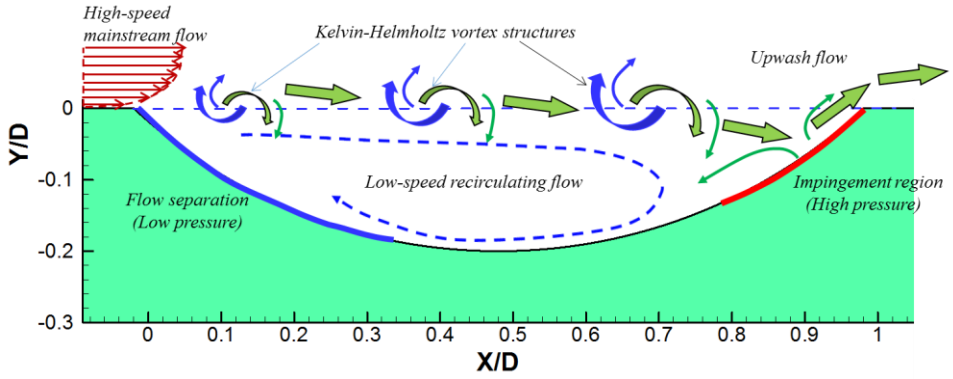

Figure11. *Schematic of the flow structures inside a dimple cavity*

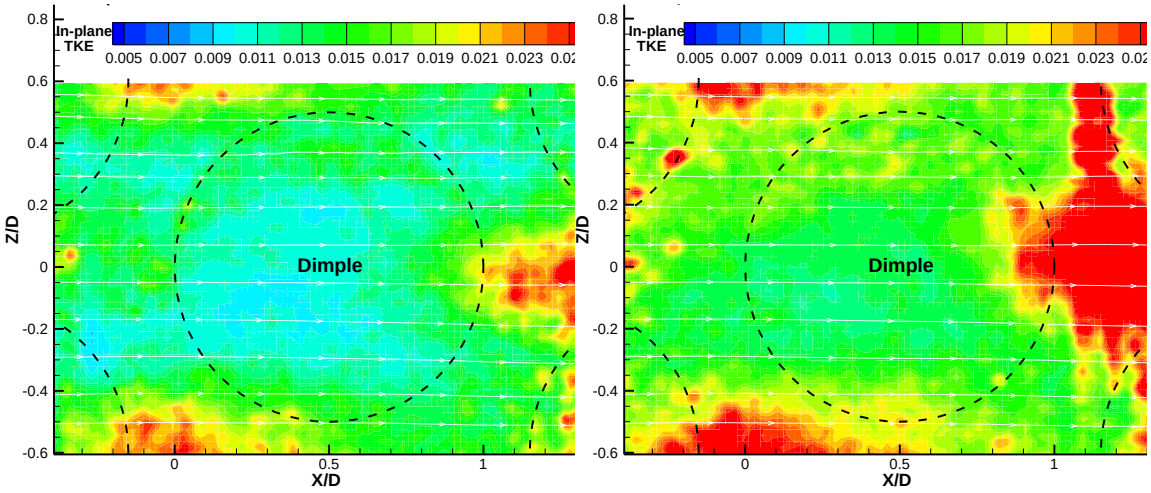

(a) *Re*= 36.7K (b) *Re*= 50.5K

Figure 12. *Distributions of the normalized in-plane TKE (i.e.,* $0.5\left(\overline{u'^2}+\overline{w'^2}\right)/\bar{U}^2$ *) in the horizontal plane near the upper surface of the dimpled test plate.*

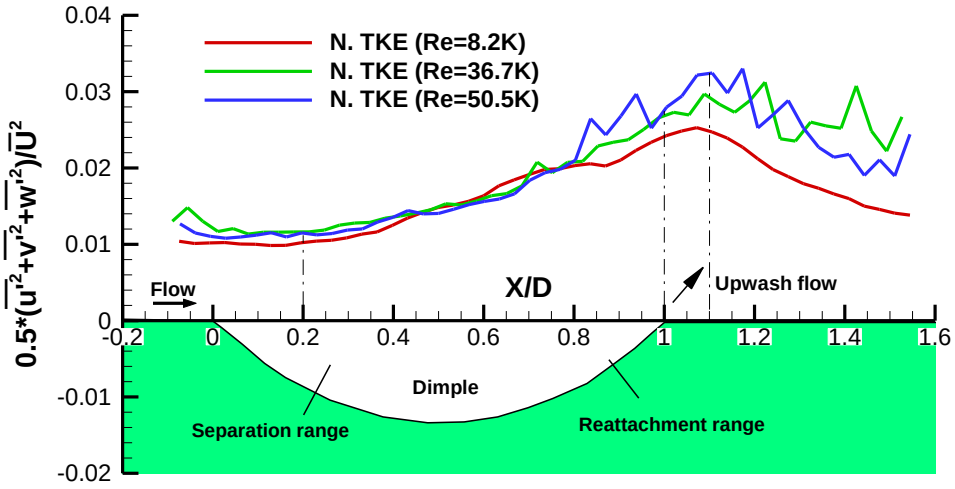

(a) Measured *TKE* profiles of the present study

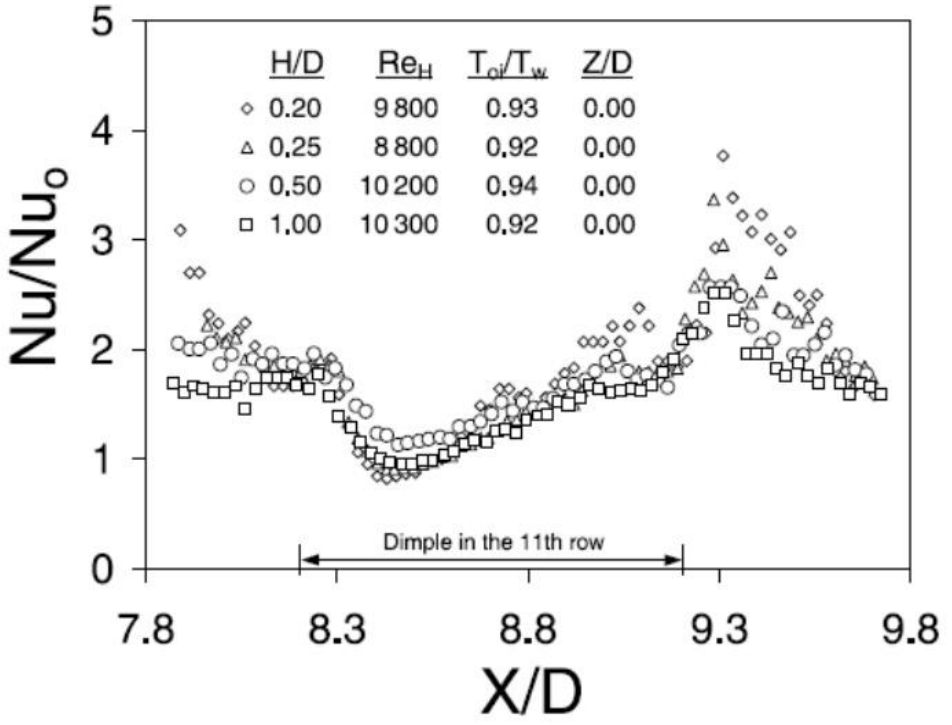

(b). Measured local Nusselt number data reported in Mahmood and Ligrani [15]

Figure 13. *The measured TKE profiles of the present study along with the local Nusselt number data reported in Mahmood and Ligrani [15].*

CHAPTER 6

CONCLUSIONS AND FUTURE WORK

1. General Conclusions

In this chapter, the major accomplishments achieved in this dissertation were summarized and discussed below. There are total of four topics: Barchan-dune-shaped ramp, Barchan-dune-shaped injection compound, compressibility effect on film cooling effectiveness, and flow characteristics over dimpled surface. Future work with respect to the study of effectiveness in cascade testing was also suggested.

1.1 Improved effectiveness by using Barchan-Dune-Shaped ramp (BDSR).

Inspired by the unique shape of Barchan dune, which prevents sand particles on the ground from being blown away by the oncoming flow, we proposed a BDSR for film cooling. The influence of mass flux ratio (M=0.40, 0.85, 1.00, 1.25), dune location (DB=-3.0D, -0.9D, 2.7D, 3.4D), and height (H=0.3D, 0.5D) of dune on film cooling effectiveness were investigated experimentally using the PSP technique. Meanwhile a high-resolution PIV system was used to conduct detailed flow field measurements in order to quantify the turbulent mixing between coolant and mainstream flow behind the Barchan-dune-shaped ramps.

1) The experimental results revealed that BDSR with H=0.5D and L=-0.9D can largely enhance the cooling performance of a cylindrical hole. Compared with circular hole, there was a 50%-100% gain in Area-averaged effectiveness for BDSR (H=0.5D, L=0.9D) at M>0.85.

2) Investigation of flow physics using PIV and stereo-PIV showed three distinct mechanisms for enhancement of film cooling performance (i) down-wash stream from the crest of dune lowered and diffused the coolant jet in the stream-wise direction, (ii) vortex structure in *X*-*Z* plane generated continuous suction along the horn of dunes, resulting in wider lateral film coverage, and (iii) formation of the Anti-CRV pair in *Y*-*Z* plane counteracted the vortex induction from the coolant jet, causing downdraught of coolant from jet core.

3) The film cooling effectiveness of BDSR was found to be closely related to both the location and height of the dune. With dune upstream, the H=0.5D case is a better solution. This is due to the stronger downwash and suction effects in the taller case. However, the H=0.3D is a considerable solution for the dune downstream.

1.2 Barchan-Dune-Shaped injection compounds (BDSIC) for enhanced effectiveness.

Upgraded from the BDSR configuration, the BDSIC film cooling concept was proposed. An experimental study was conducted to examine the cooling performance of BDSIC using PSP and PIV techniques. The effects of dune shape (shorted, normal, and elongated dune), mass flux ratio (M=0.6, 0.9, 1.2, 1.5), density ratio (DR=0.97, 1.5, 2.1), and hole interaction on cooling effectiveness were studied in great detail.

1) It was found that the BDSICs can significantly enhance the effectiveness of original hole, especially the BDSIC with elongated dune. Comparing to a circular hole, there are over 30%, 150%, and 500% gain in lateral effectiveness for the elongated case at M=0.6, 0.9, and 1.2 respectively.

2) The mechanisms for enhancement of effectiveness in BDSIC was revealed clearly by PIV and stereo-PIV measurements, (i) continual suppression on coolant gas leaded to a stable and uniform coolant coverage, similar to a tangential slot, (ii) complete elimination of CRV pair prevented the jet from lifting off, and (iii) formation of Anti-CRV pair in the *Y-Z* plane generated a downdraught of coolant from jet core, and enhanced the lateral film coverage.

3) Unlike traditional cooling holes, the effectiveness of BDSIC was found to keep increasing as the mass flux ratio increased.

4) The BDSIC exhibited a weak dependent upon the density ratio. Due to the appearance of dune cover, the coolant jet would hit the inner surface and eject tangentially into the mainstream disregarding the density difference, leading to a close cooling effectiveness.

5) Detailed analysis showed that the loss generated by the penetration process in circular hole was much greater than that of BDSIC. With the help of dune cover, the aerodynamic loss was reduced at high mass flux ratio.

All in all, the BDSIC concept is a hybrid of Barchan dune and tangential slot film cooling, which inherits the merits of both. It is able to produce enhanced effectiveness with less aerodynamic loss at high mass flux ratio.

1.3 The Compressibility Effects on Film Cooling Effectiveness.

Using the transonic speed wind tunnel of ISU, an experimental study was performed to investigate the compressibility effects on film cooling, where the mainstream Mach numbers were 0.07, 0.30, 0.50, and 0.70 respectively.

1) It was found that, at M=0.40, the mainstream Mach number had limited effect on the effectiveness of film cooling. Their effectiveness were similar and had been verified by the similar flow field from the PIV experiment.

2) Increasing M to 0.85 and 1.25, the measured effectiveness of Ma=0.30, 0.50, 0.70 cases were found to be marginally higher than that of Ma=0.07. Due to the Bernoulli's principle, the middle jet of high speed cases was attracted by the adjacent streams to pull down slightly and spread wider over the surface. Also the growth rate of shear layers was decreased as the mainstream velocity and mass flux ratio increased.

3) In general, the difference of area-averaged effectiveness were found to be within 15% between high speed and low speed cases. Therefore, when the mass flux ratio is not particular high, it is acceptable to study the film cooling effectiveness of transonic speed flow by performing experiments in a relatively low-speed wind tunnel.

1.4 The Characteristics of Turbulent Boundary Layer Flows over Dimpled Surface.

The experimental study was conducted in a low speed, open-circuit wind tunnel with the Reynolds number (i.e., based on the hydraulic diameter of the dimpled channel and freestream velocity) of the test cases in the range of Re=8,200 to 50,500. In addition to measuring surface pressure distributions to determine the friction factors of the test plates and to reveal detailed surface pressure map inside a dimple cavity, a high-resolution digital Particle Image Velocimetry (PIV) system was used to achieve detailed flow field measurements to quantify the characteristics of the turbulent boundary layer flows over the dimpled test plate.

1) The friction factor of the dimpled test plate would be about 30% ~ 80% higher than that of the conventional flat plate, depending on the Reynolds number of the test cases, which agrees well with the findings reported in previous studies.

2) The surface pressure in the front portion of the dimple was found to be relatively low, a region with much higher surface pressure would exist near the back rim of the dimple.

3) As shown quantitatively from the PIV results, the high-speed incoming flow would separate from the dimpled surface when passing over the front rims of the dimples. The separated boundary layer flow was found to behave more like a free shear layer which is highly unstable. Therefore, rolling up of unsteady vortex structures due to the Kelvin–Helmholtz instabilities in the shear layer between the high-speed mainstream flow and the low-speed recirculating flow inside the dimple cavity would be readily realized.

4) The unsteady Kelvin–Helmholtz vortices were found to be able to not only promote the entrainment of high-speed mainstream flow into the near wall region, but also booster the ejection of the low-speed recirculating flow out of the dimple cavity.

5) The strong upwash stream significantly enhanced the turbulent mixing in the boundary layer flow over the back portion of the dimpled surface, leading to an augmented heat transfer between the high-speed mainstream flow and the low-speed near-wall flow over the dimpled surface. This is believed to be the primary reason why a dimpled surface can have a good heat transfer enhancement performance with comparatively smaller pressure loss penalties compared to pin-fins.

2. Future Work

As for the film cooling study of BDSIC, the present study showed enhanced effectiveness with less aerodynamic loss. But the experiment was conducted on a flat plate with low turbulent intensity. For a more practical situation, it will be particular interesting to measure the effectiveness and heat transfer coefficient of BDSIC in film cooled turbine cascade. Which is close to real engine environment, it is able to obtain more valuable results.

For the study on the internal cooling, it is interesting to instantaneously resolve the three-dimensional vortex shedding in the span-wise direction. Based on that, more accurate analysis of the vortex shedding effect on the coefficient of heat transfer could be realized. Comprehensive understanding of dimpled cooling is of great importance to further optimize the geometry of internal cooling.

APPENDIX

MEASUREMENT UNCERTAINTY AND REPEATABILITY ANALYSIS OF PSP TECHNOLOGY

The film cooling effectiveness is calculated by,

$$\eta = 1 - \frac{1}{\left(P^*_{air} / P^*_{gas} - 1\right) DR + 1} \ . \tag{1}$$

It is determined by P^*_{air}, P^*_{gas} and *DR* these three variables. Applying Taylor Series Method to estimate the measurement uncertainty, the film cooling uncertainty should be

$$\Delta\eta^2 = \left(\frac{\partial\eta}{\partial P^*_{air}}\Delta P^*_{air}\right)^2 + \left(\frac{\partial\eta}{\partial P^*_{gas}}\Delta P^*_{gas}\right)^2 + \left(\frac{\partial\eta}{\partial DR}\Delta DR\right)^2 . \tag{2}$$

And the derivatives can be obtained below, where $P^*_{air} = f(I^*_{air})$, $P^*_{gas} = f(I^*_{gas})$ (PSP Calibration function).

$$\frac{\partial\eta}{\partial P^*_{air}} = \frac{1}{\left[\left(P^*_{air} / P^*_{gas} - 1\right) DR + 1\right]^2} \frac{DR}{P^*_{gas}} \ , \tag{3}$$

$$\frac{\partial\eta}{\partial P^*_{gas}} = \frac{1}{\left[\left(P^*_{air} / P^*_{gas} - 1\right) DR + 1\right]^2} \frac{-DR * P^*_{air}}{P^{*\,2}_{gas}} \ , \tag{4}$$

$$\frac{\partial\eta}{\partial DR} = \frac{1}{\left[\left(P^*_{air} / P^*_{gas} - 1\right) DR + 1\right]^2} (P^*_{air} / P^*_{gas} - 1) , \tag{5}$$

Therefore if we know I^*_{air}, ΔI^*_{air}, I^*_{gas} and ΔI^*_{gas}, these two ΔP^*_{gas} and ΔP^*_{air} can be computed by $\Delta P^* = \frac{1}{2}\left[P^{*+}\left(I^* + \Delta I^*\right) - P^{*-}\left(I^* - \Delta I^*\right)\right]$, as illustrated in Figure 1.

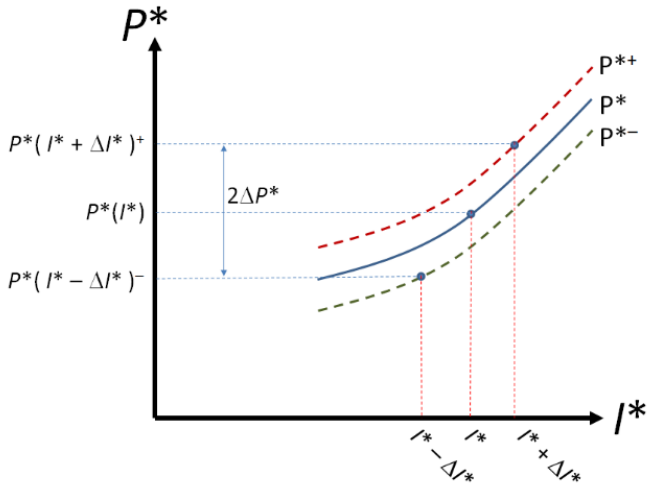

Figure 1. *Uncertainty propagation through the PSP calibration curve.*

$$I^*_{gas} = \frac{I_{ref} - I_b}{I_{gas} - I_b}\ , \tag{6}$$

$$I^*_{air} = \frac{I_{ref} - I_b}{I_{air} - I_b}\ , \tag{7}$$

$$\Delta I^{*}{}^{2}_{gas} = \left(\frac{1}{I_{gas} - I_b}\Delta I_{ref}\right)^2 + \left(\frac{I_{ref} - I_{gas}}{\left(I_{gas} - I_b\right)^2}\Delta I_b\right)^2 + \left(\frac{I_{ref} - I_b}{\left(I_{gas} - I_b\right)^2}\Delta I_{gas}\right)^2 \tag{8}$$

$$\Delta I^{*}{}^{2}_{air} = \left(\frac{1}{I_{air} - I_b}\Delta I_{ref}\right)^2 + \left(\frac{I_{ref} - I_{air}}{\left(I_{air} - I_b\right)^2}\Delta I_b\right)^2 + \left(\frac{I_{ref} - I_b}{\left(I_{air} - I_b\right)^2}\Delta I_{gas}\right)^2 \tag{9}$$

And I_{gas} is Gas Jet Image (ensemble average of 3500), I_{air} is Air Jet Image (ensemble average of 200), I_{ref} is Reference Image (ensemble average of 100), and I_b is Background Image (ensemble average of 60).

Each image ensemble can be analyzed to determine the 95% confidence interval of the intensity, assuming normal distribution ($\Delta I_x = 1.96\sigma_x / \sqrt{N}$, σ_x is the standard deviation, *N* is the number of images).

Therefore, we can achieve the film cooling effectiveness measurement uncertainty distribution based on above analysis. Please refer to Johnson and Hu [1] for more detailed measurement uncertainty analysis.

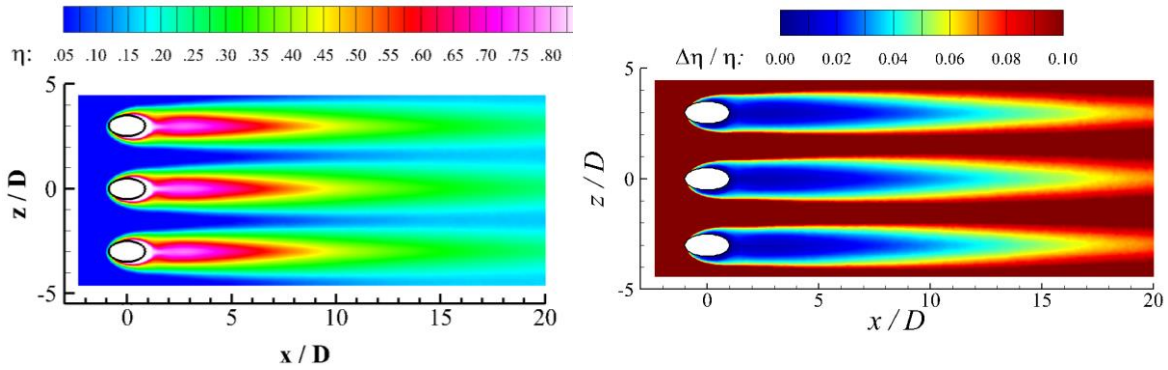

(a)

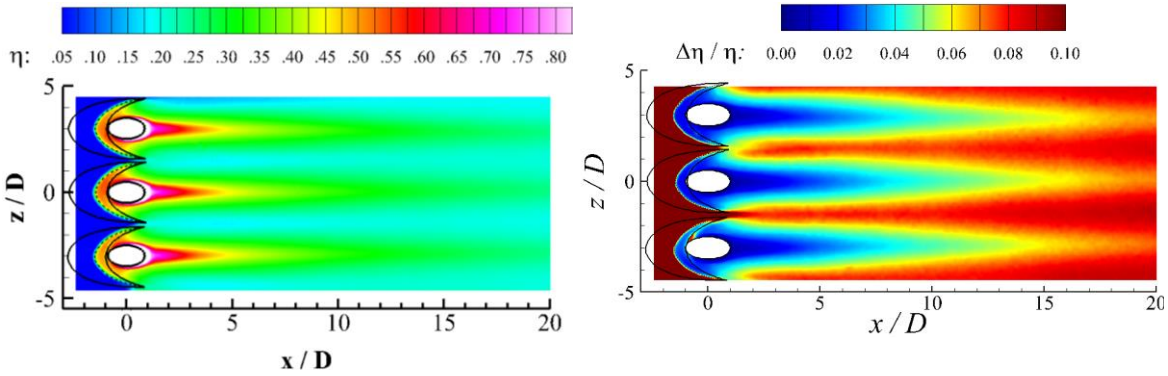

(b)

Figure 2. *The film cooling effectiveness (lift) and corresponding measurement uncertainty (right) distributions. (a) Circular hole at M=0.6, (b) WBD at M=0.85.*

Figure 2 shows the film cooling effectiveness and corresponding measurement uncertainty distribution of without and with dune cases. Carefully inspecting these contours, we can obtain that the estimated measurement uncertainty of centerline effectiveness is about 3% for $\eta = 0.5$, 5% for $\eta = 0.3$, but the uncertainty of upstream locations could be as high as 30%.

Since the definition of lateral averaged film cooling effectiveness is $\eta_{LA}(x) = \int \eta_i(x,z)dz = \sum_{i=1}^{n} \eta_i(x,z_i)\Delta z$, the uncertainty for discrete measurements can be reduced to $\Delta\eta(x) = RMS(\Delta\eta_i(x,z_i))$ which directly results from the root-mean-square of individual uncertainty propagation. Therefore, the estimated measurement uncertainty of lateral-averaged effectiveness is about 7% for $\eta = 0.3$, 10% for $\eta = 0.2$. It is worth mentioned that the discussed uncertainty doesn't include the process uncertainty which was determined to be comparably small and have a negligible effect.

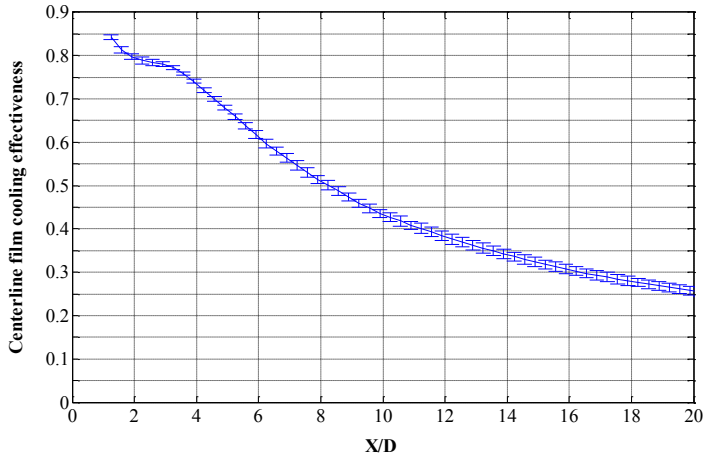

Figure 3. *The centerline effectiveness of circular hole at M=0.6.*

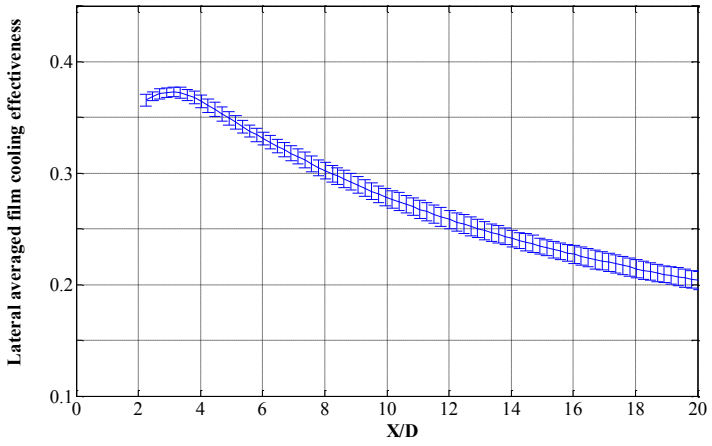

Figure 4. *The lateral-averaged effectiveness of circular hole at M=0.6.*

Three groups of experiment data, obtained through same method and facilities at three separate times, were used to analysis the repeatability of PSP technique. Figure 3 and 4 show the analyzed effectiveness of circular hole at M=0.6, where the mean and standard deviation of effectiveness are included in these figures. Obviously, the variation of measured data were within the measurement uncertainty.

Reference

[1] Johnson, B. E., and Hu, H., 2014, "Measurement Uncertainties Analysis in the Determination of Adiabatic Film Cooling Effectiveness by Using Pressure Sensitive Paint (PSP) Technique," Volume 1D, Symposia: Transport Phenomena in Mixing; Turbulent Flows; Urban Fluid Mechanics; Fluid Dynamic Behavior of Complex Particles; Analysis of Elementary Processes in Dispersed Multiphase Flows; Multiphase Flow With Heat/Mass Transfer in Process Tec, ASME, p. V01DT40A001.